University of Southampton Research Repository

University of Southampton

Faculty of Engineering and Physical Sciences
School of Engineering

Bubble collapse in complex geometries

DOI: 10.5258/SOTON/T0058

by

Elijah David Andrews
MEng
ORCiD: 0000-0002-4634-199X

A thesis for the degree of
Doctor of Philosophy

January 2023

University of Southampton

Abstract

Faculty of Engineering and Physical Sciences
School of Engineering

Doctor of Philosophy

Bubble collapse in complex geometries

by Elijah David Andrews

A gas or vapour bubble near a solid boundary collapses towards the boundary due to the asymmetry induced by the nearby boundary. High surface pressure and shear stress from this collapse can damage, or clean, the surface. The majority of prior research has focused on simple flat boundaries or cases with limited complexity. In this research, we experimentally and numerically investigate how complex geometries affect bubble collapse dynamics.

We first investigate how a slot in a flat boundary affects the jet direction for a single bubble. We use a boundary element model to predict how the jet direction depends on key geometric parameters and experimentally validate the predictions using laser-induced cavitation. We reveal a tendency for the jet to be directed away from a slot.

Various bubble collapse properties, such as bubble displacement and rebound size, have been shown to be a function of the 'anisotropy' of the collapse, measured by a dimensionless representation of the Kelvin impulse known as the anisotropy parameter [Supponen *et al.*, J. Fluid Mech. 802, 263-293 (2016)]. However, characterisation of the anisotropy parameter in different geometries has been limited to simplified analytic solutions. We further develop our boundary element model to be capable of predicting the anisotropy parameter for any rigid complex geometry. We experimentally explore a robust measure of bubble displacement, showing that the bubble displacement in a range of complex geometries behaves as a single function of the predicted anisotropy parameter values.

We then extend this model, in combination with experiments, to the study of porous plates by investigating how the standoff distance, porosity, pore size, and pore shape affect two collapse properties: bubble displacement and bubble rebound size. We show that these properties depend primarily on the standoff distance and porosity of the boundary and show that they each collapse onto respective single curves.

This work provides key insights into the effects of complex geometries on bubble collapse behaviour. The numerical model developed herein provides a simple, inexpensive method to connect complex geometries to the growing framework of studies using the anisotropy parameter.

Contents

Declaration of Authorship

I declare that this thesis and the work presented in it is my own and has been generated by me as the result of my own original research.

I confirm that:

1. This work was done wholly or mainly while in candidature for a research degree at this University;
2. Where any part of this thesis has previously been submitted for a degree or any other qualification at this University or any other institution, this has been clearly stated;
3. Where I have consulted the published work of others, this is always clearly attributed;
4. Where I have quoted from the work of others, the source is always given. With the exception of such quotations, this thesis is entirely my own work;
5. I have acknowledged all main sources of help;
6. Where the thesis is based on work done by myself jointly with others, I have made clear exactly what was done by others and what I have contributed myself;
7. Parts of this work have been published as: Andrews *et al.* (2020), Andrews & Peters (2022), Andrews *et al.* (2022)

Signed:.. Date:..................

Acknowledgements

Thanks to my family and friends for their support during my studies. Particular thanks to the friends who spent many hours keeping me sane during lockdown.

Thanks to the experimental fluids group at University of Southampton for their advice, productive discussion, and patient enthusiasm while watching my many bubble videos. Thanks to Lebo Molefe for experimental collaboration in the earliest days of this research and for invaluable discussion and feedback since.

Thanks to John Shrimpton and Peter Birkin for constructive feedback during the 9- and 18-month review processes.

Thanks to David Fernández Rivas for helpful advice and insightful conversation. And the biggest of thanks to Ivo Peters for his gracious supervision, diligent guidance, and generous support.

Finally, thanks to the EPSRC for financial support under Grant No. EP/P012981/1.

Definitions and Abbreviations

A	Bubble area in frame
A	Panel area
A	Area of porous plate hole
A'	Ratio of hole area to tesselation unit area
c_L	Speed of sound in liquid
Eu	Euler number
$\mathbf{F}$	Force
$\mathbf{F}'$	Equivalent force for $m_b = 1\ \mathrm{m}^3\ \mathrm{s}^{-1}$
g	Gravitational acceleration
H	Plate thickness
H	Slot height
h	Non-dimensional slot height
$\mathbf{I}$	Kelvin impulse
k	Polytropic constant
L	Plate length
M	Total number of mirror sinks
m	Sink volume flow rate
m_b	Bubble sink volume flow rate
N	Total number of boundary elements
$\mathbf{n}$	Normal vector
p_B	Bubble internal pressure
p_G	Gas or vapour pressure
p_{G_0}	Gas or vapour pressure initial condition
p_V	Vapour pressure
p_∞	Far-field pressure
Δp	Driving pressure
R	Bubble radius
R_0	Initial (maximum) bubble radius
$\bar{R}_0$	Mean initial bubble radius
R_1	Maximum bubble radius after first rebound
$\dot{R}$	First time derivative of bubble radius
$\ddot{R}$	Second time derivative of bubble radius

$\bar{R}$	Non-dimensional bubble radius
R	Relative position factor
R	Relative position factor matrix
$\mathbf{R}_b$	Bubble relative position factor vector
Re	Reynolds number
S	Surface tension
S	Boundary surface
S	Hole spacing
t	Time
t_{TC}	Rayleigh collapse time
$\bar{t}$	Non-dimensional time
$\mathbf{u}$	Velocity vector
$\mathbf{u}_b$	Velocity vector at bubble position
V	Bubble volume
W	Slot width
W	Wall surface
W	Characteristic hole length (width)
We	Weber number
X	Horizontal position
x	Non-dimensional horizontal position
$\mathbf{x}$	Position vector
$\mathbf{x}_b$	Bubble position vector
$\mathbf{x}_s$	Sink position vector
$x^\star$	Horizontal position of peak jet angle
$\hat{x}$	Normalised horizontal position
Y	Bubble distance from boundary
Y	Vertical position
y	Non-dimensional vertical position
z	Depth of bubble in water
γ	Ratio of specific heats
γ	Standoff distance
Δ	Bubble displacement distance
δ	Buoyancy parameter
δ	Approximate boundary layer scale
ζ	Anisotropy parameter
$\boldsymbol{\zeta}$	Anisotropy vector
θ	Jet angle
θ_b	Bubble position angle
θ_c	Corner angle
$\theta^\star$	Peak jet angle
$\hat{\theta}$	Normalised jet angle

ν_L	Kinematic viscosity of liquid
ρ_L	Density of liquid
σ	Sink strength density
ϕ	Void fraction
ϕ	Velocity potential
ϕ_b	Bubble velocity potential
ϕ_w	Wall velocity potential
$\nabla\phi$	Velocity
$\nabla\phi'$	Equivalent velocity for $m_b = 1\ \mathrm{m}^3\ \mathrm{s}^{-1}$
RMSD	Root mean squared difference
BEM	Boundary element method

Chapter 1

Introduction

Gas and vapour bubbles collapsing have long been a focus of research in a range of fields. Sections 1.1-1.6 are a review of bubble collapse literature followed by an outline of our research problem in section 1.7.

1.1 Applications

Bubbles collapsing have been studied in connection with a broad range of applications. Investigations were initially instigated in response to damage encountered on ship propellers (Rayleigh, 1917). The low pressures generated by the motion of the propellers causes cavitation to occur which, on collapsing, exert significant damaging loads on the propellers. Cavitation damage has continued to be a focus of research as the damage can be costly and reduce the lifespan of various parts (Luo *et al.*, 2016; Lu *et al.*, 2016; Sagar & el Moctar, 2020). Figure 1.1 shows the damage that occurs on a marine propeller. This damage decreases the service life of the propeller and increases drag, which in turn reduces propeller efficiency.

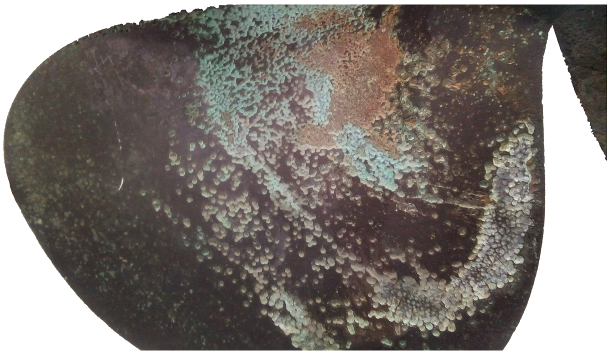

FIGURE 1.1: A propeller damaged by prolonged exposure to cavitation.

Although cavitation damage is often detrimental, it can be used for cleaning objects (Verhaagen & Fernández Rivas, 2016; Birkin *et al.*, 2016). The most commonly implemented method of harnessing these cleaning effects is the application of ultrasound. Passing ultrasound through a fluid causes low and high pressure regions to form which cause bubbles to grow and then collapse. Two common areas of research are investigations of the individual cleaning effects of single bubbles collapsing (Ohl *et al.*, 2006; Chahine *et al.*, 2016) and the cumulative effect of ultrasonic cleaning (Verhaagen *et al.*, 2016; Reuter *et al.*, 2017).

There are also numerous applications in biological and biomedical fields (De La Torre, 1992; Brennen, 2003). Snapping shrimp rapidly close a special claw to induce a high speed jet. The very high speed jet causes a low pressure region to form that cavitates. The collapse of this cavitation creates shockwaves that can be used for defence or to stun and kill prey (Versluis *et al.*, 2000; Shimu *et al.*, 2019). Figure 1.2 shows this process happening. Cavitation also occurs in traumatic brain injuries, such as concussions, where low pressures cause the cerebrospinal fluid to cavitate which can contribute to brain damage (Canchi *et al.*, 2017). Other applications include needle-free injections (Oyarte Gálvez *et al.*, 2020), lithotripsy to disintegrate kidney and gall stones (Brennen, 2003), and reducing damaging effects from cavitation that occurs when an energy pulse probe is used in endosurgery (Palanker *et al.*, 2002).

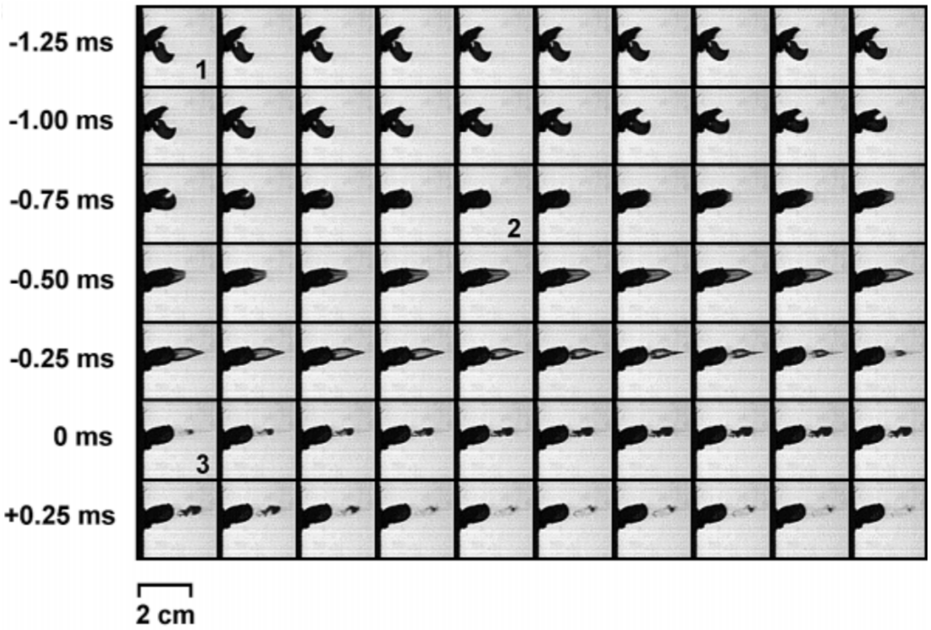

FIGURE 1.2: Frames of high-speed footage of a snapping shrimp jet showing the claw closing, the ensuing jet, and the subsequent expansion and collapse of the bubble (Versluis *et al.*, 2000).

Other novel applications include breaking ice with collapsing bubbles (Cui *et al.*, 2018) and using cavitation to induce compressive residual stresses in metals and alloys (Sonde *et al.*, 2018), a similar process to shot peening.

Many of these applications involve complex geometries, either as a direct consequence of the application or as a potential design variable. In the following three sections, cavitation literature is reviewed with increasing geometric complexity.

1.2 Cavitation in an infinite fluid

Rayleigh (1917) is widely cited as the first significant study of collapsing bubbles, in which equations are developed to describe the growth and collapse of a spherically symmetric cavity in an infinite incompressible fluid with a constant pressure at an infinite distance. Rayleigh's work was subsequently extended by Plesset (1949) to include a time-varying pressure at a distance from the bubble. The resulting equation is the commonly used Rayleigh-Plesset equation which has been applied in numerous studies as a good approximation for the growth and collapse of bubbles (Blake *et al.*, 2015; Supponen *et al.*, 2016), sometimes in modified forms to better suit specific scenarios (Harris, 1996). The following analysis is primarily based on the book by Brennen (1995).

The Rayleigh-Plesset equation is typically written as

$$\frac{p_B(t) - p_\infty(t)}{\rho_L} = R\ddot{R} + \frac{3}{2}\dot{R}^2 + \frac{4\nu_L}{R}\dot{R} + \frac{2S}{\rho_L R}, \tag{1.1}$$

where p_B is the pressure inside the bubble; p_∞ is the far-field pressure; ρ_L and ν_L are the density and kinematic viscosity of the fluid, respectively; S is the surface tension; and R is the radius of the bubble with $\dot{R}$ and $\ddot{R}$ representing the first and second derivatives of the radius with respect to time.

The exact implementation of this equation can vary significantly depending on the assumptions that are made. For example, a thermally driven collapse uses a different formulation than a purely inertial collapse. For an inertial collapse, the gas inside the bubble is often considered to behave polytropically such that the pressure of gas in the bubble is directly related to the volume (Brennen, 1995).

$$p_G = p_{G_0}\left(\frac{R_0}{R}\right)^{3k} \tag{1.2}$$

where p_G is the gas or vapour pressure and k is the polytropic constant. Subscript 0 denotes the initial conditions. For the research presented in this thesis, the bubble collapse events occur too quickly for significant heat transfer across the bubble boundary. Thus the gas is assumed to be isentropic and the polytropic constant is equal to the ratio of specific heats, $k = \gamma$. This leads to the following formulation of the Rayleigh-Plesset equation

$$\frac{p_V(t) - p_\infty(t)}{\rho_L} + \frac{p_{G_0}}{\rho_L}\left(\frac{R_0}{R}\right)^{3k} = R\ddot{R} + \frac{3}{2}\dot{R}^2 + \frac{4\nu_L}{R}\dot{R} + \frac{2S}{\rho_L R}, \tag{1.3}$$

which uses the relationship $p_B = p_V + p_G$, where p_V is the vapour pressure of the liquid.

An important analytic result from these equations is the time required for total collapse of the bubble from $R = R_0$ to $R = 0$, known as the Rayleigh collapse time,

$$t_{TC} = 0.915 \left(\frac{\rho_L R_0^2}{p_\infty - p_V} \right)^{\frac{1}{2}}, \tag{1.4}$$

which, although only an approximation (neglecting compressibility, surface tension, gas contents, and viscosity), provides a useful scale for time during a bubble collapse (Brennen, 1995). Notably, R_0 refers to the maximum radius of the bubble as we assume here that the bubble starts at its maximum radius.

A non-dimensional form of the Rayleigh-Plesset equation may be formulated by normalising R with the maximum bubble radius, R_0, and the time, t, with the Rayleigh collapse time, t_{TC}.

$$\mathrm{Eu} = \bar{R}\ddot{\bar{R}} + \frac{3}{2}\dot{\bar{R}}^2 + \frac{4}{\mathrm{Re}}\frac{\dot{\bar{R}}}{\bar{R}} + \frac{2}{\bar{R}\mathrm{We}} \tag{1.5}$$

where $\bar{R} = \frac{R}{R_0}$, $\dot{\bar{R}} = \frac{\mathrm{d}\bar{R}}{\mathrm{d}\bar{t}}$, $\ddot{\bar{R}} = \frac{\mathrm{d}^2\bar{R}}{\mathrm{d}\bar{t}^2}$, $\bar{t} = \frac{t}{t_{TC}}$, $\mathrm{Eu} = \frac{p_B - p_\infty}{\rho_L u^2}$, $\mathrm{Re} = \frac{u R_0}{\nu_L}$, $\mathrm{We} = \frac{\rho_L R_0 u^2}{S}$, $u = \frac{R_0}{t_{TC}}$

Figure 1.3 shows a numerical solution to equations 1.3 and 1.5. The fluid is assumed to be water at 20°C ($p_V = 2.3388$ kPa, $\rho_L = 997\,\mathrm{kg\,m^{-3}}$, $\nu_L = 1.003\mathrm{e}-6\,\mathrm{m^2\,s^{-1}}$, $S = 0.0728$ $\mathrm{N\,m^{-1}}$). The bubble has an initial radius $R_0 = 2$ mm (representative of the bubbles in this investigation) and an initial internal pressure equal to the vapour pressure $p_{G_0} = p_V$. At an infinite distance the pressure is $p_\infty = 100$ kPa. Here we assume that p_V and p_∞ are constants. This results in a collapse time $t_{TC} = 185$ μs, Reynolds number $\mathrm{Re} = 21\,569$, Weber number $\mathrm{We} = 3205$, and pressure ratio of $p_{G_0}/(p_\infty - p_V) = 0.0239$. Under these conditions the bubble initially collapses before rebounding and repeating the cycle. Due to the minor viscous effects the bubble does not completely recover its initial radius in subsequent expansions. In reality, these viscous effects are very small, as indicated by the high Reynolds number present in the system. The effects of surface tension are also relatively small, as indicated by the high Weber number. Thus, for the analysis in this thesis, both viscous effects and surface tension effects will be neglected.

The Rayleigh-Plesset equation has been further extended by the work of Keller & Miksis (1980). The Keller-Miksis equation additionally models the compressibility of water which becomes necessary during the very rapid stages of bubble collapse. Whereas the Rayleigh-Plesset equation shows bubbles rebounding to nearly their full size, the Keller-Miksis model demonstrates the decreasing radius of rebounds. Neglecting surface tension and viscosity, the Keller-Miksis equation can be written (Trummler *et al.*, 2021) as

$$\frac{p_V(t) + p_G - p_\infty(t)}{\rho_L}(1 + v) + \frac{R\dot{p}_G}{\rho_L c_L} = R\ddot{R}(1 - v) + \frac{3}{2}\dot{R}^2(1 - \frac{v}{3}) \tag{1.6}$$

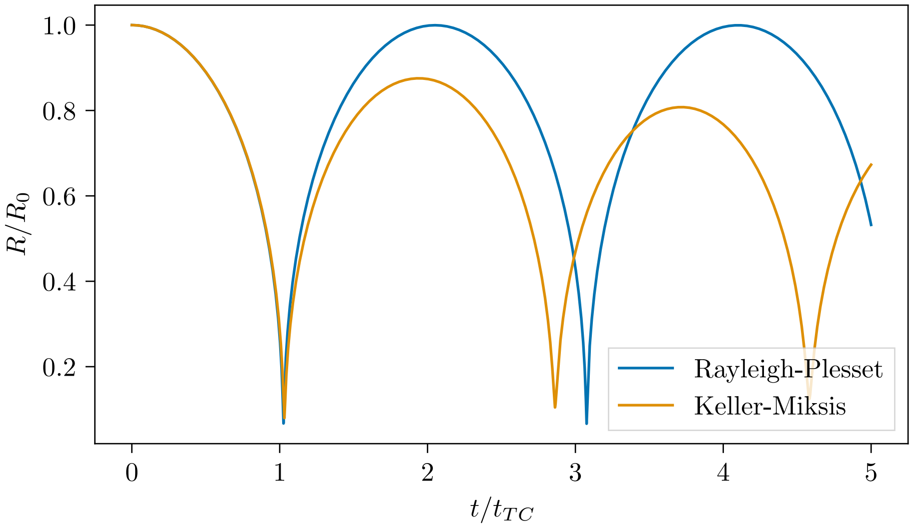

FIGURE 1.3: A numerical solutions to the Rayleigh-Plesset equation and Keller-Miksis equation showing the bubble radius (normalised by the initial radius) plotted against time (normalised by the Rayleigh collapse time).

where c_L is the speed of sound in the liquid and $v = \dot{R}/c_L$. This is largely similar in form to equation 1.3. For clarity, p_G here is not substituted by equation 1.2. Using the same conditions as the Rayleigh-Plesset solution, with $c_L = 1480$ m s^{-1}, a numerical solution to the Keller-Miksis equation is shown alongside the Rayleigh-Plesset solution in figure 1.3. Most notably, compared to the Rayleigh-Plesset solution, the bubble no longer recovers its full size after each rebound.

The rebound radius in this model depends on the driving pressure $\Delta p = p_\infty - p_V$ and the initial partial pressure of non-condensable gas inside the bubble p_{G_0}. This agrees well with the work of Akhatov *et al.* (2001), who produced a more complete numerical model including some thermal effects; the effects of condensation, evaporation, and compressibility; and greater attention to the properties and dynamics of the internal gas. They showed that the effect of diffusion into the bubble is negligible but that a small amount of non-condensable gas inside the bubble can significantly increase the rebound size by reducing the condensation of vapour on the bubble surface. They suggested that the recombination of the initial plasma could be a key factor in the non-condensable gas content of a laser-induced cavitation bubble.

However, despite its importance to the resulting dynamics of the bubble, a method for directly measuring the non-condensable gas inside a bubble has not yet been developed. Tinguely *et al.* (2012) estimated the non-condensable gas content by fitting a Keller-Miksis model to their experimental data. They showed that the energy in the bubble after collapse is partitioned between the bubble rebound and the emitted shock-waves. They further showed, as expected from the Keller-Miksis equation, that this partition depends on the pressure in the liquid and the non-condensable gas content of the bubble, among other properties of the liquid and gas.

More recently, Trummler *et al.* (2021) numerically investigated the effect of non-condensable gas on bubble collapse dynamics. They showed good agreement with the work of Tinguely *et al.* (2012) and further showed that the observed effects of non-condensable gas extend to bubbles collapsing in close proximity to a solid boundary. However, as with previous studies, they highlight the uncertainty around the amount of non-condensable gas present in practical applications. Despite being a significant factor in the dynamics of bubble collapse and rebounds, this remains an open question. This issue becomes relevant to the present work in chapter 4 and chapter 5, where the bubble rebound size is measured and bubble displacement is measured during rebound.

1.3 Cavitation near a flat boundary

In an infinite fluid, as previously discussed, bubbles collapse with spherical symmetry. As they collapse they draw in the surrounding fluid. When a solid rigid boundary is introduced near the bubble, it is more difficult for the bubble to draw fluid in from the boundary side as the boundary is 'impeding' the flow (Blake, 1983). This causes the fluid on the boundary side of the bubble to be drawn in slower, reducing the speed of the bubble surface collapse on that side. This asymmetry causes the bubble to translate towards the boundary and can cause the bubble to produce a high speed jet (Plesset & Chapman, 1971; Blake *et al.*, 1986).

A nearby free surface, such as the boundary between water and air, has the opposite effect of a solid boundary. The free surface deforms, making it easier to draw fluid from that side of the bubble, producing a lower relative impedance. This causes the jet to be directed away from the free surface. However, for very large bubbles, buoyancy can be a more dominant effect. In addition to the effects that occur with rigid boundaries, bubbles expanding near free surfaces may also produce jets at the surface due to rapid expansion (Blake *et al.*, 1987). The rapid expansion of bubbles can be harnessed to produce very high speed, controlled jets which have many potential applications, such as needle-free injectors (Oyarte Gálvez *et al.*, 2020).

Deformable surfaces present another range of behaviours depending on how easy they are to deform. Stiff boundaries, or boundaries with high inertia, act similarly to a rigid boundary by impeding the flow to the bubble. Conversely, if the boundary can easily deform, it becomes easier to deform the boundary than to draw in fluid so the boundary acts similarly to a free surface. This means that the jet may be weaker than a rigid boundary or be directed away from the boundary (Gibson & Blake, 1982). Even more complex behaviour has been investigated for cavitation near elastic gels (Brujan *et al.*, 2001*a*,*b*). Depending on the water content of the gel, and thus the elastic modulus, bubble deformation was observed to vary greatly and jets were directed towards the boundary, away from the boundary, or both.

Bubble collapses occur on a very short time scale such that viscous effects can be neglected, as demonstrated in section 1.2. For the majority of the collapse the fluid can also be treated as incompressible. This allows potential flow models to be applied to describe the flow. During the growth and collapse phases, while the bubble remains mostly spherical, the bubble can be treated as a source or sink. By mirroring the bubble in the boundary plane, the no-penetration boundary condition is achieved along the whole boundary. Both a solid boundary and a free surface can be modelled using the method of images (Blake *et al.*, 1987; Kucera & Blake, 1990). In the case of a free surface, the image sink has the opposite sign to the bubble sink. This configuration is shown in figure 1.4. Note the flow parallel to the boundary, stagnation point at the center of the boundary, and higher speeds closer to the bubble.

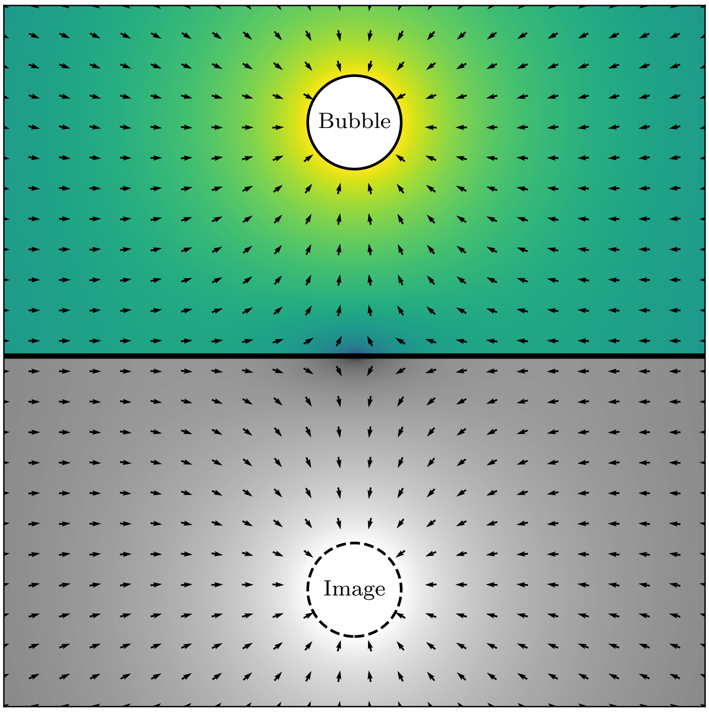

FIGURE 1.4: A schematic of the method of images. A bubble, represented as a sink, is reflected in the plane of a boundary, producing an image sink. The domain of interest is shown in colour and the image domain is shown in greyscale. Arrows show the direction of flow and the logarithm of the flow speed is shown in the background contour.

Despite the significant differences between the ideal case for which the Rayleigh-Plesset equation was derived and most realistic scenarios, the Rayleigh-Plesset equation provides a reasonable approximation for the scales involved in bubble growth and collapse. Figure 1.5, from Supponen *et al.* (2015), shows a comparison between experimental data for bubble collapse near a flat boundary and the Rayleigh-Plesset equation.

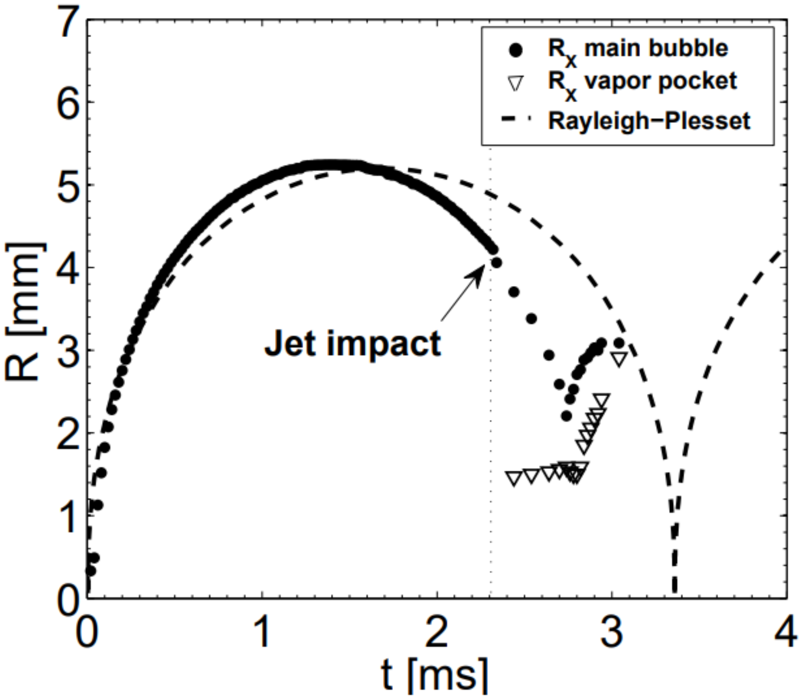

FIGURE 1.5: A comparison between experimental data and a Rayleigh-Plesset equation solution near a flat boundary. This is figure 2(*a*) in Supponen *et al.* (2015).

Flat, rigid boundaries have been the primary focus of research studying the effects of cavitation as they are the simplest geometry for which the complex dynamics can be observed. These studies have included the mechanisms and measurement of bubble cleaning (Ohl *et al.*, 2006; Verhaagen & Fernández Rivas, 2016; Reuter & Mettin, 2016), damage induced by bubble collapses (Dular *et al.*, 2019; Sagar & el Moctar, 2020), analysis of pressure fields during bubble collapse and jetting (Li *et al.*, 2016), and measurements of shear stress induced on the boundary (Dijkink & Ohl, 2008; Koukouvinis *et al.*, 2018). Of particular note, Zhao *et al.* (2008) show that, for very low standoff distances, the acoustic transient contributes more to the reduction in rebound energy than the liquid jet.

An important factor when considering how a collapsing bubble interacts with a boundary is the strength of the collapse asymmetry. This is typically discussed in terms of the Kelvin impulse; Benjamin & Ellis (1966) describe it thus "*the impulse associated with a moving bubble presents much the same intuitive physical picture as the momentum of a rigid projectile in free space*". Blake *et al.* (2015), continuing from several prior papers (Blake & Cerone, 1982; Blake, 1983, 1988), present equations for the Kelvin impulse for rigid boundaries, free surfaces, two fluid interfaces, and inertial boundaries as well as a buoyancy term. Supponen *et al.* (2016) present a dimensionless equivalent of the Kelvin impulse called the anisotropy parameter, ζ. For a solid boundary this parameter is calculated by the equation

$$\zeta = 0.195\gamma^{-2} \tag{1.7}$$

where γ is the standoff distance Y/R_0. Y is the distance from the boundary and R_0 is the maximum bubble radius. This is equation 2.5 in Supponen *et al.* (2016). They then measure various jet parameters as functions of the anisotropy parameter and show that the anisotropy parameter is valid for various different 'jet drivers' including buoyancy, flat rigid surfaces, flat free surfaces, stationary potential flow, a liquid interface, and an inertial boundary. Supponen *et al.* (2018) expands on these jet parameters to include the ratio of energy between the first two bubble collapses. This ratio is also shown to be a function of the anisotropy parameter.

1.4 Cavitation near complex geometries

Although flat boundaries are easy to study, real systems are rarely so simple and more complex boundaries introduce additional complexity to the bubble dynamics. Complex geometries have been a focus of recent research. Some examples of complex geometries are shown in figure 1.6 and are a series of concave corners (Tagawa & Peters, 2018), square and triangular channels (Molefe & Peters, 2019), an axisymmetric curved surface (Tomita *et al.*, 2002) and the slot geometry investigated in chapter 3.

Most studies on complex geometries have used experimental techniques to observe bubble dynamics. Some studies rely solely upon experimental results such as research on ridge-patterned structures (Kim & Kim, 2020), a combination of a free surface and inclined flat plate (Zhang *et al.*, 2017), and a perpendicular corner geometry (Brujan *et al.*, 2018). Although experimental results are very useful for capturing bubble dynamics, they are sometimes unable to capture the underlying mechanisms that could be understood more thoroughly with a combination of experimental results and numerical modelling. As an example, the jet direction behaviour in a corner geometry can be modelled using a method of images technique which has been presented by Kucera & Blake (1990) and then expanded upon and validated by Tagawa & Peters (2018). Brujan *et al.* (2018) makes a linear fit between the jet angle and the ratio of distances to the two walls. However, Tagawa & Peters (2018) showed that the method of images provides a better fit to experimental results. In addition to allowing a better understanding of underlying mechanisms and relationships, numerical results can also investigate much broader parameter spaces if the techniques employed are sufficiently inexpensive.

There is not yet a standard approach to investigating complex geometries. It is suggested in Supponen *et al.* (2016) that the anisotropy parameter for a bubble with a combination of jet drivers, such as gravity, pressure gradients, and nearby boundaries, is the vector summation of anisotropy parameters for the jet-drivers. This would allow for complex combinations of jet drivers to be modelled, including complex boundary geometries. However, it is also suggested that this may not hold for complex geometries. By comparing this to the solution for a corner (Tagawa & Peters, 2018), it is clear that this solution does not accurately capture the direction of the jet so it cannot be used in such a simple manner.

More confined geometries have also been investigated, such as those used for needle-free injections (Oyarte Gálvez *et al.*, 2020) or quasi-2D geometries such as those found in some microfluidic devices (Zwaan *et al.*, 2007).

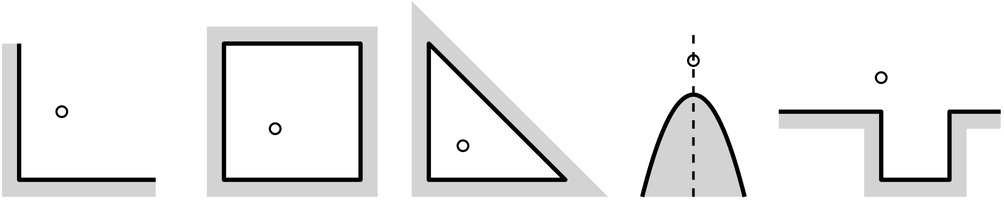

FIGURE 1.6: Examples of complex geometries. From left to right: a concave corner, a square channel, a triangular channel, an axisymmetric curved surface, and a slot geometry.

1.5 Experimental methods

Gas and vapour bubbles that behave this way can be generated by a large range of mechanisms. One of the most common is low pressures such as those that occur near ship propellers (van Terwisga *et al.*, 2007), due to rapid acceleration (Pan *et al.*, 2017), or the low pressure regions generated for ultrasonic cleaning (Brennen, 1995). However, for the study of cavitation dynamics, these mechanisms can be difficult to harness as the exact location of bubbles may be hard to predict and individual bubbles are hard to isolate. Many experiments use spark-gap generated bubbles where the high temperature spark causes the nearby water to vaporise, leading to a bubble (Zhang *et al.*, 2017; Li *et al.*, 2018; Kim & Kim, 2020). Laser-induced cavitation behaves similarly by using a focused laser to generate the bubble (Brewer & Rieckhoff, 1964; Lauterborn, 1972; Noack & Vogel, 1999). These techniques allow individual bubbles to be isolated and carefully positioned. Podbevšek *et al.* (2021) conducted an evaluation of these techniques, categorising a wide variety of advantages and drawbacks of each technique. Figure 1.7 shows a range of different techniques investigated in their work.

A key limitation in observing bubble collapse is the very short timescale on which the collapse occurs. Using equation 1.4, the initial collapse of a 2 mm radius bubble, prior to any rebounds, would take approximately 0.185 ms. Observing this collapse therefore requires approximately 10 000 frames per second to even see the collapse occur, with much higher frame rates required to observe and measure more detailed phenomena. Some studies report using frame rates of *"up to 10 million frames per second"* (Supponen *et al.*, 2016) while others report use of a camera system capable of achieving frame rates of 25 million frames per second (Chin *et al.*, 2003; Sijl *et al.*, 2010).

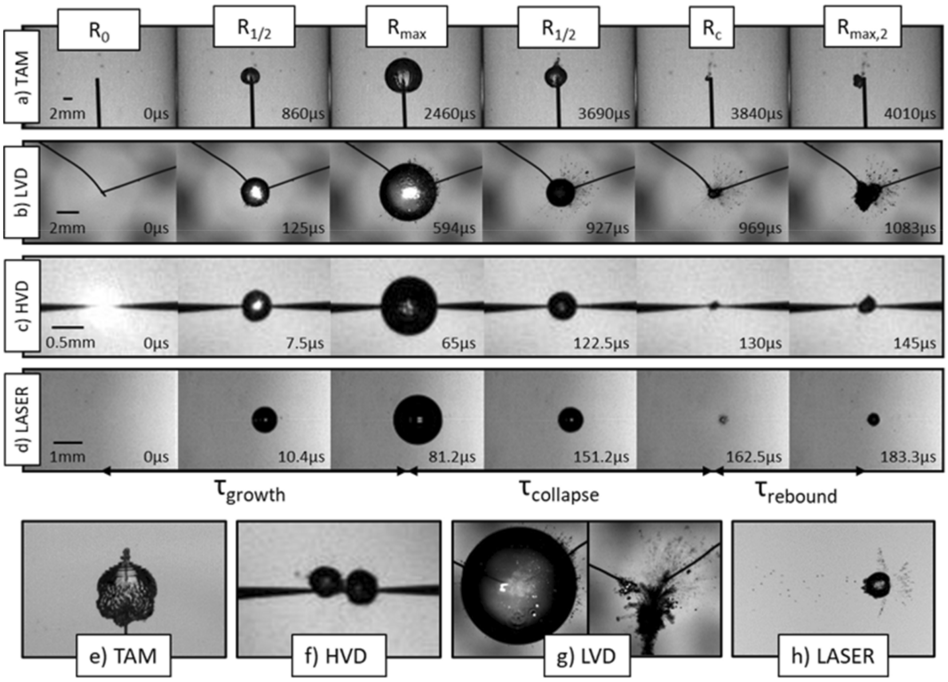

FIGURE 1.7: Figure 7 from Podbevšek *et al.* (2021) showing bubbles created by "tube arrest method" (TAM), "low-voltage discharge" (LVD), "high-voltage discharge" (HVD), and "laser-induced bubble" (LASER). (*a*-*d*) Frames from high-speed recordings of experiments. (*e*) Surface instabilities and small jets caused by TAM. (*f*) Double bubble rebound in HVD. (*g*) Electrode breakup with LVD. (*h*) Expansion of microbubbles caused by the initial shockwave from a laser-induced bubble.

As the bubble collapse is a pressure-driven event, hydrostatic pressure must be considered. Although in many cases it can be considered negligible (Tagawa & Peters, 2018), some studies go to great lengths to remove the influence of gravity in order to measure the other effects very precisely. Some experiments have been performed during parabolic flights such that a very low gravity environment can be maintained for a short period of time (Obreschkow *et al.*, 2011; Supponen *et al.*, 2016). A similar effect can be achieved more simply by performing the experiment during a short free fall drop (Blake & Gibson, 1981). Using the buoyancy parameter of Blake *et al.* (1986), the effect of buoyancy can be compared to a nearby plate. The buoyancy parameter is defined as

$$\delta = \pm\sqrt{\frac{\rho_L g R_0}{p_\infty - p_V}} \tag{1.8}$$

where g is the gravitational acceleration. Taking $\rho_L = 997$ kg m^{-3}, $g = 9.81$ m s^{-2}, an initial radius $R_0 = 2$ mm, and pressure difference of $p_\infty - p_V = 97.7$ kPa, the buoyancy parameter is $\delta = 0.014$. Blake *et al.* (1986) found the relation $\gamma\delta = 0.442$ for bubbles under equal influence from buoyancy and a nearby boundary. Using this relation, the effect of buoyancy would become equal at a standoff distance of $\gamma \approx 32$, which is far beyond the range of our experiments and thus a negligible effect.

1.6 Numerical modelling

The method of images can be used for some limited complex geometries. Mirror sinks of differing strengths produce a curved boundary (Tomita *et al.*, 2002). Additional boundaries can also be created by introducing more mirror planes. This can be used to model a limited set of concave corner geometries (Kucera & Blake, 1990; Tagawa & Peters, 2018; Wang *et al.*, 2020) and some interior geometries such as rectangular and triangular channels (Molefe & Peters, 2019). Thus far, most research using this technique has focused on geometries with a constant two-dimensional cross-section. However, the method of images could be used to investigate more complex three-dimensional shapes. One key limitations to this technique is that images must not be mirrored into the domain of interest, which limits non-tessellating and convex geometries. Kucera & Blake (1990) avoid this limitation by solving the equations on a Riemann space to model a semi-infinite plate. Despite its limitations, the method of images has proven to be fast and reliable for the geometries that it can be applied to.

Another commonly applied family of methods are boundary integral and boundary element methods (Brebbia & Dominguez, 2001). Instead of relying on mirrored sinks to achieve the necessary boundary conditions, these methods represent boundary conditions as a distribution of sinks (or some more complex potential flow elements). In the case of boundary integral methods, the boundary conditions are represented by integral equations, that are then discretised into a form similar to boundary element methods. These methods have widely been applied to numerically modelling the evolution of the bubble surface over time (Blake & Gibson, 1987; Harris, 1992; Zhang & Liu, 2015; Chahine *et al.*, 2016; Supponen *et al.*, 2016; Wang *et al.*, 2020). An example boundary element method simulation is shown in figure 1.8. Harris (1996) uses a boundary element method to model a series of complex geometries, and attempts to resolve the Kelvin impulse using a more complex version of the Rayleigh-Plesset equation. The results are compared to results obtained using a modified Green's function but are not validated against experimental results. These methods provide a relatively inexpensive and accurate way of predicting bubble dynamics in a wide range of scenarios, however they are unable to model some of the more complex dynamics such as shockwaves.

Far more complex and vastly more expensive simulations have been applied in order to better resolve the full bubble dynamics. These often involve the volume of fluid method (Zeng *et al.*, 2018; Koukouvinis *et al.*, 2016; Han *et al.*, 2018; Koukouvinis *et al.*, 2018; Lechner *et al.*, 2019; Gonzalez-Avila *et al.*, 2020*a*), often in combination with the finite volume method, although other systems have been applied (Zhang *et al.*, 2019; Sagar & el Moctar, 2020). These methods are able to more completely capture the bubble dynamics, but have a relatively high computational cost. As such, they become

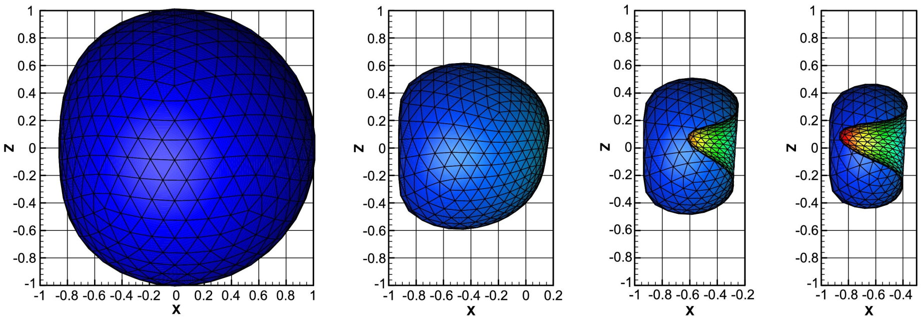

FIGURE 1.8: An example boundary element method simulation of a bubble collapsing near a solid wall. This is part of figure 16 from Zhang & Liu (2015).

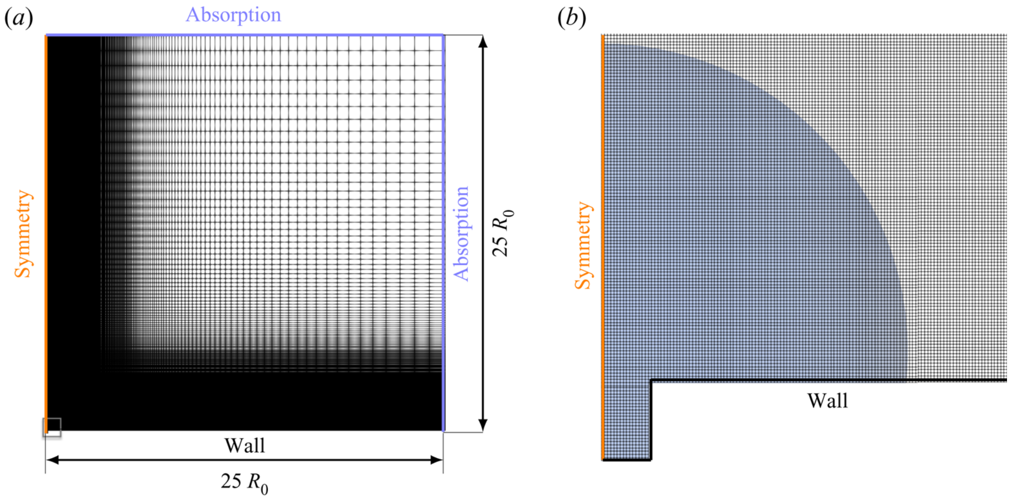

FIGURE 1.9: (*a*) An example mesh of a simulation of a bubble collapsing near a crevice. (*b*) Magnified view showing every fourth grid line. This is figure 3 from Trummler *et al.* (2020).

prohibitively expensive when investigating larger parameter spaces such as those required for investigating the effects of complex geometries on bubble collapse. An example mesh is shown in figure 1.9.

1.7 Research problem

This research project focuses on understanding how complex geometries influence the dynamics of bubble collapse. By better understanding these mechanisms, geometries can be designed to reduce or enhance the effects of bubble collapses as desired.

We investigate two fundamental geometries for which little research has been conducted: slot geometries and porous plates. The slot geometry can be considered a prototypical example of any surface with some portion removed such as channels, scratches, or gaps between parts. The porous plates extend this idea in the direction of porous materials such as filters.

In this research, we employ experimental methods and develop simple numerical models to gain insight into these geometries and provide a low-cost numerical model for investigating other complex geometries.

1.8 Thesis structure

The remainder of this thesis is structured as follows. Chapter 2 outlines the experimental methodologies applied to this research. Then, the main investigation is comprised of three sections. Firstly, the jet directions of bubbles collapsing near slot geometries are investigated in chapter 3. As part of this investigation a simple numerical model is developed that can predict the direction of the jet. Secondly, the numerical model is further developed in chapter 4 to predict not only the direction of the bubble collapse, but also produce the anisotropy parameter described by Supponen *et al.* (2016). This model is validated with experimental data from a collection of complex geometries. Finally, in chapter 5, bubble displacement and rebound size are investigated near porous plates both experimentally and using a further development of the numerical model. To conclude, the key results are summarised in chapter 6.

Data and code supporting this research are available from the University of Southampton repository at `https://doi.org/10.5258/SOTON/D2506`.

Chapter 2

Experimental measurements of cavitation

In this chapter we outline the experimental methods and analysis techniques used in this research. The objective of the experiments in this work was to produce consistent bubbles at a well-controlled location relative to a given geometry. The methodologies outlined here were applied to the work in chapters 3, 4, and 5.

2.1 Generating bubbles

Experiments were performed in acrylic or glass water tanks with volumes of approximately 3-5 litres. The tanks were filled with partially degassed water to minimise microbubbles present in the water that could cause additional nucleation of bubbles during experiments. Initially, normal tap water was used but later experiments used purified water to eliminate as many possible sources of variation as feasible.

As mentioned in section 1.5, one commonly-used technique is laser-induced cavitation. A laser is focused down to a small volume and, at a critical energy density threshold, this intense input of energy forms a hot plasma (Brewer & Rieckhoff, 1964). This plasma is visible in figure 2.1 and in turn produces a rapidly expanding vapour bubble. This technique allows the use of relatively easy-to-align optical equipment to precisely position bubbles. A Q-switched Nd:YAG laser (‘Bernoulli PIV’ or ‘Nano PIV’, both from Litron Lasers) was used to generate a 6-8 ns pulse at a wavelength of 532 nm.

Geometries were positioned relative to the bubbles using a translation stage with an arm connected to the geometries. This allowed the bubble to be positioned relative to the geometry with an accuracy of 5 μm without having to move or realign the optics.

In this research, two different focusing optics were used: a microscope objective and an off-axis parabolic mirror.

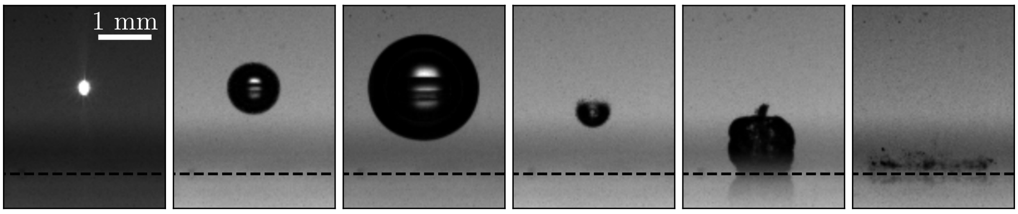

FIGURE 2.1: Frames from a high-speed recording of a bubble collapse. The plasma initially formed by the focused laser is visible in the first frame.

2.1.1 Microscope objective

A microscope objective is typically used to magnify objects, taking an object at the focal point and creating a larger image of it. In this experiment we use the microscope objective in reverse: taking a wide laser beam and focusing it down to a point in the water. We positioned the microscope objective immediately above the water surface such that bubbles were nucleated below it.

In selecting a microscope objective, there exists a trade-off between the working distance and the focusing angle. A wide focusing angle, corresponding to a high numerical aperture, would allow the highest energy density to be restricted to a very small region in order to reduce secondary nucleations along the laser path (Tagawa *et al.*, 2016; Sinibaldi *et al.*, 2019). To achieve a wide focusing angle there must be either a very large optic or a small working distance. At a small working distance the bubble would be nucleated too close to the water surface and the effect of the geometry of interest would not be easily distinguished from the effects of the free surface. Therefore, a numerical aperture was selected that balanced the working distance with the focusing angle.

In this work a Nikon Plan Fluor 10X microscope objective (maximum numerical aperture NA = 0.30) was used to focus the laser to the position where the bubble was created. However, although the optic is rated to a numerical aperture of 0.30, the focusing angle of the beam is also limited by its width entering the objective and so a lower effective numerical aperture is expected. In order to maximise the beam width, a beam expander was used to double the beam diameter.

This optic resulted in the geometry being submerged approximately 25 mm deep below the water surface. The relatively large distances to the tank walls, plate edges, and plate holder mean that their effects on the experiments were negligible. The laser output energy was typically set to 140 mJ per pulse, and then modulated down by adjusting the attenuator setting (typically between 30-35%) to use the minimal level that could produce a bubble. Bubbles typically ranged in diameter from approximately 1 mm to 3 mm.

The typical microscope objective experiment configuration used in this research is shown in figures 2.2 and 2.3.

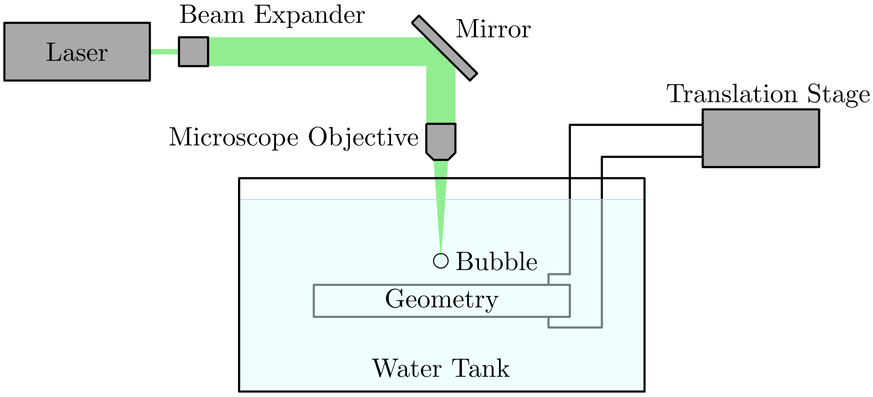

FIGURE 2.2: Diagram of the experiment configuration. In addition to the equipment shown, a high speed camera observes the bubble collapse, which is back-lit by a 100W LED panel.

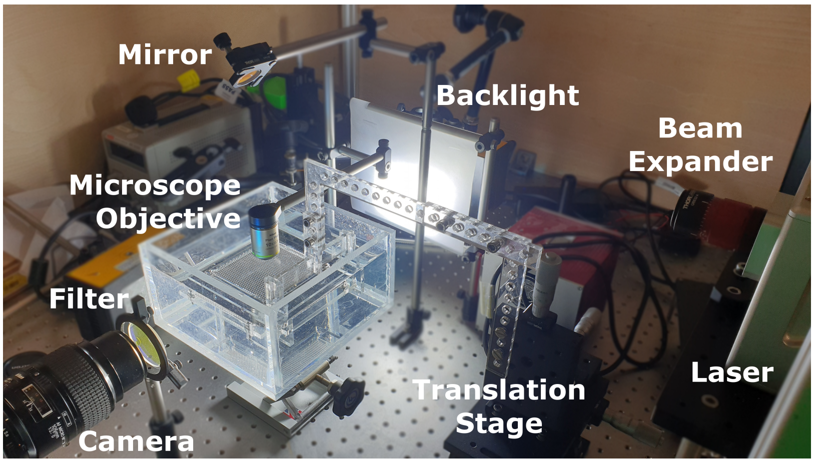

FIGURE 2.3: A photograph showing the experiment configuration shown in figure 2.2.

2.1.2 Off-axis parabolic mirror

A laser directed at a parabolic mirror is focused down to a point in the parabola. An off-axis parabolic mirror is a segment of a parabola, selected such that the laser is focused at an angle away from the axis of the incident laser. Using a sufficiently large mirror, with an expanded beam, this method of focusing can achieve wide focusing angles with relatively large working distances.

Following the example of Obreschkow *et al.* (2013), we implemented an off-axis parabolic mirror setup, as shown in figure 2.4. The principle constraints of the off-axis parabolic mirror setup were the achievable diameter of the laser and the required angle to keep any geometry clear of the laser beam prior to focusing.

The initial laser output energy was approximately 97 mJ and was subsequently attenuated with the attenuator set to between 70 % and 75 %. The beam was restricted by an iris to be approximately 3 mm in diameter, in order to remain well-collimated after expansion, and then expanded with a 10x beam expander to approximately 30 mm in diameter. The expanded beam was focused by a gold off-axis parabolic mirror with a focusing angle of approximately 41 degrees (equivalent numerical aperture = 0.35). The mirror was submerged in the water, so the distance to the water surface was not a concern. This methodology produced bubbles with radii ranging from 1.07 mm to 1.65 mm. Notably, the gold surface absorbed most of the laser energy, but was less likely to degrade when immersed in water when compared to mirror materials designed to operate with a 532 nm laser (Obreschkow *et al.*, 2013). However, a recent study has reported use of an aluminium off-axis parabolic mirror (Sieber *et al.*, 2022) so the degradation concern may not be as significant as originally assumed.

The typical off-axis parabolic mirror experiment configuration used in this research is shown in figure 2.4.

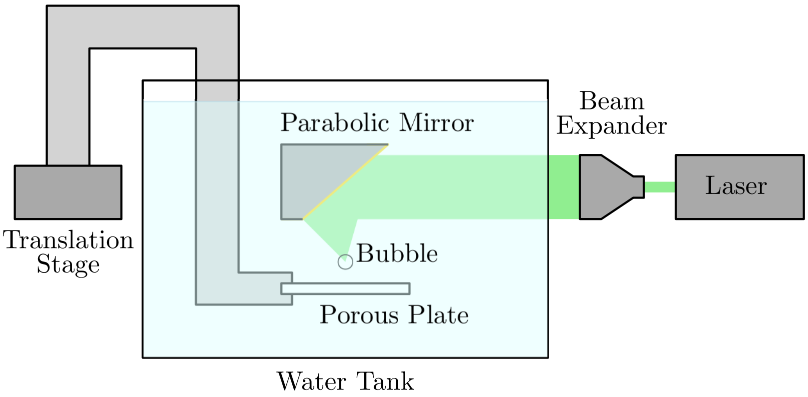

FIGURE 2.4: Schematic showing the experimental setup for laser-induced cavitation using an off-axis parabolic mirror to generate bubbles near a porous plate.

2.1.3 Comparison between optics

The core difference between the two methodologies is the symmetry and size of bubble that is achievable based on the focusing angle. As will be discussed in section 4.4.2, even without significant secondary nucleation, the shape of the bubble varies with the shape of the initial plasma. As the bubble becomes less spherical, the spread of measurements of bubble collapse properties increases. Thus, it is desirable to create the most spherical bubbles possible. Using the microscope objective method, the mean eccentricity of the bubble image at maximum size was 0.23. Using the off-axis parabolic mirror method, this was reduced to 0.13. This allows more precise measurements to be taken, which is necessary for assessing small variations such as those investigated in chapter 5.

In addition to this primary difference, there are some secondary considerations.

Firstly, the off-axis parabolic mirror method produced far more repeatable bubbles. To quantify this, the slots data used in chapters 3 and 4, using the microscope objective method, had a mean bubble radius of 1.09 mm with a standard deviation of 0.12 mm (11 %). In contrast, the porous plates data used in chapter 5, using the off-axis parabolic mirror method, had a mean bubble radius of 1.42 mm with a standard deviation of just 0.04 mm (2.8 %).

Secondly, due to the wider angle of convergence, the laser also diverges faster beyond the focal point when using the off-axis parabolic mirror method. This reduces the concentration of laser energy that impinges on nearby geometries. For transparent geometries this has little effect, but for opaque geometries, this absorbed energy can be important as will be shown in section 5.4.1.

Finally, and the principle downside of the off-axis parabolic mirror, the microscope objective method is much less sensitive to misalignment of the optics. Figure 2.5 shows a ray tracing simulation of the laser being focused by the off-axis parabolic mirror. The inset plots of figure 2.5(*b* and *c*) show zoomed-in views of the focal region. Figure 2.5(*b*) shows the focal region of an aligned mirror and figure 2.5(*c*) shows the focal region of a mirror misaligned by just 1 degree anti-clockwise. It is clear from these diagrams that even very small misalignment can severely compromise the quality of the focal point. In figure 2.5(*b*), the laser is focused to a single point of maximum energy density at which a bubble would be nucleated. However, in figure 2.5(*c*), the maximum energy density is spread across the left edge of the focal region which would result in a range of possible nucleation points. Figure 2.5(*d*) is from a frame of a high-speed recording of bubble formation and collapse. The bright region in this frame follows the laser path and appears to indicate regions of higher laser concentration, although the exact source of this light is unclear as the laser wavelength is filtered out. This frame shows two bubbles being simultaneously nucleated at a point away from the desired focal point due to the visible misalignment.

2.2 Recording

In both cases, a Photron FASTCAM SA-X2 high speed camera was used to record the bubble collapse. The camera recorded at 100 000 frames per second and used a 105 mm Nikon Micro-Nikkor lens. A 550 nm longpass filter was used to protect the camera from the laser. The camera triggered the laser to ensure accurate synchronising of the recording and the bubble collapse. For each experiment, 100 frames were recorded,

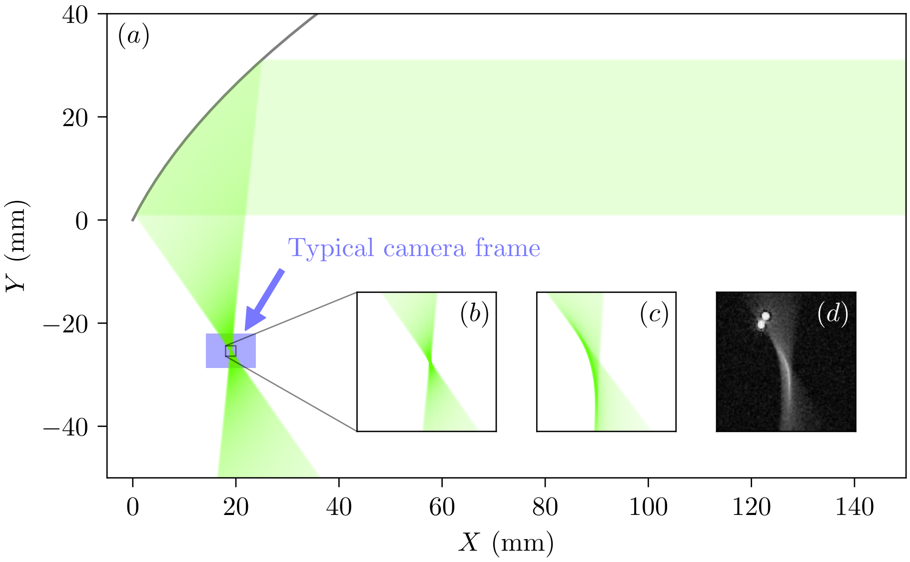

FIGURE 2.5: (*a*) Two-dimensional ray tracing simulation of a laser being focused by a parabolic mirror. The typical size of a camera frame is indicated for comparison. (*b*) A zoomed-in view of the focal area of the simulation in (*a*). (*c*) A zoomed-in view of the focal area of a similar simulation with a mirror misaligned by 1 degree anti-clockwise. (*d*) Part of a frame from a high-speed recording with the background subtracted showing a poorly-aligned focal region during plasma formation.

spanning 1 ms of time. A 100 W LED panel was used to back-light the bubble collapse such that the bubble appears dark on a light background in the recorded images.

2.3 Image processing

2.3.1 Bubble measurement

Image processing techniques were used to extract data from the recorded movies. The background was removed by subtracting each frame from the very first frame, which has no bubble, to produce a white bubble on a black background (figure 2.6*b*). A threshold filter was applied to convert the isolated bubble image into a binary array of pixels (figure 2.6*c*). A binary opening operation was performed that works to remove small objects from around the bubble such as small additional bubbles (applied in figure 2.6*d* although in this case it changes very little). The resulting image typically has a hole in the center of the bubble, caused by the back-light being refracted through the bubble. This hole was filled (figure 2.6*e*) and any additional small objects in frame were also removed (figure 2.6*f*). The bubble area was then measured as the total number of white pixels in the image and the position was calculated as the centroid of these pixels.

This analysis was repeated for each frame of a recording. The bubble radius was determined by assuming a spherical bubble such that $R = \sqrt{A/\pi}$ where R is the bubble

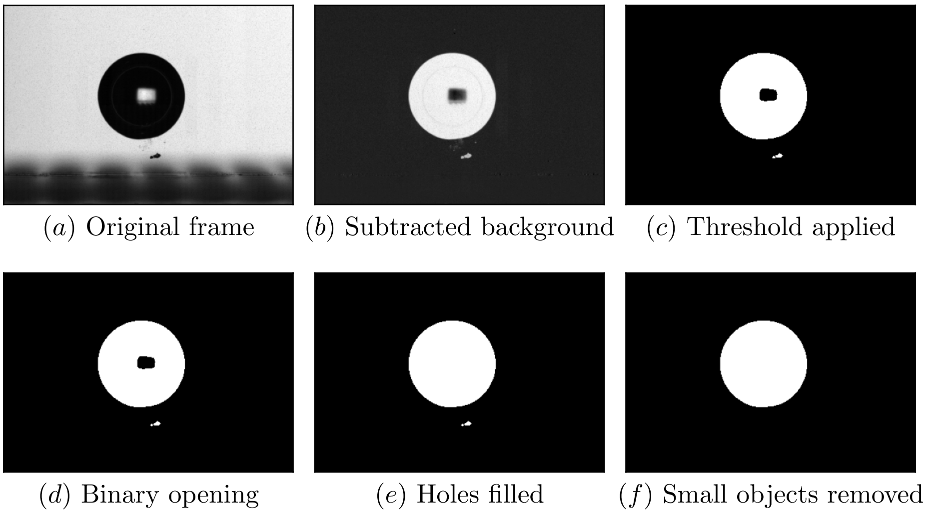
(a) Original frame (b) Subtracted background (c) Threshold applied

(d) Binary opening (e) Holes filled (f) Small objects removed

FIGURE 2.6: An example of each step of the image processing used to measure the bubble position and size.

radius and A is the bubble area in frame. Thus, a plot of bubble radius over time was produced as in figure 2.7(*b*). The spherical bubble assumption holds reasonably well for bubbles near their first and second size peaks as shown in figure 2.7(*a*). When the bubble is not spherical, this can simply be taken as an equivalent bubble radius. The position of the bubble centroid and the radius of the bubble were measured at the first two bubble size maxima to give a displacement direction, dimensionless displacement distance Δ/R_0, and dimensionless rebound size R_1/R_0. These measurements are shown in figure 2.7(*c*). The direction is investigated in chapter 3 and the distance and rebound size are investigated in chapters 4 and 5.

2.3.2 Calibration

The movement of the background geometry in frame between different bubble positions was used to calibrate the size of objects in the frame. The translation stage moved the geometry perpendicular to the camera frame so the known translation distance could be compared to the distance moved in the image to provide a measurement of millimetres per pixel of the image. This technique was applied across multiple frames to provide an accurate calibration. This calibration technique was compared to placing an object of known size (callipers set to 1 mm) in the frame and measuring the pixels manually. The translation-based technique was at least as accurate and required far fewer manual measurements.

These calibrations were applied to the area and translation data to provide physical sizes and distances and were also used to measure geometry in the recorded frames.

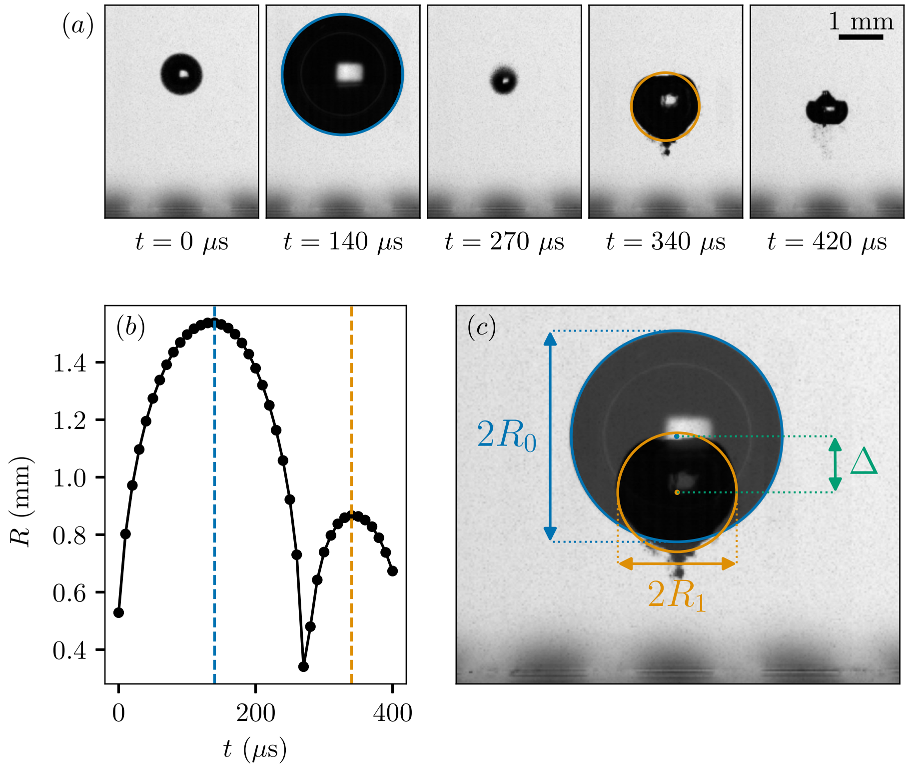

FIGURE 2.7: (*a*) Cropped frames of a bubble collapsing near a boundary. Circles with area equal to the bubble are shown for each of the size maxima ($t = 140$ μs and $t = 340$ μs). (*b*) Plot showing the measured bubble radius for the measured time span. (*c*) Composite of the two size maxima frames with equivalent circles and measured parameters annotated. R_0 is the initial maximum bubble radius. R_1 is the maximum bubble radius during the rebound. Δ is the displacement of the bubble centroid between the first and second bubble maxima.

Chapter 3

Bubble collapse near slot geometries

This chapter is based on a paper that has been published in Journal of Fluid Mechanics (Andrews et al., 2020). Experimental data gathering and preliminary analysis for this paper were performed as part of an internship prior to beginning the current programme.

3.1 Abstract

The collapse of a gas or vapour bubble near a solid boundary produces a jet directed towards the boundary. High surface pressure and shear stress induced by this jet can damage, or clean, the surface. More complex geometries will result in changes in collapse behaviour, in particular the direction of the jet. The majority of prior research has focused on simple flat boundaries or cases with limited complexity. There is currently very little known about how complex geometries affect bubble collapse. We numerically and experimentally investigate how a slot in a flat boundary affects the jet direction for a single bubble. We use a boundary element model to predict how the jet direction depends on key geometric parameters and show that the results collapse to a single curve when the parameters are normalised appropriately. We then experimentally validate the predictions using laser-induced cavitation and compare the experimental results to the predicted dependencies. This research reveals a tendency for the jet to be directed away from a slot and shows that the jet direction is independent of slot height for slots of sufficient height.

3.2 Introduction

The collapse of a gas or vapour bubble near a solid boundary forms a liquid jet that impinges on the boundary (Plesset & Chapman, 1971). The impinging jet can damage, or clean, the boundary surface due to the pressure and wall shear stress induced at the boundary (Dijkink & Ohl, 2008; Koukouvinis *et al.*, 2018). In addition to the jet impingement, shock waves emitted during collapse events may contribute to the effects on the boundary, however it is not clear in which regimes the jet or shock waves are more dominant (van Wijngaarden, 2016). Studying the collapse of single bubbles is a valuable tool for understanding the mechanics involved as the effects of the jet are the result of individual bubble collapses (Benjamin & Ellis, 1966). An understanding of individual bubble collapses can also inform investigation of cavitation erosion caused by many individual collapse events building up over time (Fernandez Rivas *et al.*, 2013). Some common areas in which these bubbles occur are cavitation damage (Sreedhar *et al.*, 2017), hydraulic systems (Luo *et al.*, 2016), and ultrasonic cleaning (Verhaagen & Fernández Rivas, 2016).

Developing a better understanding of the effects of cavitation collapse can increase the lifespan of components such as ship propellers (van Terwisga *et al.*, 2007) and tidal turbines (Kumar & Saini, 2010) or determine the effectiveness of ultrasonic cleaning for complex geometries (Verhaagen *et al.*, 2016; Reuter *et al.*, 2017). There are also numerous applications in biomedical fields such as reducing tissue damage during surgery (Palanker *et al.*, 2002), investigating mechanisms of cell death in cases where cavitation could be used for drug delivery (Dijkink *et al.*, 2008), using cavitation to facilitate needle-free injections (Oyarte Gálvez *et al.*, 2020), and studying the contribution of cavitation in traumatic brain injuries (Canchi *et al.*, 2017) where cavitation is induced by high accelerations (Pan *et al.*, 2017). More novel applications of cavitation include producing high speed liquid jets at small scales (Karri *et al.*, 2012), using cavitation as an ice-breaking mechanism (Cui *et al.*, 2018), and understanding biological mechanisms such as those employed by the snapping shrimp (Versluis *et al.*, 2000; Shimu *et al.*, 2019).

The majority of prior experimental research has focused on the jet dynamics near simple flat boundaries (Benjamin & Ellis, 1966; Plesset & Chapman, 1971; Kucera & Blake, 1990; Dijkink & Ohl, 2008; Supponen *et al.*, 2016) or cases with limited complexity such as axisymmetric boundaries (Tomita *et al.*, 2002) or parallel boundaries (Han *et al.*, 2018; Gonzalez-Avila *et al.*, 2020*a*). Although understanding how bubbles behave near simple geometries is important, in reality geometries have many more complex features such as corners, indentations, slots, and surface imperfections. For this reason further investigation of complex geometries is important.

Some more complex geometries have been studied, such as parallel boundaries closed at one end (Brujan *et al.*, 2019), semi-infinite boundaries (Kucera & Blake, 1990), near combinations of a free surface and an inclined flat boundary (Zhang *et al.*, 2017), inside a set of concave corners (Kucera & Blake, 1990; Brujan *et al.*, 2018; Tagawa & Peters, 2018; Wang *et al.*, 2020), and inside rectangular and triangular channels (Molefe & Peters, 2019). A recent experimental study has investigated how a ridge-patterned structure can affect the bubble surface evolution and jet dynamics when a bubble is generated on the ridge and between the ridges (Kim & Kim, 2020). There have also been investigations into related phenomena such as the behaviour of ultrasonically driven bubble clouds near larger bubbles trapped on pit geometries (Stricker *et al.*, 2013) and bubble collapse dynamics in microfluidic systems of channels with various shapes (Zwaan *et al.*, 2007).

Studies on more complex geometries typically focus on interior geometries and exploit analytical tools such as the method of images (Kucera & Blake, 1990; Tagawa & Peters, 2018; Molefe & Peters, 2019) or fully resolve the flow using complicated simulations (Wang *et al.*, 2020). There are also some studies that only investigate the geometry experimentally (Zhang *et al.*, 2017). Harris (1996) presents a simplified numerical model to determine the Kelvin impulse for the treatment of general complex geometries, however the results are not validated. In this research we present and validate a simple numerical model that can be used to treat complex geometries and present results for a complex exterior geometry.

A liquid jet impinging on a boundary can be characterised by its strength and direction. In this paper we investigate the effect of a slot in a flat plate (shown in figure 3.1*a*) on the jet direction. Slot geometries are common and some other geometries in flat surfaces could be modelled as a series of slots. Examples of geometries that could be approximated by slots are scratches in flat surfaces, trenches in semiconductor manufacturing, and various 3D printed objects. These slots could impact how well the surfaces are cleaned or cause concentrations of cavitation damage.

The paper is structured as follows. The problem is defined in section 3.3 and some qualitative predictions are made. The experimental procedure is outlined in section 3.4.1 and the numerical method is defined in section 3.4.2, including some key mathematical derivations. The numerical method is then employed in section 3.5.1 to make some quantitative predictions of the jet direction. Experimental results are presented in section 3.5.2, and subsequently compared to the numerical predictions in section 3.5.3.

3.3 Problem definition

We define a slot as a rectangular channel in a surface, as shown in figure 3.1(*a*). The slot has width W and height H. A bubble is positioned horizontally at a distance X from the slot centre and vertically at a distance Y from the boundary surface. The bubble radius can be neglected when considering only the jet direction, which is discussed further in section 3.4.2.3. The jet direction is measured anticlockwise from the downwards direction such that a positive angle is towards the right side of the slot. These definitions are shown in figure 3.1(*b*). The jet angle is a function of the other four parameters, as defined in equation 3.1. From dimensional analysis, this function can be reduced to a function of the three non-dimensional variables $x = 2X/W$, $y = Y/W$, and $h = H/W$.

The horizontal position of the bubble is normalised with respect to half of the width of the slot so that the bubble is directly above the edge of the slot at $x = 1$. The vertical position of the bubble is normalised with respect to the width as this provides the most versatility. A slot with an infinite height can still be regarded as a slot, whereas a slot with infinite width is no longer a slot. Normalizing with only the width allows the non-dimensional vertical position to retain relevance for all geometries that could be considered as slots. The jet angle, defined in both forms, is thus

$$\theta = f(X, Y, H, W) = g(x, y, h). \tag{3.1}$$

The physical mechanisms affecting the jet direction can be qualitatively understood. When the bubble collapses it draws in fluid from the surroundings. When the bubble collapses in infinite fluid, with no nearby boundaries, the fluid is drawn in completely symmetrically, leading to a spherically symmetrical collapse. If a solid boundary is present, the fluid cannot be drawn directly through the boundary so the boundary is 'impeding' the flow (Blake, 1983). This impedance means that the fluid on the boundary side of the bubble is slower than on the open fluid side. For this reason the bottom of the bubble collapses slower than the top, creating an impulse towards the boundary known as the Kelvin impulse (Blake, 1983). Using this idea of relative impedance, some predictions can be made about how the bubble should behave near the slot. The slot contains fluid, so it should be easier for the bubble to draw fluid from the slot than from a solid boundary, effectively having a lower relative impedance. Thus, the fluid on the slot side of the bubble will move more quickly than on the solid boundary side. This means that the jet should be directed away from the slot. An example of a bubble collapse near a slot is shown in figure 3.2; note how the jet is directed away from the slot. Based on symmetry and limiting behaviour, two more predictions can be made. First, based on symmetry, when the bubble is above the centre of the slot, the jet should be directed straight down ($\theta = 0$). Second, as the bubble moves infinitely far from the slot ($x \to \infty$) the boundary becomes a simple flat boundary and the jet must also be directed straight down. Based on these predictions, it is expected that there will be some maximum θ between $x = 0$ and $x \to \infty$ with a negative minimum of an equal magnitude on the opposite side of the slot.

3.4 Methods

3.4.1 Experimental method

Experiments were conducted using laser-induced cavitation (Lauterborn, 1972; Noack & Vogel, 1999) with the microscope objective method described in section 2.1.1. Slot geometries for a range of slot widths and heights were created by layering laser cut

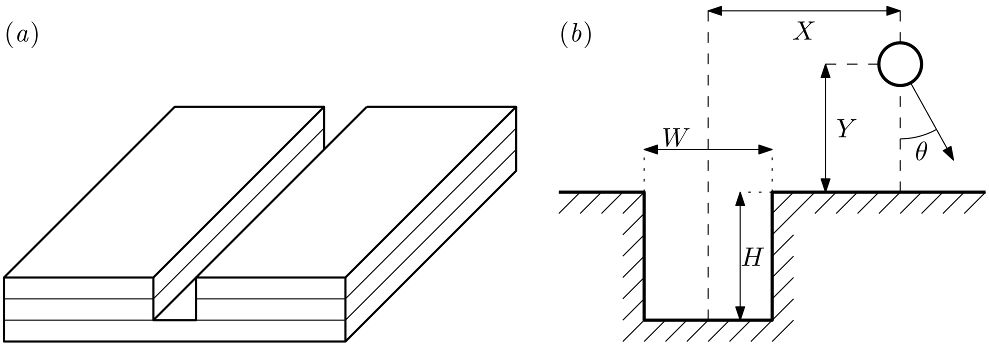

FIGURE 3.1: (*a*) Schematic view of a slot in the surface of a flat boundary constructed from layered acrylic. (*b*) The parameters defining a slot, bubble position, and jet direction.

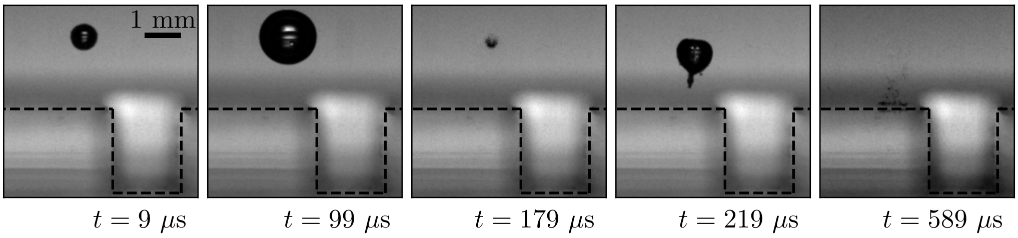

FIGURE 3.2: Snapshots from a high-speed recording of a bubble collapse near a slot with width $W = 2.2$ mm and $H = 2.7$ mm with the bubble positioned at a vertical distance $Y = 2.29$ mm and horizontal distance $X = -2.03$ mm. The jet angle is measured to be $\theta = -0.099$ radians (-5.7 degrees). The slot outline is indicated by the black dashed line.

acrylic, as shown in figure 3.1(*a*). The plates were 50 mm wide and the slots extended 50 mm along the plate. Bubbles ranged in diameter from approximately 1 mm to 3 mm. Around the jet angle peaks the bubbles were at least 10 bubble radii away from the plate edges. The relatively large distances to the tank walls, plate edges, and plate holder meant that their effects on the jet angle were negligible. Bubbles were at most 16 bubble radii away from the slot centre horizontally, and ranged between 1.25 and 8.6 bubble radii from the slot surface vertically. Figure 3.2 shows snapshots from one recording of a bubble collapsing near a slot.

As described in section 2.3, recordings were post-processed in Python to measure key characteristics such as the bubble size variation over time and the direction of the resulting jet. To determine the jet direction, a vector was taken between the centroid positions of the first and second maxima of the bubble size (at 99 μs and 219 μs in figure 3.2) which is generally a good approximation of the nominal jet direction at a position and is straightforward to measure (Tagawa & Peters, 2018). From this analysis, and position measurements from the translation stage, graphs were produced characterising how the jet direction varied with bubble position and geometry characteristics.

3.4.2 Numerical method

The collapse of a gas or vapour bubble occurs on a timescale where viscous effects are not significant and the water can be considered incompressible for the majority of the collapse. This means that the collapse can be modelled by a velocity potential ϕ. Various methods have been used to solve for this velocity potential. Simple potential flow models using mirror sinks have been used to predict the jet direction in limited geometries (Kucera & Blake, 1990; Tagawa & Peters, 2018; Molefe & Peters, 2019). More complex boundary integral methods and boundary element methods have been applied, typically to simulate how the surface of the bubble moves during collapse (Kucera & Blake, 1990; Harris, 1996; Li *et al.*, 2016; Brujan *et al.*, 2019). In this research a simplified boundary element method is used to predict the jet direction without resolving how the surface of the bubble moves over time. This is similar to the mirror sink model employed by Tagawa & Peters (2018) and Molefe & Peters (2019) to compute jet direction but with an infinite distribution of 'mirror' sinks along the geometry boundary as in boundary element methods. This method combines the simplicity of the mirror sink model for finding the jet direction with the geometric versatility of boundary element methods. Using a simple model keeps the computational cost low, allowing for analysis of many different geometries across large parameter spaces. The method employed in this research is similar in form to that used by Harris (1996) but without solving for the bubble variation with time. Three key derivations are included here for completeness: the numerical method used, the derivation of the effect of a panel on itself, and the derivation of average bubble surface velocity for considering the effect of bubble size. Validation of the numerical model is also demonstrated in this section.

3.4.2.1 Boundary element method

The boundary is modelled as an infinite distribution of sinks on the boundary surface with varying strength. The infinite distribution of sinks is divided into panels such that the strength of the sinks within a panel can be approximated by a constant strength across the whole panel. The strength of each panel is determined by asserting no flow through the boundary surface at the centre of every panel and solving the resulting system of linear equations. The derivation for these equations is shown here.

A sink at position $\mathbf{x}_s$ induces a velocity $\nabla\phi = \mathbf{u}$ at any position $\mathbf{x} \neq \mathbf{x}_s$

$$\mathbf{u} = \frac{m(\mathbf{x} - \mathbf{x}_s)}{4\pi|\mathbf{x} - \mathbf{x}_s|^3}, \tag{3.2}$$

where m is the volume flow rate of the sink, typically referred to as the sink strength.

The flow through a surface with normal vector **n** is the scalar product of the velocity at that point, **u**, with the normal vector:

$$\frac{\partial \phi}{\partial n} = \frac{\partial \phi}{\partial x} n_x + \frac{\partial \phi}{\partial y} n_y + \frac{\partial \phi}{\partial z} n_z = \mathbf{u} \cdot \mathbf{n}. \tag{3.3}$$

The velocity through the wall is a combination of the normal velocity from the bubble, $\partial \phi_b / \partial n$, and the normal velocity from the wall, $\partial \phi_w / \partial n$, which must sum to zero for the no-through-flow condition to be met:

$$\frac{\partial \phi}{\partial n} = \frac{\partial \phi_b}{\partial n} + \frac{\partial \phi_w}{\partial n} = 0. \tag{3.4}$$

Thus, the normal component of the velocity from the wall can be expressed as the negative of the normal component of the velocity potential from the bubble.

$$\frac{\partial \phi_w}{\partial n} = -\frac{\partial \phi_b}{\partial n} \tag{3.5}$$

To determine the normal velocity from the bubble at a position **x**, the results from equations 3.2 and 3.3 can be combined to give

$$\frac{\partial \phi_b}{\partial n} = \mathbf{u}_b \cdot \mathbf{n} = \frac{m_b (\mathbf{x} - \mathbf{x}_b)}{4\pi |\mathbf{x} - \mathbf{x}_b|^3} \cdot \mathbf{n}, \tag{3.6}$$

where $\mathbf{x}_b$ is the position of the bubble.

Similarly, the velocity contribution from the wall can be expressed with the integral of the boundary sink strength density σ over the wall surface W.

$$\frac{\partial \phi_w}{\partial n} = \iint_W \sigma(\mathbf{x}_w) \frac{\mathbf{x} - \mathbf{x}_w}{4\pi |\mathbf{x} - \mathbf{x}_w|^3} \cdot \mathbf{n} \mathrm{d}W, \tag{3.7}$$

where $\mathbf{x}_w$ is a position on the wall surface.

The wall surface is expressed as a series of N panels, each with a constant sink strength density, σ_j, centroid position, $\mathbf{x}_j$, and an area, A_j. Thus, equation 3.7 is approximated by

$$\frac{\partial \phi_w}{\partial n} = \sum_{j=1}^{N} \sigma_j \frac{A_j (\mathbf{x} - \mathbf{x}_j) \cdot \mathbf{n}}{4\pi |\mathbf{x} - \mathbf{x}_j|^3}. \tag{3.8}$$

Substituting equations 3.6 and 3.8 into 3.5 yields

$$\sum_{j=1}^{N} \sigma_j \frac{A_j (\mathbf{x} - \mathbf{x}_j) \cdot \mathbf{n}}{4\pi |\mathbf{x} - \mathbf{x}_j|^3} = -m_b \frac{(\mathbf{x} - \mathbf{x}_b) \cdot \mathbf{n}}{4\pi |\mathbf{x} - \mathbf{x}_b|^3}. \tag{3.9}$$

This can be rewritten in terms of factors relating to the relative positions of each point. In this research, R denotes these factors such that

$$R_j = \frac{A_j(\mathbf{x} - \mathbf{x}_j) \cdot \mathbf{n}}{4\pi|\mathbf{x} - \mathbf{x}_j|^3}, \tag{3.10}$$

$$R_b = \frac{(\mathbf{x} - \mathbf{x}_b) \cdot \mathbf{n}}{4\pi|\mathbf{x} - \mathbf{x}_b|^3}, \tag{3.11}$$

and

$$\sum_{j=1}^{N} R_j \sigma_j = -m_b R_b. \tag{3.12}$$

In order to calculate the sink strength densities, σ_j, equation 3.12 must be solved at a number of points on the boundary equal to the number of panels. For a reasonable distribution of points, and convenience, these points are selected to be the panel centroids. Defining R_{12} as the effect of the second panel at the centroid of the first panel, and so on, we write

$$\begin{bmatrix} R_{11} \; R_{12} \ldots R_{1N} \\ R_{21} \; R_{22} \ldots R_{2N} \\ \vdots \quad \vdots \quad \ddots \quad \vdots \\ R_{N1} R_{N2} \ldots R_{NN} \end{bmatrix} \sigma = -m_b \begin{bmatrix} R_{b1} \\ R_{b2} \\ \vdots \\ R_{bN} \end{bmatrix}, \tag{3.13}$$

$$R\sigma = -m_b \mathbf{R}_b, \tag{3.14}$$

where each term of the R matrix is

$$R_{ij} = \frac{A_j(\mathbf{x}_i - \mathbf{x}_j) \cdot \mathbf{n}_i}{4\pi|\mathbf{x}_i - \mathbf{x}_j|^3}, \tag{3.15}$$

which is undefined for any value $i = j$. This is resolved in section 3.4.2.2.

As with any system of linear equations, the system in equation 3.14 could be solved in many ways. However, it is noted that the R matrix is fixed for any given geometry and is entirely independent of bubble position. Thus, if multiple bubble positions need to be evaluated for a single boundary geometry, a single inversion of the R matrix can be used to solve the system for all bubble positions using

$$\sigma = -m_b R^{-1} \mathbf{R}_b. \tag{3.16}$$

Although other methods would be faster for solving the system for a single position, this method is far more efficient when multiple bubble positions need to be solved.

This method generally performs well, as will be demonstrated in later sections, but is vulnerable to ill-conditioned systems in some cases. However, such systems can be identified using the condition number of the R matrix and avoided.

3.4.2.2 Panel integral

The normal velocity induced by a panel at its own centroid is required in order to solve equation 3.13. For the majority of the panel this poses no issue; the velocity induced by a point that is not at the centroid is entirely tangential to the panel and so does not contribute to the normal velocity. However, the velocity induced by the centroid itself is undefined. Following the example of Brebbia & Dominguez (2001), the singularity can be resolved.

The panel is deformed such that the centroid is expanded into a hemisphere with radius ϵ, as shown in figure 3.3. The velocity normal to the panel at the centroid becomes the integral of the normal velocity induced by the sink at the centroid position over the whole hemisphere.

For any point on the hemisphere, the velocity induced by the centroid sink is always normal to the surface. The normal velocity at any such point is thus

$$\mathbf{u} \cdot \mathbf{n} = \frac{\sigma}{4\pi\epsilon^2}. \tag{3.17}$$

For a circle on the hemisphere aligned parallel to the panel, with all points at an angle φ from the horizontal, the sum of velocities is

$$u_{circle} = \frac{\sigma}{4\pi\epsilon^2} 2\pi\epsilon \cos(\varphi) = \frac{\sigma}{2\epsilon} \cos(\varphi). \tag{3.18}$$

This is integrated over the whole hemisphere to give

$$u_{total} = \int_0^{\pi/2} \frac{\sigma}{2\epsilon} \cos(\varphi) \epsilon \mathrm{d}\varphi = \frac{\sigma}{2} \int_0^{\pi/2} \cos(\varphi) \mathrm{d}\varphi = \frac{\sigma}{2}, \tag{3.19}$$

which is independent of the hemisphere radius, ϵ. As $\epsilon \to 0$, the velocity induced by the panel at its own centroid is a constant $\sigma/2$ and so the relative position factor is $R = 0.5$.

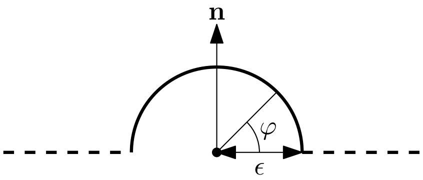

FIGURE 3.3: A cross-section of a panel (dashed line) deformed such that the centroid is a hemisphere (solid line), with radius ϵ, centred on the panel centroid.

3.4.2.3 Average surface velocity

Previous research (Tagawa & Peters, 2018; Molefe & Peters, 2019) has shown that the jet direction is accurately predicted by the velocity that the mirror sinks induce at the position of the bubble centroid.

The jet direction is aligned with the bubble translation velocity which is defined as the velocity of the centroid. We define the centroid as the average position of the bubble surface, so the velocity of the centroid is the average velocity of the bubble surface. In this section, it is shown that the induced velocity at the centroid of a spherical bubble is equal to the average velocity of the bubble surface, independent of bubble size.

The velocity induced by any individual sink on a point is given by

$$\mathbf{u} = -\frac{m\mathbf{r}}{4\pi|\mathbf{r}|^3}, \tag{3.20}$$

where $\mathbf{r}$ is the vector from the sink to the point.

By integrating $\mathbf{u}$ over a sphere it can be shown that the total velocity on the surface of the sphere is

$$\mathbf{u}_{total} = -m\frac{\mathcal{R}^2\mathbf{d}}{|\mathbf{d}|^3}, \tag{3.21}$$

where $\mathcal{R}$ is the radius of the sphere and $\mathbf{d}$ is the vector from the sink to the bubble centroid.

The average velocity on the surface of the sphere is thus the total velocity divided by the surface area of the sphere,

$$\mathbf{u}_{avg} = \frac{\mathbf{u}_{total}}{4\pi\mathcal{R}^2} = -\frac{m\mathcal{R}^2\mathbf{d}}{4\pi\mathcal{R}^2|\mathbf{d}|^3} = -\frac{m\mathbf{d}}{4\pi|\mathbf{d}|^3}, \tag{3.22}$$

which is equal to the velocity induced by the sink at the bubble centroid.

Due to the properties of potential flow, the velocity induced by every sink is simply a linear summation of the velocity induced by each individual sink. Thus, the average surface velocity of a sphere induced by a combination of sinks is equal to the velocity at the centre of the sphere. It is noted that the bubble sink itself does not contribute to the average surface velocity as all components cancel out.

3.4.2.4 Verification

Verification, as well as initial validation, of the boundary element method presented here was performed by comparison to the analytical model presented in Tagawa & Peters (2018). Figure 3.5 shows a schematic of a $\theta_c = \pi/2$ corner with uniform length and equal depth. This geometry, and similar models with varying corner angles, were generated using the BEM and then compared to the method of images model presented in Tagawa & Peters (2018). Figure 3.4 shows comparisons between the BEM (labelled 'Numeric') and method of images (labelled 'Analytic'). The comparisons to the analytic solution are broadly good, especially so for a corner angle of $\pi/2$. However, the quality of the solution does vary with the corner angle. Notably, the $\pi/4$ corner has particularly poor agreement. For each corner BEM model, the infinity norm condition number, $||R||_\infty$, is shown. A high condition number indicates that the solution to the system of equations is very sensitive to small changes in the input. For the comparisons here, when the condition number is very high the solution is notably poor. This indicates that this BEM model is vulnerable to ill-conditioned systems, but that these systems can be detected and avoided.

Figure 3.6 shows the root mean squared difference (RMSD) between the BEM model solution and the method of images solution. This is calculated by numerically integrating the square of the analytical solution subtracted from the numerical solution in the range $\theta_c/4 \leq \theta_b \leq 3\theta_c/4$. This limits the effect of near-panel interactions. The mean square difference is obtained by dividing the integral by $\theta_c/2$ and then the square root is taken to obtain the RMSD.

For figure 3.6, the bubble was positioned at a distance 5 from the center of the corner and panel sizes were selected such that, as the bubble approached the plates, it would align with the center of a panel. This ensured consistent results as the position of the bubble relative to the panels when approaching the boundaries can slightly vary the solution. The analytic solution is equivalent to a panel size of zero and an infinite plate length, $L \to \infty$. As the panel size tends to zero, the RMSD tends to a limiting value and as the plate length increases, this limiting value decreases. This indicates that the BEM model converges to a stable solution, and that the stable solution is accurate.

3.5 Results and discussion

3.5.1 Numerical results

Using the boundary element method described in section 3.4.2, the jet direction can be modelled for given geometric parameters. Up to 20 000 panels were used to model the boundary, with a distribution such that there were more panels near the slot than towards the edges of the plate. The Python implementation of the boundary element method developed for this research runs on a standard desktop computer, where the primary limitation is the memory required to store the matrices.

Figure 3.7 shows a contour plot of the jet angle for a slot with a square cross-section ($h = 1$). As predicted qualitatively, the jet is directed towards the boundary but angled away from the slot. Three main regimes are revealed. Close to the boundary but far from the slot (low y, high x) the jet angle is dominated by the flat boundary and is not significantly affected by the slot. This leads to a very low jet angle. Near the centre of the slot the geometric symmetry dominates, again leading to low jet angles. The third regime is between these two, where the bubble is far enough from the centre that

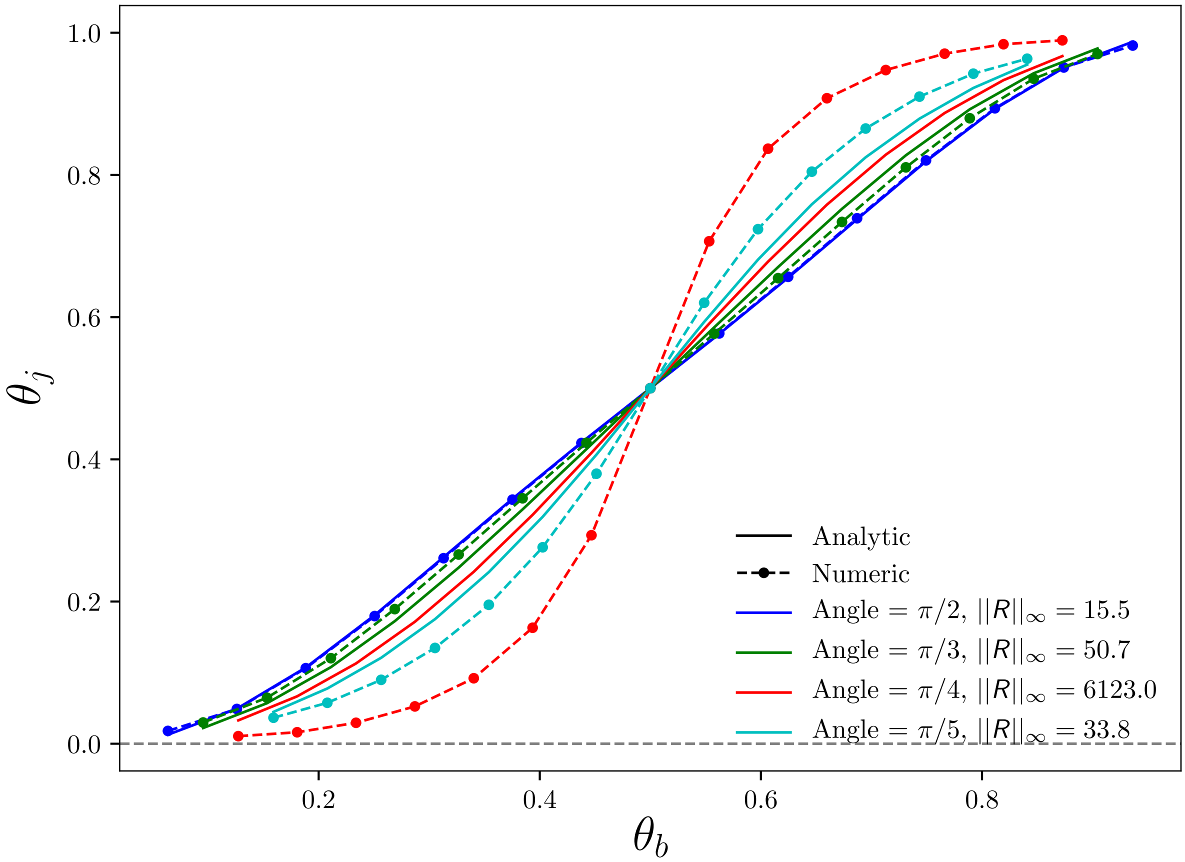

FIGURE 3.4: Comparisons between analytic and BEM solutions for a series of corners. Dashed lines are numerical model results using the BEM. Solid lines are analytical results using the method of images.

symmetry does not dominate, and positioned such that the slot has a significant effect relative to the flat boundary.

In order to more easily quantify this shape, and for simpler comparison to experimental results, slices of the θ contour are taken with constant y and a range of x. One such slice is shown in figure 3.7(*b*) and is the form in which data will be presented hereafter. As in the contour plot, this plot shows that the jet tends to be directed straight at the boundary when the bubble is far from the slot. As the bubble approaches the slot the jet is angled away from the slot centre down to a negative peak jet angle. After the peak the jet angle tends back towards zero, crossing zero at the centre point. The jet angle then increases to an equal and opposite peak on the other side of the slot due to the symmetry of the geometry.

Using the normalised geometric parameters, two sets of numerical predictions have been plotted in figures 3.8 and 3.9 to show how the jet angle curve varies with h and y.

Figure 3.8(*a*) shows that the peak jet angle increases as the normalised slot height, h, increases. This is because the slot contains more fluid and so its relative impedance is

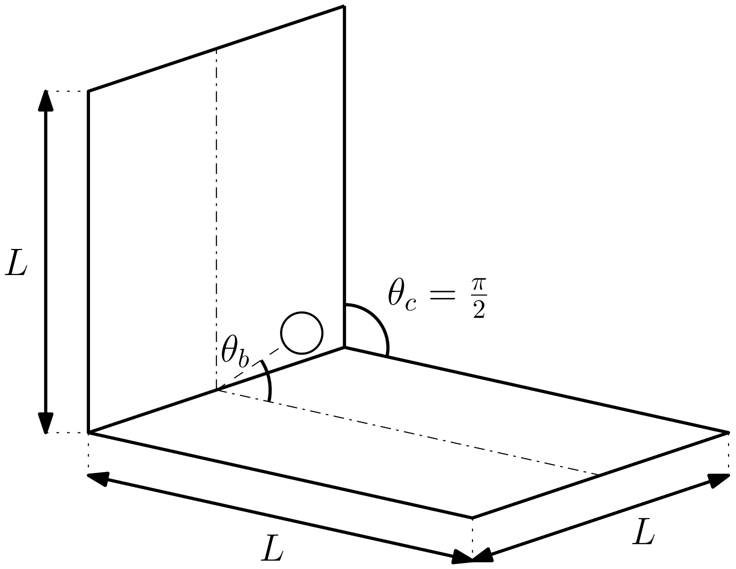

FIGURE 3.5: Schematic of the corner geometry used for verification.

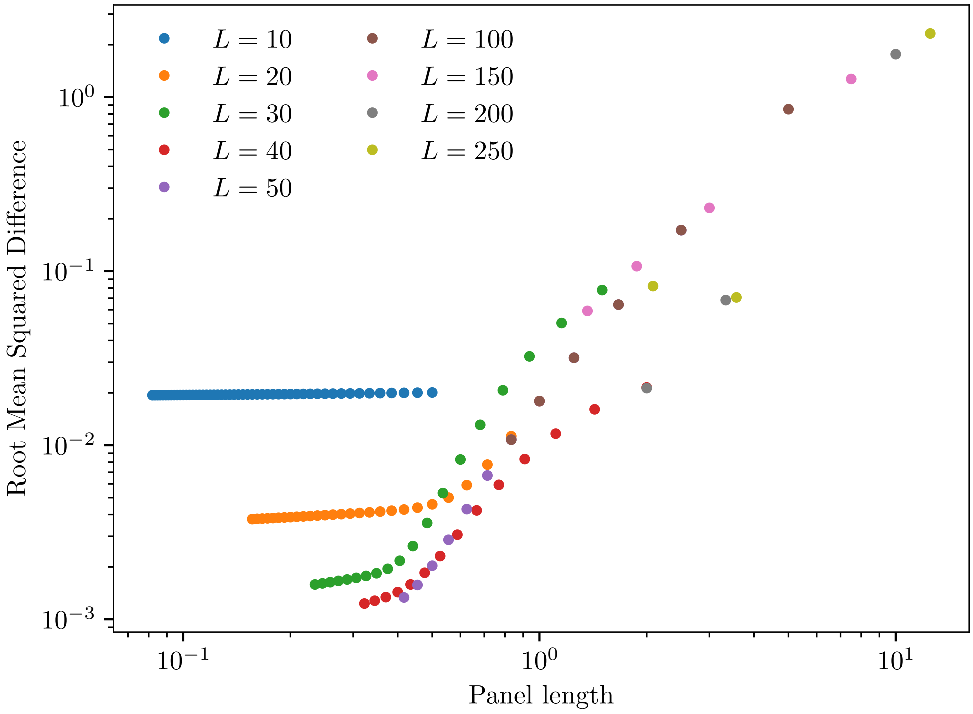

FIGURE 3.6: Convergence plot for the $\pi/2$ corner geometry for decreasing BEM panel length and increasing corner plate length.

decreased. The position of the peak moves closer to the slot as the height is increased. These curves have a similar shape, which can be characterised by two parameters defining the peak. For a given y and h, the maximum value of θ is $\theta^\star$ and occurs at $x = x^\star$. Thus, θ can be normalised with $\theta^\star$, and x can be normalised with $x^\star$.

$$\hat{\theta} = \frac{\theta}{\theta^\star}, \hat{x} = \frac{x}{x^\star} \tag{3.23}$$

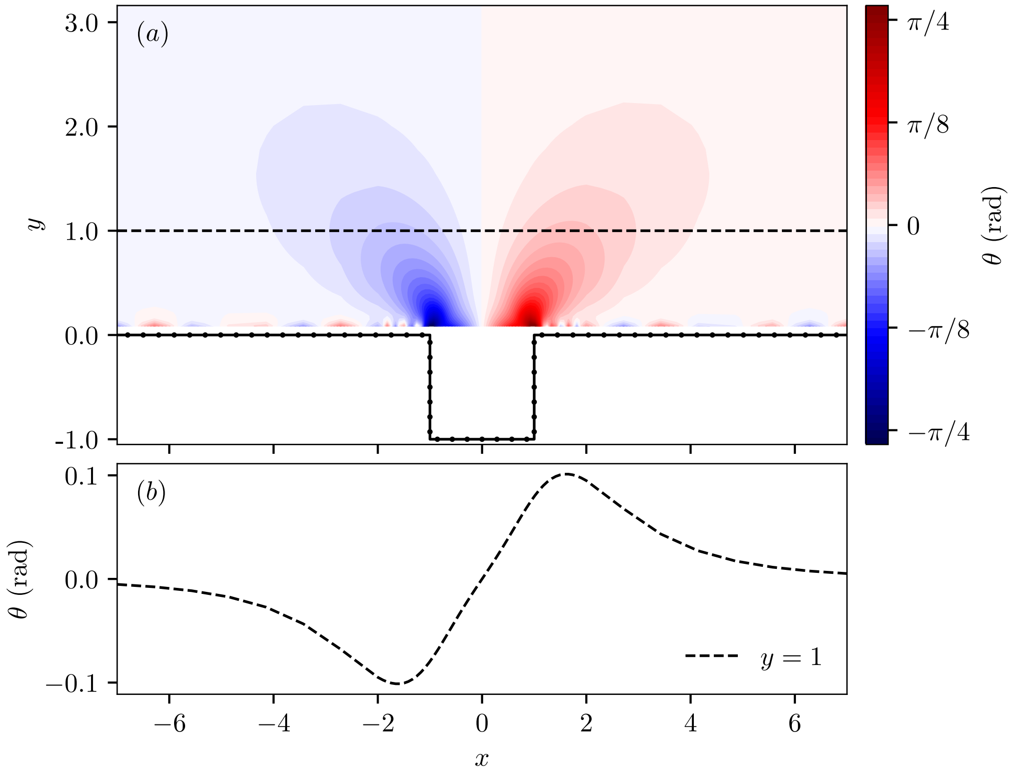

FIGURE 3.7: (*a*) A contour plot of θ as a function of x and y. The slot, with $h = 1$, is represented by the black line, with points plotted at the panel centroids. Very close to the boundary the jet angle is more strongly affected by individual panel sinks rather than the boundary as a whole leading to the more rapid variations visible near the boundary. (*b*) A plot of θ against x for $y = 1$, corresponding to the black dashed line on the contour plot in (*a*).

When these curves are normalised, as shown in figure 3.8(*b*), they collapse down to being very close to the same curve, with the exception of the data with the lowest height ($h = 0.5$).

Figure 3.9(*a*) shows that the peak jet angle, $\theta^\star$, increases as the normalised vertical distance away, y, decreases. This is because the bubble is closer to the boundary and so is more strongly affected. The position of the peak, $x^\star$, moves further from the slot as the vertical distance away is increased. When these curves are normalised, as shown in figure 3.9(*b*), they also collapse down to being very close to the same curve, with the exception of the data closest to the boundary ($y = 0.5$).

It is noted that the $h = 1$ curves in figure 3.8 are the same as the $y = 1$ curves in figure 3.9 showing that the curves from both figures collapse to the same curve.

As mentioned, the curves collapse except for bubbles very close to the boundary, or with slots that have a low height. For these cases, the effect of the slot can be treated as two opposing steps with a relatively large separation. A single step would cause a single jet angle peak. When the effects of two peaks with opposite signs are combined, the gradient in the middle depends on the separation of the peaks. If the peaks are very close, then the peaks blend together resulting in the collapsed shapes seen in figures 3.8(*b*) and 3.9(*b*). If, however, the peaks are far apart then a pronounced kink in the curve appears at the middle of the slot, as shown by the $h = 0.5$ curve in figure 3.8 and the $y = 0.5$ curve in figure 3.9. When bubbles are close to the boundary the effects of each side of the slot are relatively more separated, as is also the case for low height slots. Most slots have $h \geq 1$ and $y \geq 1$ where the peaks merge giving the collapsed curve shape; only these curves will be considered in further analysis.

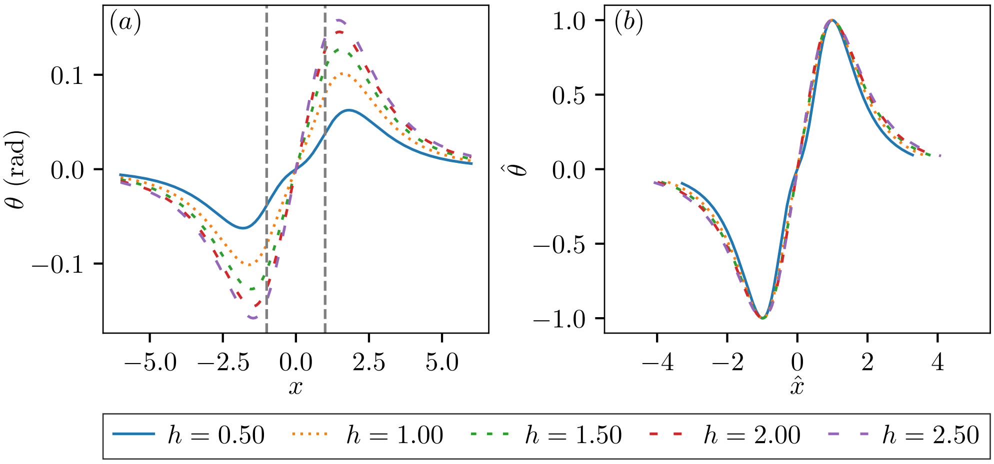

FIGURE 3.8: (*a*) θ against x for a range of slot geometries characterised by h and a fixed value of $y = 1$. The slot boundaries are indicated by the dashed vertical lines ($x = -1$, $x = 1$). (*b*) Normalised θ, $\hat{\theta}$, against normalised x, $\hat{x}$, for the same values of h. The curves collapse well onto one curve when normalised. The $h = 1$ curves here are the same as the $y = 1$ curves in figure 3.9.

As the curves in figures 3.8 and 3.9 collapse well onto the same curve, $\theta^\star$ and $x^\star$ can be used to characterise the variation of the jet angle with the parameters h and y. Two contour plots in figure 3.10 show $\theta^\star$ and $x^\star$ plotted as functions of h and y.

Figure 3.10(*a*) shows that the maximum jet angle, $\theta^\star$, depends most strongly on the dimensionless vertical bubble position, y. As y increases, with the bubble moving far from the slot, the maximum jet angle tends towards zero. As y tends towards zero, the maximum jet angle increases very rapidly, but is bounded by the solution for a convex right-angle corner as would be the case for a bubble at $y = 0$ as $x \to 1^-$.

Figure 3.10(*a*) shows a weaker dependence of maximum jet angle on the dimensionless slot height, h, compared to the dependence on y. As h increases, the maximum jet angle tends towards a limit, as can be observed in the contour, showing only a dependence on y for large values of h. The figure also shows that the maximum jet angle tends to zero as h tends to zero which is expected as the slot becomes a flat plate.

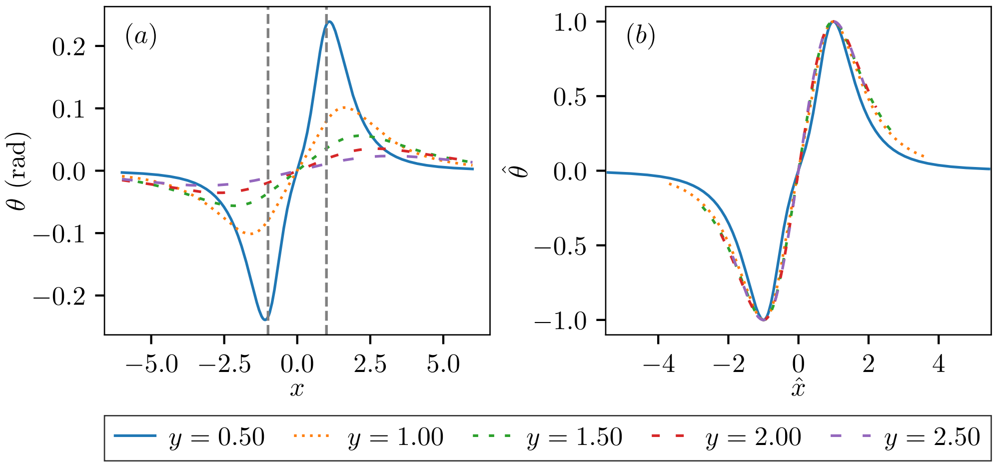

FIGURE 3.9: (*a*) θ against x for a range of slot geometries characterised by y and a fixed value of $h = 1$. The slot boundaries are indicated by the dashed vertical lines ($x = -1$, $x = 1$). (*b*) Normalised θ, $\hat{\theta}$, against normalised x, $\hat{x}$, for the same values of y. The curves collapse well onto one curve when normalised. The $y = 1$ curves here are the same as the $h = 1$ curves in figure 3.8.

Figure 3.10(*b*) shows the dependence of the position of the maximum jet angle, $x^\star$, on both y and h. $x^\star$ increases approximately linearly with y, as might be predicted from figure 3.7(*a*). For low values of h the gradient of the linear relationship changes, but as h increases the gradient tends towards 1 (this can be seen in figure 3.15(*b*) where the gradient of the $x^\star$-y line is approximately 1). It is noted that, for very low jet angles, the position of the peak becomes more sensitive to numerical errors and imperfect boundary conditions, such as the edges of the plate. Very low jet angles are found at low h and high y values, in the top left corners of the contour plots in figure 3.10.

Both $\theta^\star$ and $x^\star$ exhibit limiting behaviour as h increases. This suggests that at some point increasing the height of the slot will have a negligible effect on the jet angle. Even for lower values of h, the variation with h is typically much less significant than with y.

3.5.2 Experimental results

Experiments were conducted by performing a horizontal sweep over a selected slot at fixed vertical distances Y. The horizontal positions tested were selected to focus most of the data around both θ peaks and to observe the behaviour at a large horizontal distance on at least one side of the slot. Each position was tested multiple times; for most experiments there were five repeats.

In order to understand the stochastic variation of θ that occurs at each position, two series of experiments were conducted with 50 repeats at each position. From this data it was observed that the standard deviation of jet angle is reasonably consistent for all positions and conforms well to the normal distribution. We did not observe a dependence

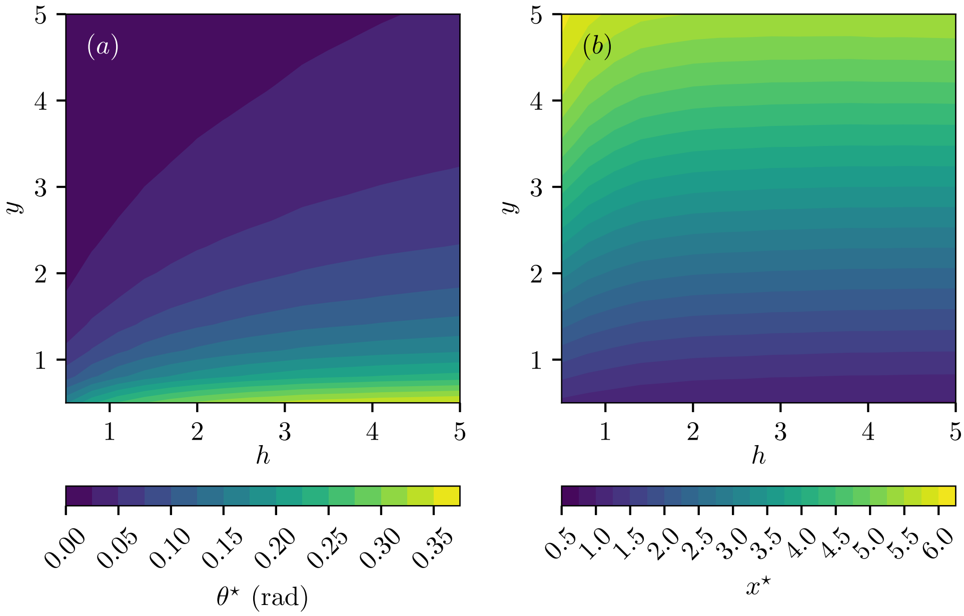

FIGURE 3.10: Contour plots of peak jet angle, $\theta^\star$, and peak jet angle position, $x^\star$, as functions of non-dimensional vertical distance, y, and non-dimensional slot height, h.

of jet angle variation on the magnitude of the bubble displacement. This standard deviation was therefore applied to the remainder of the data to provide statistical error bars that show a 99% confidence interval of the mean at each position based on the number of repeats at those positions.

A second order polynomial curve fit was applied around each of the two peaks of the θ-x curve. As the geometry is symmetrical the two peaks should be equal and opposite; the peak on the negative x side should have a negative θ value of the same magnitude as on the positive x side. Thus, if the polynomial curve fits on each side are slightly offset from being symmetrical, all of the data can be shifted by the offset in both θ and x to achieve symmetry. Offsets in θ are most likely caused by misalignments in the experiment. Other possible sources of asymmetry would cause offsets of much lower magnitudes than even minor misalignments. In addition to correcting for misalignments, low quality data can be identified by very large curve fit offsets. The curve fit from one side, mirrored in both axes, should fit the data from the opposite side. If this is not the case then it can be concluded that the data is of a low quality and thus neglect it from further analysis. Of the data collected in this research, horizontal sweeps at three y values for the W2H6 geometry were neglected on this basis and thus not presented here.

Data was gathered for both peaks so that this symmetry analysis could be conducted. However, only one side of the slot was tested to a greater horizontal distance as the behaviour in this region is already well understood. An example sweep with the curve

Label	W (mm)	H (mm)	Y values measured (mm)	h	y
W1H3	1.23	2.74	1.94, 2.91, 3.89	2.23	1.58, 2.37, 3.16
W2H3a	2.20	2.70	1.77, 2.29, 2.81, 3.32, 3.84	1.23	0.80, 1.04, 1.28, 1.51, 1.75
W2H3b	2.20	2.90	2.66, 3.68	1.32	1.21, 1.67
W2H6	2.20	5.40	1.52, 1.99	2.45	0.69, 0.90
W2H9	2.14	8.21	1.66, 2.66	3.84	0.78, 1.24
W2H12	2.20	11.50	2.63	5.23	1.20
W4H12	4.20	11.47	2.43, 3.43	2.73	0.58, 0.82

TABLE 3.1: Measurements of geometries used. Labels refer to the nominal width and height.

fit plotted is shown in figure 3.11. In this example the peaks are slightly offset from being symmetrical, so the data would be shifted before conducting further analysis.

The geometries tested are shown in table 3.1 and the jet angle data is summarised in figure 3.12. The experimental results follow the same qualitative trends as the numerical predictions. There is a negative jet angle peak on the left side of the slot, and a positive jet angle peak on the right. The magnitude of jet angle peak increases as y decreases and h increases. The position of the jet angle peak increases as y increases, but it is more difficult to discern how the position varies with h.

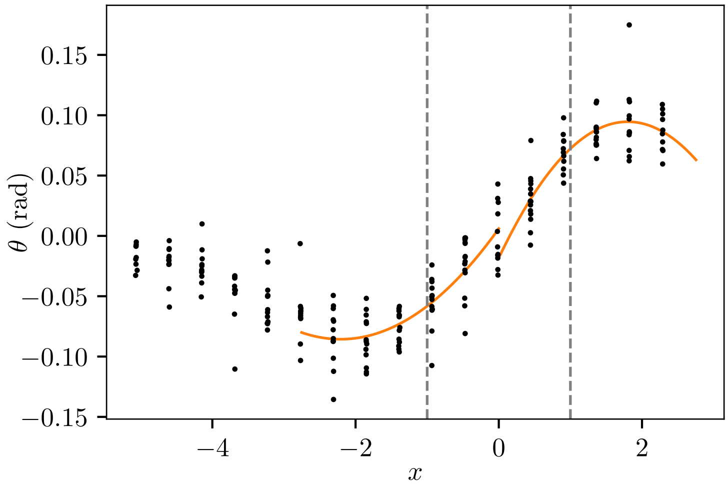

FIGURE 3.11: An example curve fit on data using slot 'W2H3a' from table 3.1 ($W = 2.2$ mm, $H = 2.7$ mm). The bubble was positioned at a vertical distance $Y = 2.81$ mm. The points are the experimental data and the lines are the two curve fits. The slot boundaries are indicated by the dashed vertical lines ($x = -1$, $x = 1$).

3.5.3 Comparison

We will now proceed to directly compare our experimental data to the numerical results.

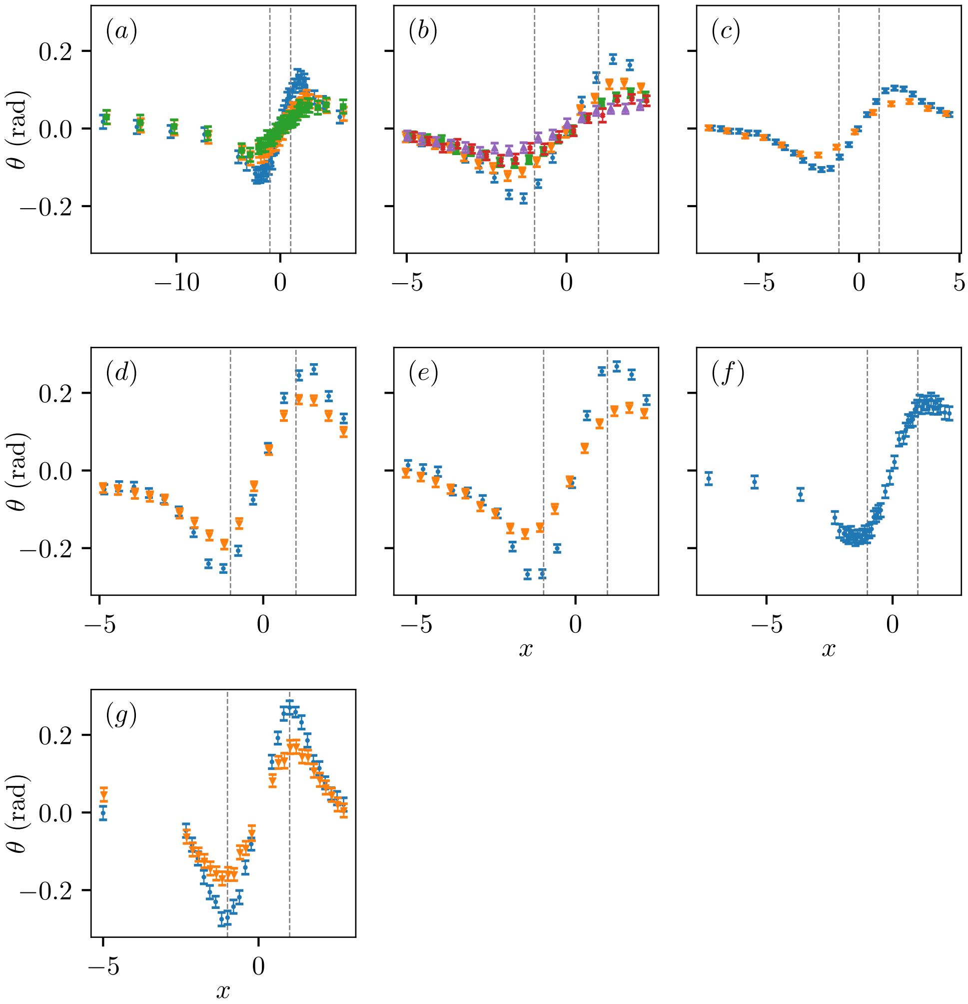

FIGURE 3.12: θ plotted against x for all experimental data from table 3.1. The slot boundaries are indicated by the dashed vertical lines ($x = -1$, $x = 1$). Data is coloured by y value; peak θ decreases as y increases. (*a*) W1H3: blue $y = 1.58$, orange $y = 2.37$, green $y = 3.16$. (*b*) W2H3a: blue $y = 0.80$, orange $y = 1.04$, green $y = 1.28$, red $y = 1.51$, purple $y = 1.75$. (*c*) W2H3b: blue $y = 1.21$, orange $y = 1.67$. (*d*) W2H6: blue $y = 0.69$, orange $y = 0.90$. (*e*) W2H9: blue $y = 0.78$, orange $y = 1.24$. (*f*) W2H12: blue $y = 1.20$. (*g*) W4H12: blue $y = 0.58$, orange $y = 0.82$.

Figure 3.13 shows a direct comparison between four experimental data curves and boundary element method predictions for the same geometric parameters. These plots show a good agreement between predicted curves and experimental results. The most significant difference is for the W4H12 geometry where the experimental data has a steeper gradient on the outer sides of the peaks, but the magnitude and position of the peak is well predicted. It is noted that the W4H12 data in general has a steeper peak curve than other experimental data when compared to numerical results. There is a tendency for the numerical model to under-predict the magnitude of the jet angle peak, although the peak position is generally predicted well. On average, across all 17 horizontal sweeps presented here, the numerical model under-predicted $\theta^{\star}$ by 13 %

and $x^\star$ by 2.6 %.

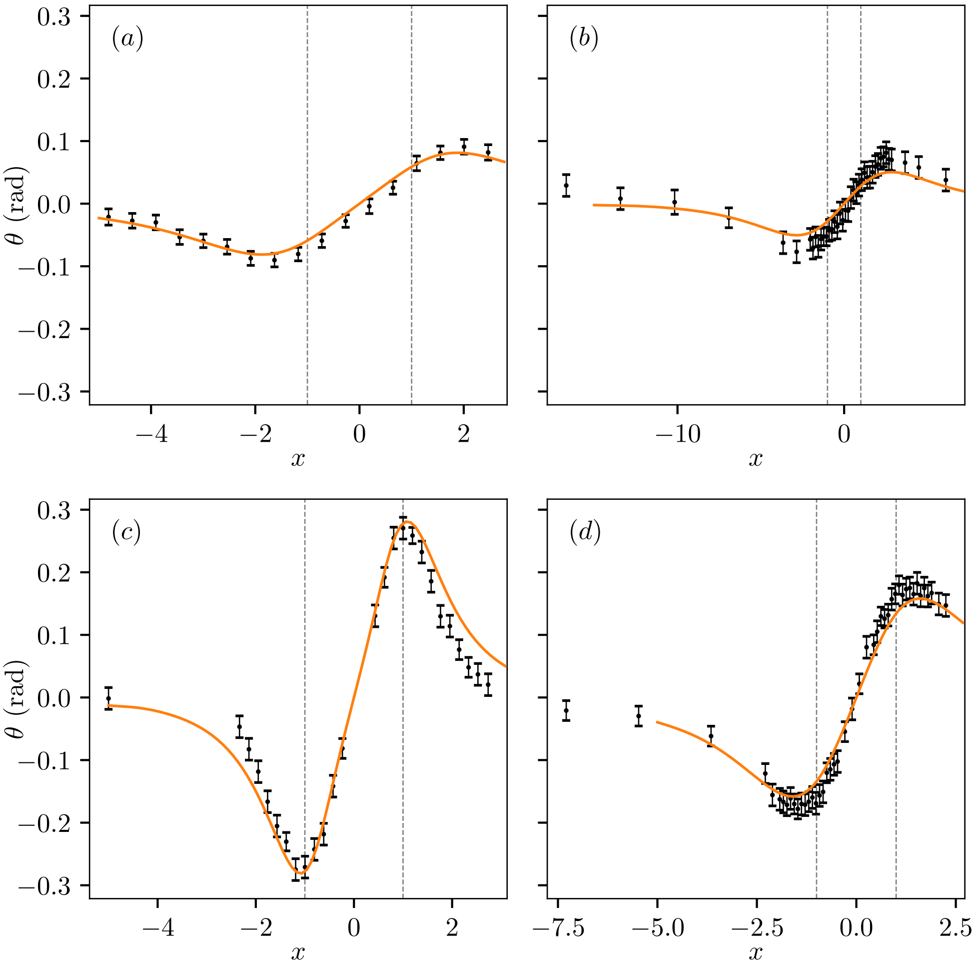

FIGURE 3.13: Experimental data for a series of slots from table 3.1. This data is compared to numerical predictions for the same configurations. Experimental data is plotted as points with error bars, numerical model predictions are plotted as solid lines. The slot boundaries are indicated by the dashed vertical lines ($x = -1$, $x = 1$). Geometries are ordered by h value. (*a*) W2H3a, $h = 1.23$, $y = 1.28$. (*b*) W1H3, $h = 2.23$, $y = 2.37$. (*c*) W4H12, $h = 2.73$, $y = 0.58$. (*d*) W2H12, $h = 5.23$, $y = 1.20$.

All experimental data collapses onto a single curve when the experimental data is normalised with the peak values $x^\star$ and $\theta^\star$, which were determined using the previously described curve fitting method. Figure 3.14 shows all of the data normalised and compared to the normalised prediction curve that matches all predictions with $h \geq 1$ and $y \geq 1$. The experimental data collapses very well, validating the collapse observed from the numerical predictions. Although the numerical prediction curve has a slightly higher normalised jet angle on the outer sides of the peaks, the collapsed experimental data curve matches the numerical curve remarkably well. The variations in the normalised curve observed numerically at very low h and at very low y would likely not be visible in the experimental data due to the magnitude of the error compared to the magnitude of the variations.

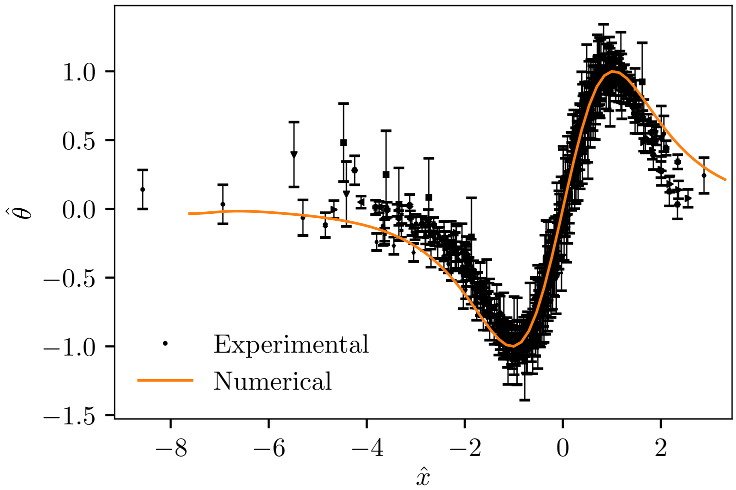

FIGURE 3.14: Experimental results from all geometries, each with a range of y, showing normalised jet angle, $\hat{\theta}$, against normalised horizontal position, $\hat{x}$. This is compared to the collapsed numerical curve that matches all numerical curves for $y \geq 1$ and $h \geq 1$. The experimental results collapse down onto one curve and match the numerical prediction.

A comparison between numerically predicted $\theta^\star$ and $x^\star$ trends and experimental results is shown in figure 3.15. Here $\theta^\star$ and $x^\star$ have been calculated using the curve fitting method described in section 3.5.2. The error bars in this figure are based on the error distribution from large amounts of data, synthesised using the numerical model, with similar properties to experimental data. It is also noted from the synthesised data that the curve fit has a tendency to over-estimate the peak position. The results are compared for the same h values as the experimental data and the same range of y values as figure 3.10. These results generally show a good agreement between the numerical and experimental results. The most significant difference is that the numerical prediction underestimates the $\theta^\star$ values for W1H3. This is to be expected as a similar discrepancy is observed in figure 3.13.

Overall, the model tends to under-predict the jet angle, but performs well on the curve shape and trends. The position of the maximum jet angle, $x^\star$, is especially well predicted.

3.6 Conclusion

We have investigated the collapse of bubbles near a slot geometry using experiments and a simple numerical model. Our main observation is the variation of the jet angle with the horizontal position of the bubble. At the center of the slot the jet is directed straight downwards due to symmetry and far from the slot the surface acts as a flat boundary so the jet is also directed downwards. Between these two limits there is a peak jet angle deflection, angled away from the slot. The peak jet angle and position of

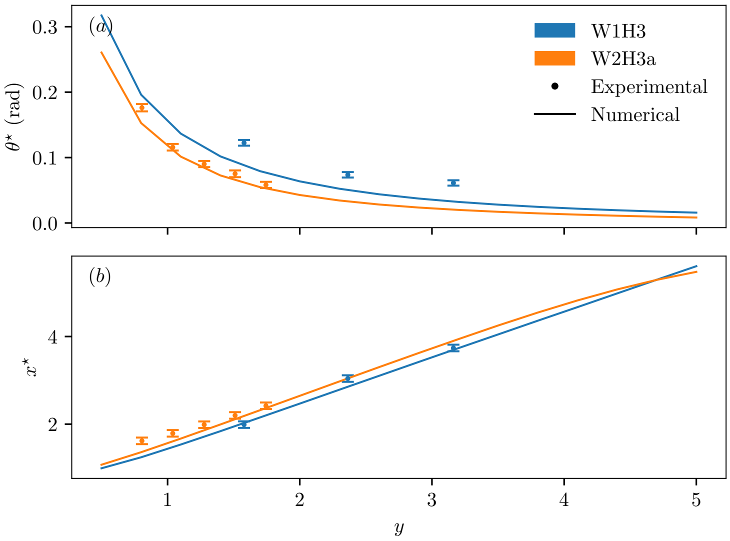

FIGURE 3.15: Experimental data points from two slots compared with boundary element method predictions for the same configurations. (*a*) Peak jet angle, $\theta^\star$, as a function of y. (*b*) Position of peak jet angle, $x^\star$, as a function of y. Slot W1H3 has $h = 2.23$. Slot W2H3a has $h = 1.23$. Experimental data is plotted as dots, numerical model predictions are solid lines.

the peak jet angle both tend to a limiting value as the slot height increases. This shows that, for slots of sufficient height, the jet angle depends only on the bubble position. As the vertical position of the bubble increases, the peak jet angle decreases and the horizontal position of the peak increases. For $h >> 1$, the position of the peak jet angle is directly proportional to the vertical distance: $x^\star \propto y$. When the jet angle and horizontal position are normalised by their respective peak values, we find that all jet angle curves collapse.

In this research we do not present any quantitative analysis of the strength of the jet, however we can make some qualitative predictions. For a simple flat boundary, jet strength depends on the distance between the bubble and the boundary. For a slot there is the distance to the slot surface and the distance to the slot floor. Far from the slot the jet strength would depend on the distance from the slot surface. Above an infinitely wide slot the jet strength would depend on the distance from the slot floor. We may conclude that near a finite slot the jet strength would be between these two limiting cases but quantifying the exact behaviour will require further experiments.

The numerical model has a tendency to under-predict the jet angle compared to experimental data gathered in this research, although it is often within reasonable error. The numerical model predictions very closely follow the shape and overall trends of the data, and provide a good prediction of the position of the peak jet angle, $x^\star$. In addition, the collapsed curve predicted by the numerical model matches the collapsed curve found from the experimental data. These comparisons serve to validate the numerical model presented in this research and provide a good basis from which to continue the study of complex geometries using this model. The velocity profile of the fluid in and around the slot can also be predicted by this model, although further investigation would be required to validate the predicted profiles.

In the context of cleaning with bubbles, particularly with ultrasonic cavitation, this research suggests that slots in surfaces to be cleaned would likely experience fewer jet impacts because bubbles would be drawn away from the slots rather than into them, and thus be cleaned less rigorously than the rest of the surface. Where cavitation damage is a problem this property could also be used to protect sensitive components by recessing them within slots, although this technique would likely have other implications depending on the flow conditions and requirements of the components.

Although we do not quantify the cleaning or damage effects here, these areas have been extensively studied previously using simple geometries. Our research provides a valuable step towards applying this knowledge to the more complex geometries that are found in many real-world applications.

Chapter 4

Modelling bubble collapse anisotropy in complex geometries

This chapter is based on a paper that has been published in Physical Review Fluids (Andrews & Peters, 2022).

4.1 Abstract

A gas or vapour bubble collapsing in the vicinity of a rigid boundary displaces towards the boundary and produces a high-speed jet directed at the boundary. This behavior has been shown to be a function of the 'anisotropy' of the collapse, measured by a dimensionless representation of the Kelvin impulse known as the anisotropy parameter (Supponen *et al.*, 2016). However, characterisation of the anisotropy parameter in different geometries has been limited to simplified analytic solutions. In this work we develop an inexpensive numerical model, based on the Boundary Element Method, capable of predicting the anisotropy parameter for any rigid complex geometry. We experimentally explore a robust measure of bubble displacement, showing that the bubble displacement in a range of complex geometries behaves as a single function of the predicted anisotropy parameter values.

4.2 Introduction

Collapsing bubbles have been studied in great depth for many years due to their ubiquity in both nature and engineering. Common applications include cavitation damage (Rayleigh, 1917; Luo *et al.*, 2016; Lu *et al.*, 2016; Sagar & el Moctar, 2020), cleaning (Ohl *et al.*, 2006; Verhaagen & Fernández Rivas, 2016; Birkin *et al.*, 2016; Chahine *et al.*, 2016;

Verhaagen *et al.*, 2016; Reuter *et al.*, 2017), and various biomedical applications (De La Torre, 1992; Palanker *et al.*, 2002; Brennen, 2003; Canchi *et al.*, 2017; Oyarte Gálvez *et al.*, 2020). Although many such applications feature numerous bubbles collapsing, it is important to study the fundamental behavior of individual bubbles to identify how key parameters affect the collapse behaviour. This study goes as far back as Rayleigh (1917) where a single spherical void collapsing in an infinite fluid was treated. The study of single bubbles collapsing has since grown significantly, addressing a wide range of questions. Studies have experimentally and numerically investigated a wide variety of bubble collapse properties such as bubble collapse shapes (Blake *et al.*, 1986; Brujan *et al.*, 2019; Zhang *et al.*, 2020), induced pressures (Benjamin & Ellis, 1966; Li *et al.*, 2015, 2016; Supponen *et al.*, 2019), boundary shear stresses (Dijkink & Ohl, 2008; Koukouvinis *et al.*, 2018; Zeng *et al.*, 2018; Gonzalez-Avila *et al.*, 2020*a*; Zeng *et al.*, 2022), and shock wave properties (Tagawa *et al.*, 2016; Sinibaldi *et al.*, 2019; Trummler *et al.*, 2021). Much of this research focuses on simple boundary geometries such as flat plates, free surfaces, constant pressure gradients, and other boundaries for which analytic solutions of the flow field exist. In recent years, there has been increasing interest in complex geometries. For example, studies have explored jet direction for various complex geometries (Tagawa & Peters, 2018; Molefe & Peters, 2019; Andrews *et al.*, 2020), bubble dynamics near curved rigid surfaces (Tomita *et al.*, 2002), dynamics in combinations of boundaries and free surfaces (Zhang *et al.*, 2017; Quah *et al.*, 2018; Kiyama *et al.*, 2021), jetting and shear stress between two walls (Han *et al.*, 2018; Gonzalez-Avila *et al.*, 2020*a*), and bubble shape variation at the corner of a rigid wall Zhang *et al.* (2020).

Many parameters of the dynamics of a bubble collapsing near a flat plate depend on the standoff distance $\gamma = Y/R_0$ where Y is the distance from a boundary or fluid interface and R_0 is the maximum bubble size (Kröninger *et al.*, 2010; Supponen *et al.*, 2016; Zeng *et al.*, 2022). However, for more complex geometries, it is difficult to define a geometric equivalent to the standoff parameter. Even with very limited complexity, such as in a corner, it is not trivial to define such a parameter.

The Kelvin impulse is a parameter that captures the overall motion of the fluid. The Kelvin impulse is the net force acting on the fluid integrated over time, effectively the total fluid momentum. This parameter was described well by Benjamin & Ellis (1966) and has been studied analytically and numerically for many years (Blake & Cerone, 1982; Blake *et al.*, 1986; Kucera & Blake, 1990; Harris, 1996; Blake *et al.*, 2015). More recently, Supponen *et al.* (2016) presented a dimensionless version of the Kelvin impulse called the anisotropy parameter, denoted ζ. Analytic solutions for the anisotropy parameter were derived for a number of different sources of anisotropy and many bubble collapse properties have been shown to be functions of the anisotropy parameter, regardless of the source of anisotropy. For example, jet speed, bubble displacement, jet volume (Supponen *et al.*, 2016), shockwave energy (Supponen *et al.*, 2017), and rebound energy (Supponen *et al.*, 2018). Thus, the anisotropy parameter is a powerful tool for predicting bubble collapse behaviour.

Harris (1996) presented a simple boundary element model for estimating the Kelvin impulse for a bubble near a complex geometry. In the current research, we present a similar model that predicts the Kelvin impulse for complex geometries. We extend this model by non-dimensionalizing the results to produce the anisotropy parameter following the example of Supponen *et al.* (2016). With this model, anisotropy parameter values can be predicted for complex geometries whereas they were previously only studied for geometries with limited analytic solutions. The study of bubble collapse properties as functions of anisotropy magnitude can thus be extended to complex geometries.

4.3 Methods

In this section, the procedure for calculating the general Kelvin impulse is derived and the procedure for converting this to the anisotropy parameter is presented. These calculations rely on numerical solutions to the Rayleigh-Plesset equation so various formulations of the Rayleigh-Plesset equation are compared. Three methods for computing the anisotropy parameter for a range of geometries are then presented. Finally, the data analysis techniques used to process experimental results are outlined.

4.3.1 Computing the anisotropy parameter

The Kelvin impulse, $\mathbf{I}(\tau)$, of a fluid during the time period $0 < t < \tau$ can be represented as the integral of the force acting on the fluid over time,

$$\mathbf{I}(\tau) = \int_0^\tau \mathbf{F}(t)dt, \tag{4.1}$$

where τ is an arbitrary point in time and the force $\mathbf{F}(t)$ acting on the fluid is equal and opposite to the force the fluid exerts on the bounds of the domain. For a bubble in an infinite fluid bounded only by a rigid geometry, and following the derivation of Blake & Cerone (1982), this force can be written as

$$\mathbf{F}(t) = -\rho_L \int_S \left[\frac{1}{2}|\nabla\phi|^2\mathbf{n} - \frac{\partial\phi}{\partial n}\nabla\phi\right] dS, \tag{4.2}$$

where ρ_L is the surrounding fluid density, S is the boundary surface, and $\mathbf{n}$ is a vector normal to the surface S. Potential flow is assumed with velocity potential ϕ and $\partial\phi/\partial n$ is the derivative of the potential in the normal direction. Note here that the sign varies from previous works (Blake & Cerone, 1982; Blake, 1988; Harris, 1996) where the normal vector is defined as outward from the domain. In equation 4.2 the normal vector is defined as inward to the domain in accordance with the convention used in this work for the boundary element method.

On the surface of the boundary, the normal velocity $\partial\phi/\partial n = 0$ (Harris, 1996) and thus the force reduces to the integral of the dynamic pressure on the boundary

$$\mathbf{F}(t) = -\frac{1}{2}\rho_L \int_S |\nabla\phi|^2 \mathbf{n} dS. \tag{4.3}$$

The bubble and all boundaries are modelled using point sinks. The strength of these sinks scales directly with the bubble sink strength $m_b(t)$ which varies with time. Thus, we can express the velocity $\nabla\phi$ induced at a position j by a boundary element sink as the bubble sink strength multiplied by the equivalent velocity $\nabla\phi'$ when the bubble sink strength is $m_b = 1\ \mathrm{m}^3\ \mathrm{s}^{-1}$. Properties computed with $m_b = 1\ \mathrm{m}^3\ \mathrm{s}^{-1}$ are denoted by a prime. As such this velocity is denoted $\nabla\phi'$ and we can write

$$\nabla\phi|_j = m_b(t)\nabla\phi'|_j. \tag{4.4}$$

We therefore express the force as

$$\mathbf{F}(t) = -\frac{1}{2}\rho_L \int_S |m_b(t)\nabla\phi_j'|^2 \mathbf{n} dS = m_b(t)^2 \left[-\frac{1}{2}\rho_L \int_S |\nabla\phi_j'|^2 \mathbf{n} dS \right] = m_b(t)^2 \mathbf{F}', \tag{4.5}$$

such that

$$\mathbf{F}' = -\frac{1}{2}\rho_L \int_S |\nabla\phi_j'|^2 \mathbf{n} dS, \tag{4.6}$$

where $\mathbf{F}'$ is the equivalent force for a bubble sink strength of $m_b = 1\ \mathrm{m}^3\ \mathrm{s}^{-1}$. $\mathbf{F}'$ is time-independent, purely depending on the geometry and bubble position, which is assumed to be fixed. Different methods for calculating $\mathbf{F}'$ are presented in sections 4.3.3.1 to 4.3.3.3.

Thus, combining equations (4.1) and (4.5), the impulse integral equation becomes

$$\mathbf{I}(\tau) = \mathbf{F}' \int_0^\tau m_b(t)^2 dt. \tag{4.7}$$

By assuming that the bubble remains spherical throughout the collapse, and defining the bubble sink strength to be the rate of change of bubble volume V, the sink strength is given by

$$m_b(t) = \frac{dV}{dt} = 4\pi R^2 \dot{R} \tag{4.8}$$

where R is the bubble radius and $\dot{R}$ is the time-derivative of bubble radius.

The Kelvin impulse therefore becomes

$$\mathbf{I}(\tau) = \mathbf{F}' \int_0^\tau \left[4\pi R^2 \dot{R}\right]^2 dt = 16\pi^2 \mathbf{F}' \int_0^\tau R^4 \dot{R}^2 dt. \tag{4.9}$$

which can be computed using a numerical solution to the Rayleigh-Plesset equation.

A scaling between the anisotropy parameter $\boldsymbol{\zeta}$ and Kelvin impulse $\mathbf{I}$ was presented by Supponen *et al.* (2016),

$$\mathbf{I} = 4.789 R_0^3 \sqrt{\Delta p \rho} \boldsymbol{\zeta} \tag{4.10}$$

where R_0 is the initial radius of the bubble, which is taken to be its maximum size; Δp is the difference between the pressure at an infinite distance and the internal pressure of the bubble; and ρ is the density of the liquid. This relation was analytically derived from the initial expansion and subsequent collapse of a bubble collapsing in a pressure gradient.

Thus, equations (4.9) and (4.10) can be combined to determine the anisotropy parameter for any geometry,

$$\boldsymbol{\zeta} = \frac{16\pi^2 \mathbf{F}'}{4.789 R_0^3 \sqrt{\Delta p \rho}} \int_0^\tau R^4 \dot{R}^2 dt \tag{4.11}$$

where τ is now the duration of the initial expansion and collapse.

The vector anisotropy parameter $\boldsymbol{\zeta}$ represents both a magnitude and direction. The direction is equivalent to that previously used to study jet direction in complex geometries (Tagawa & Peters, 2018; Molefe & Peters, 2019; Andrews *et al.*, 2020). In this work we focus on the magnitude, represented by the scalar anisotropy parameter ζ.

4.3.2 Formulations of the Rayleigh-Plesset equation

In order to numerically solve the integral in equation 4.11, the radius R and radial velocity $\dot{R}$ must be known. In order to compute these we use the Rayleigh-Plesset equation which has long been the standard model of bubble collapse. Various modifications have been derived for differing conditions and assumptions. By assuming that the bubble collapse is primarily inertial, in an incompressible liquid, with no heat transferred across the bubble boundary, and with internal gas that behaves isentropically (Brennen, 1995), the Rayleigh-Plesset equation is

$$\frac{-\Delta p}{\rho_L} + \frac{p_{G_0}}{\rho_L} \left(\frac{R_0}{R}\right)^{3k} = R\ddot{R} + \frac{3}{2}\dot{R}^2 + \frac{4\nu_L}{R}\dot{R} + \frac{2s}{\rho_L R} \tag{4.12}$$

where Δp is the driving pressure of the collapse, often defined as $p_\infty - p_V$ where p_V is the vapour pressure of water and p_∞ is the far-field pressure; p_{G_0} is the initial pressure of gas inside the bubble; ρ_L and ν_L are the density and kinematic viscosity of the liquid, respectively; s is the surface tension; and k is the ratio of specific heats of water vapour $k = c_p/c_v \approx 1.33$.

A derivation of the Rayleigh-Plesset equation was presented by Harris (1996) that includes the effect of a nearby rigid wall and the buoyancy of the bubble,

$$\frac{-p_\infty}{\rho_L} + \frac{p_{G_0}}{\rho_L}\left(\frac{R_0}{R}\right)^{3k} + gz = R\ddot{R} + \frac{3}{2}\dot{R}^2 - \frac{\partial \phi_w}{\partial t} \tag{4.13}$$

where ϕ_w is the velocity potential induced by the wall at the bubble position; g is the acceleration due to gravity; and z is the depth of the bubble in the water.

Here we shall present a comparison between four different models and experimental data. The first model is equation 4.12, denoted 'Complete'. The second model is the same, but neglecting the effects of viscosity and surface tension, denoted 'Inertial'. The third model, denoted 'Wall model', is based on equation 4.13, however the effect of buoyancy is neglected and p_∞ is replaced by Δp for consistent comparison with the other models. The final model, denoted 'No internal gas', assumes a constant pressure difference between the inside and outside of the bubble, effectively assuming that there is no internal gas to be compressed. This model is used by Obreschkow *et al.* (2012) in order to find analytical approximations to the solution. The equations for each of these models are as follows:

$$\frac{-\Delta p}{\rho_L} + \frac{p_{G_0}}{\rho_L}\left(\frac{R_0}{R}\right)^{3k} = R\ddot{R} + \frac{3}{2}\dot{R}^2 + \frac{4\nu_L}{R}\dot{R} + \frac{2s}{\rho_L R} \tag{Complete}$$

$$\frac{-\Delta p}{\rho_L} + \frac{p_{G_0}}{\rho_L}\left(\frac{R_0}{R}\right)^{3k} = R\ddot{R} + \frac{3}{2}\dot{R}^2 \tag{Inertial}$$

$$\frac{-\Delta p}{\rho_L} + \frac{p_{G_0}}{\rho_L}\left(\frac{R_0}{R}\right)^{3k} = R\ddot{R} + \frac{3}{2}\dot{R}^2 - \frac{\partial \phi_w}{\partial t} \tag{Wall model}$$

$$\frac{-\Delta p}{\rho_L} = R\ddot{R} + \frac{3}{2}\dot{R}^2 \tag{No internal gas}$$

Figure 4.1 shows the comparison between these models and experimental data. For simple comparison, the models are initiated at maximum bubble size with internal pressure equal to the vapour pressure of water. For most models, and experimental data, the bubbles collapse to a minimum size and then rebound. Notably, around the minimum size the bubble collapses and rebounds very fast. Due to limitations in the temporal resolution of the high-speed camera, the experimental data do not accurately capture the minimum size of the bubble.

After rebound, all of the Rayleigh-Plesset models with internal gas recover very close to their initial size, whereas the experimental data shows that the bubbles do not achieve their original size due to significant energy being dissipated during the collapse.

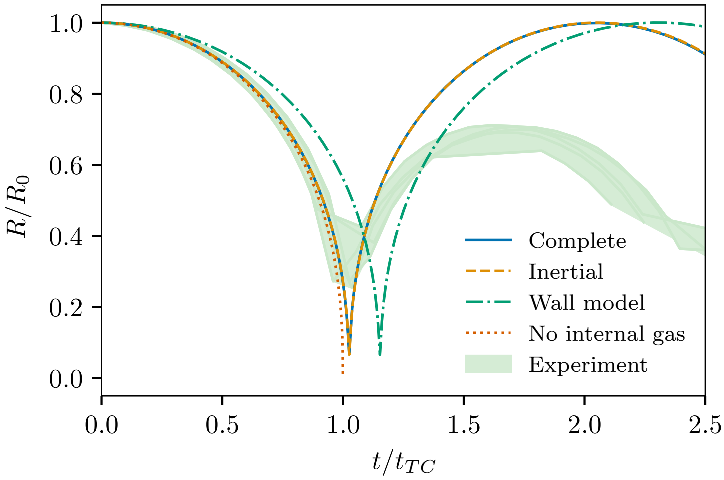

FIGURE 4.1: A comparison between the four Rayleigh-Plesset models and experimental data. The experimental data used here are a series of five bubbles generated in the same location near a slot, the green shaded area shows the spread of the data. The experimental mean of the radius and position at the maximum bubble size are used as the initial conditions for numerical models. Bubbles ranged in size from $R_0 = 1.13$ mm to $R_0 = 1.34$ mm. Radius is normalised with the initial radius R_0 and time is normalised with the Rayleigh collapse time t_{TC} (Rayleigh, 1917).

Comparing the two standard models, one with viscosity and surface tension ('Complete') and one without ('Inertial'), it is clear that viscosity and surface tension are negligible for this regime of bubble collapse.

The model that includes the effect of a nearby wall ('Wall model') consistently overestimates the collapse duration when compared to experimental data. This is likely due to the assumption of spherical symmetry in the model. In reality, the side of a bubble opposite to a nearby boundary does not get impeded by the boundary. However, the wall model assumes spherical symmetry, which means all sides of the bubble are considered to be equally impeded, resulting in a generally slower collapse.

In comparison with experimental data, the 'Complete', 'Inertial', and 'No internal gas' models all match well. In general, a benefit of the Kelvin impulse model presented in this work is that any model for the bubble radius variation with time can be used without significant methodological modifications. From here onwards, we utilise the 'Inertial' model as it is the simplest model that can capture bubble rebounds.

4.3.3 Anisotropy parameter solutions

Now that we have defined the anisotropy parameter and selected a collapse model, we will proceed to present three solution methods. We will start with analytic solutions, followed by semi-analytic and boundary element methods. All of these models rely on several key assumptions. The fluid is assumed to be incompressible, irrotational, and inviscid. Therefore, potential flow can be assumed. The bubble is considered to be spherically symmetrical with only the bubble radius varying with time.

4.3.3.1 Analytic

Much previous research has focused on calculating the Kelvin impulse analytically. Supponen *et al.* (2016) have presented anisotropy parameter solutions for several flow conditions. We include the solution for a flat plate here for completeness.

Treating the collapsing bubble as a sink in potential flow allows a solid boundary to be modelled using the method of images. This can then be solved for $\mathbf{F}'$ and the Kelvin impulse $\mathbf{I}$ (Blake, 1988) yielding the equations

$$\mathbf{F}' = -\frac{\rho_L \mathbf{n}}{16\pi Y^2} \tag{4.14}$$

$$\mathbf{I} = -0.934 R_0^3 \sqrt{\Delta p \rho_L} \gamma^{-2} \mathbf{n} \tag{4.15}$$

where Y is the distance from the boundary; $\gamma = Y/R_0$ is the standoff distance; and Δp is the initial difference between the pressure an infinite distance from the bubble and the internal pressure of the bubble, $\Delta p = p_\infty - p_V$.

Substituting equation 4.15 into equation 4.10 yields

$$\zeta = -0.195\gamma^{-2}\mathbf{n}. \tag{4.16}$$

4.3.3.2 Semi-analytic

The flow field of a set of geometries can also be solved with the method of images. In particular, these include bubbles in corner geometries (Tagawa & Peters, 2018) and bubbles inside square and triangular prisms (Molefe & Peters, 2019). The triangular prisms are limited to the three tessellating cases: equilateral triangles, isosceles right triangles, and 30°-60°-90° triangles. Although an analytic description of the flow can be achieved, solving for the Kelvin impulse quickly becomes rather involved. Therefore, we numerically integrate the pressure over the boundary on a mesh in order to calculate the Kelvin impulse. This allows these analytic models to be extended numerically. The velocity at a point is

$$\nabla\phi|_j = \sum_{i=0}^{M} m_b \frac{(\mathbf{x}_j - \mathbf{x}_i)}{4\pi|\mathbf{x}_j - \mathbf{x}_i|^3} = m_b \left[\sum_{i=0}^{M} \frac{(\mathbf{x}_j - \mathbf{x}_i)}{4\pi|\mathbf{x}_j - \mathbf{x}_i|^3}\right] = m_b \nabla\phi_j' \tag{4.17}$$

where j is any point $j \neq i$ and M is the total number of mirror sinks. $i = 0$ represents the bubble sink and $i > 0$ represent the mirror sinks. Although an infinite number of mirror sinks would be required to exactly match the boundary conditions, relatively few are required to adequately predict the anisotropy value.

Thus,

$$\nabla\phi'_j = \sum_{i=0}^{M} \frac{(\mathbf{x}_j - \mathbf{x}_i)}{4\pi|\mathbf{x}_j - \mathbf{x}_i|^3}. \tag{4.18}$$

By assuming that the pressure is constant across an element in the boundary mesh, equation 4.6 can be discretised over the boundary elements to get

$$\mathbf{F}' = -\frac{1}{2}\rho_L \sum_{j=1}^{N} A_j |\nabla\phi'_j|^2 \mathbf{n}_j. \tag{4.19}$$

where the points j are the centroids of each boundary element, A_j is the area of the boundary element at j, and N is the total number of boundary elements.

Equation 4.18 is substituted into equation 4.19 which is combined with equation 4.11 and solved numerically for the anisotropy parameter ζ.

4.3.3.3 Boundary element method

We use the boundary element method to model geometries for which the flow field cannot be solved analytically. The boundary element method is a potential flow model that represents a boundary as a discretised distribution of potential flow elements. The full derivation and solution methodology used here is discussed in chapter 3 and the main steps are summarised again here. Each element i of the boundary is represented as a single sink, positioned at the centroid of the element $\mathbf{x}_i$. The element is assumed to have a sink density σ_i that is constant over its area A_i such that the single sink has strength $\sigma_i A_i$. Thus, the velocity induced by an element is defined as

$$\nabla\phi|_j = \frac{\sigma_i A_i (\mathbf{x}_j - \mathbf{x}_i)}{4\pi|\mathbf{x}_j - \mathbf{x}_i|^3}, \tag{4.20}$$

where j is any point such that $\mathbf{x}_j \neq \mathbf{x}_i$.

Considering both the bubble and any boundaries, for any boundary element centroid point j, the velocity is given by the sum of the bubble sink and N boundary element sinks

$$\nabla\phi|_j = \nabla\phi_b|_j + \nabla\phi_w|_j = \frac{m_b(\mathbf{x}_j - \mathbf{x}_b)}{4\pi|\mathbf{x}_j - \mathbf{x}_b|^3} + \sum_{i=1, i\neq j}^{N} m_b \frac{\sigma'_i A_i (\mathbf{x}_j - \mathbf{x}_i)}{4\pi|\mathbf{x}_j - \mathbf{x}_i|^3} + \frac{m_b \sigma'_j}{2}\mathbf{n}_j. \tag{4.21}$$

The summation of boundary element sinks is valid for any position $i \neq j$. When $i = j$ a singularity would be encountered. In the normal direction this is treated with the standard $\nabla\phi|_j \cdot \mathbf{n}_j = \sigma_j/2$. An element is assumed to have no net effect on the tangential velocity at its centroid so no additional term is included. Note again that the boundary sink densities scale directly with the bubble sink strength such that $\sigma_j = m_b\sigma'_j$ where σ'_j is the boundary sink strength densities computed for $m_b = 1\ \mathrm{m}^3\ \mathrm{s}^{-1}$.

Thus, the velocity $\nabla\phi$ at any given bubble position, geometry, and time can be represented by a constant vector $\nabla\phi'$ multiplied by the bubble sink strength

$$\nabla\phi|_j = m_b \left[\frac{(\mathbf{x}_j - \mathbf{x}_b)}{4\pi|\mathbf{x}_j - \mathbf{x}_b|^3} + \sum_{i=1, i\neq j}^{N} \frac{\sigma'_i A_i (\mathbf{x}_j - \mathbf{x}_i)}{4\pi|\mathbf{x}_j - \mathbf{x}_i|^3} + \frac{\sigma'_j}{2}\mathbf{n} \right] = m_b \nabla\phi'_j, \tag{4.22}$$

such that

$$\nabla\phi'_j = \frac{(\mathbf{x}_j - \mathbf{x}_b)}{4\pi|\mathbf{x}_j - \mathbf{x}_b|^3} + \sum_{i=1, i\neq j}^{N} \frac{\sigma'_i A_i (\mathbf{x}_j - \mathbf{x}_i)}{4\pi|\mathbf{x}_j - \mathbf{x}_i|^3} + \frac{\sigma'_j}{2}\mathbf{n}. \tag{4.23}$$

As with the semi-analytic solution, equation 4.6 is discretised to produce equation 4.19, which is combined with equation 4.23 to compute $\mathbf{F}'$. This $\mathbf{F}'$ is then substituted into equation 4.11 and solved numerically for the anisotropy parameter ζ.

4.3.4 Experimental data and analysis

Bubble displacement is defined by its direction and distance. Previous work has characterised the bubble displacement direction in complex geometries (Tagawa & Peters, 2018; Molefe & Peters, 2019; Andrews *et al.*, 2020). Here, we characterise the bubble displacement distance. The displacement distance Δ is measured from the position at the initial maximum size of the bubble and terminating at the position of the bubble at its maximum rebound size.

Some previous work has measured the bubble displacement from inception to end of the first collapse (Supponen *et al.*, 2016). However, this measurement is difficult due to the very rapid growth, collapse, and movement of the bubble at these points in time. Conversely, at its maximum size, the bubble has a minimum rate of change of radius and minimum displacement velocity. Thus, measuring the bubble at the size maxima yields more robust measurements.

In addition to the bubble displacement, we measure the rebound size of the bubble R_1. In this work, the displacement and rebound size are both normalised by the maximum bubble radius R_0. These measurements are described in chapter 2.

Experimental data used in this chapter are from prior investigations of jet direction for bubbles in corner geometries (Tagawa & Peters, 2018; Peters & Tagawa, 2018), inside triangular and square prisms (Molefe & Peters, 2019; Peters & Molefe, 2019), and the slot geometries data from chapter 3. All of these experiments used laser-induced cavitation, with a microscope objective as the focusing optic as described in section 2.1.1. In addition to the data from the previous studies, data has been gathered for a flat plate using the same experimental setup.

4.4 Results and discussion

In this section we apply our numerical framework to a series of geometries with varying complexity. We begin by comparing models, we then generate anisotropy magnitude maps for four complex geometries, and finally show that experimental data collapses when combined with anisotropy parameter predictions.

4.4.1 Numerical anisotropy parameter calculations

4.4.1.1 Flat plate model comparison

We start with a flat plate geometry, which can be treated with all three models: analytic, semi-analytic, and boundary element method. The analytic solution is $\zeta = 0.195\gamma^{-2}$ which is simply the magnitude of equation 4.16. The semi-analytic solution uses a mirror sink and integrates the pressure over the boundary on the mesh of a 1 m^2 plate. The boundary element method solution uses the same mesh as the semi-analytic solution to compute boundary sink strengths and the pressure integration. In this comparison the mesh consisted of 18 020 elements with most elements concentrated in the central region. Element lengths ranged between 0.4 mm and 13.9 mm. The bubbles were positioned at $Y = 5$ mm from the boundary and the bubble radius R_0 was varied between 0.5 mm and 5 mm to produce a range of standoff distances between 1 and 10.

As $\mathbf{F}'$ depends only on bubble position, the series of bubbles can be characterised by a single $\mathbf{F}'$ value. The semi-analytic model produced an $\mathbf{F}'$ value 0.5% lower than the analytic model and the boundary element method model produced an $\mathbf{F}'$ value 3.2% lower than the analytic model. As is evident from equation 4.11, these cause a proportional decrease in the measured anisotropy magnitude. Figure 4.2(*a*) shows the comparison between the anisotropy magnitude values calculated by these models. Both the semi-analytic and boundary element method solutions predict lower anisotropy magnitude values than the analytic solution, this is in part due to integrating the pressure over a finite plate rather than the infinite plate assumed by the analytic solution. There is also some difference due to the discretization of the boundary. For the semi-analytic solution the discretization is only for the integration of pressure over the boundary, while for the boundary element method solution the discretization is in boundary conditions, flow solution, and also the integration of pressure. Finally, there is some difference due to the Rayleigh-Plesset model used. The analytic solution uses a 'No internal gas' type model whereas the other two solutions use the 'Inertial' model. Despite these differences, the three models produce very consistent anisotropy parameter values, and we conclude that the model is insensitive to these details.

Figure 4.2(*b*) shows convergence plots of both the boundary element method solution and the semi-analytic model solution for $\gamma = 1$. Here, L_{fine} is the length of the smallest element and is normalised with the bubble maximum radius. ϵ is the absolute difference between the numerical solutions and the analytic solutions divided by the analytic solution value. The semi-analytic solution has a lower difference but both methods converge towards the analytic solution as the element size is decreased.

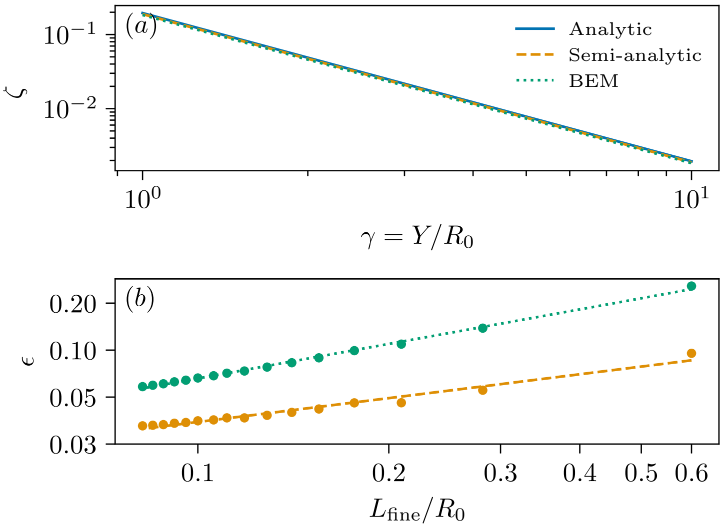

FIGURE 4.2: (*a*) The anisotropy parameter ζ against standoff γ for a simple flat plate, compared between the analytic, semi-analytic, and boundary element method models, showing a near-perfect match. (*b*) Convergence plots of both the boundary element method solution and the semi-analytic model solution for $\gamma = 1$. ϵ is the absolute difference between each solution and the analytic solution, normalised by the analytic solution. L_{fine} is the smallest element length.

4.4.1.2 Anisotropy maps for complex geometries

Unlike the analytic and semi-analytic models, the boundary element method can be applied to any geometry. In addition, the most expensive part of the boundary element method only needs to be calculated once for any geometry and the result can be used for all bubble positions. However, it is vulnerable to ill-conditioned geometries. Although this is generally unlikely to occur, it is a significant problem for very regular, highly enclosed geometries such as the prisms presented by Molefe & Peters (2019). In contrast, the semi-analytic method can operate with far fewer sinks and is stable for all valid geometries, but the full calculation must be performed for every bubble position.

The primary computational limitation of the boundary element method is the memory usage. Memory usage scales with N^2 where N is the number of boundary elements. The semi-analytic method separates this scaling into two parts: N points on the pressure mesh and M mirror sinks. The memory thus scales with NM. Where the semi-analytic model is possible, far fewer sinks M are required to model the boundary compared to the boundary element method, so far more sinks N can be used to model the pressure mesh within the same memory constraint. This allows for the pressure to be more precisely resolved.

Here we present anisotropy magnitude maps for a selection of complex geometries. Figure 4.3(*a*) shows an anisotropy magnitude map for a slot geometry of the type treated in chapter 3. The slot has a width and height $W = H = 8R_0$ for $R_0 = 0.5$ mm. $N = 22\ 939$ elements were used to resolve the boundary. In contrast to the previous work, the bubble size here is important as it is required for computing the anisotropy magnitude. Due to the finite size of the bubble, anisotropy values extremely close to the boundary do not have a clear physical meaning despite being numerically feasible. Thus, the white area near the boundary in figure 4.3(*a*) is an area of width R_0 for which the anisotropy magnitude was not computed.

At a large horizontal distance from the center of the slot, corresponding to the most negative x values in figure 4.3(*b*), the boundary becomes similar to a flat plate, with the anisotropy magnitude depending primarily on the vertical standoff distance $\gamma = Y/R_0$. As the bubble horizontally approaches the slot, the slot causes a general reduction in anisotropy due to the increase of fluid volume below the bubble. At the center of the slot, the anisotropy contributions from the slot sides cancel out horizontally due to symmetry. The anisotropy is found to be strongest in the bottom corners of the slot where the bubble is most confined on one side but not the other.

Figure 4.3(*b*) shows anisotropy magnitude curves for five different horizontal positions with a range of standoff values where the standoff $\gamma = Y/R_0$. These are compared to the anisotropy magnitude for a flat plate. Far from the slot horizontally, the $x = -5$ curve is very close to the flat plate curve as the effect of the slot is minimal. For horizontal positions closer to the slot, these curves deviate significantly from the flat plate curve.

The anisotropy magnitude for triangular prisms, square prisms, and corner geometries were calculated using the semi-analytic method. Figure 4.4 shows contour plots for anisotropy magnitude in triangular (figure 4.4(*a*)) and square (figure 4.4(*b*)) prisms of the type treated by Molefe & Peters (2019) and in a corner of the type treated by Tagawa & Peters (2018) (figure 4.4(*c*)). For the same reason as given for the slot geometries, anisotropy was not calculated in the white areas near the boundaries. The two prisms have side length $L = 15R_0$. The triangular prism used $M = 12\ 675$ image sinks and the square prism used $M = 4225$ image sinks, both with $N \approx 20\ 000$ elements in the

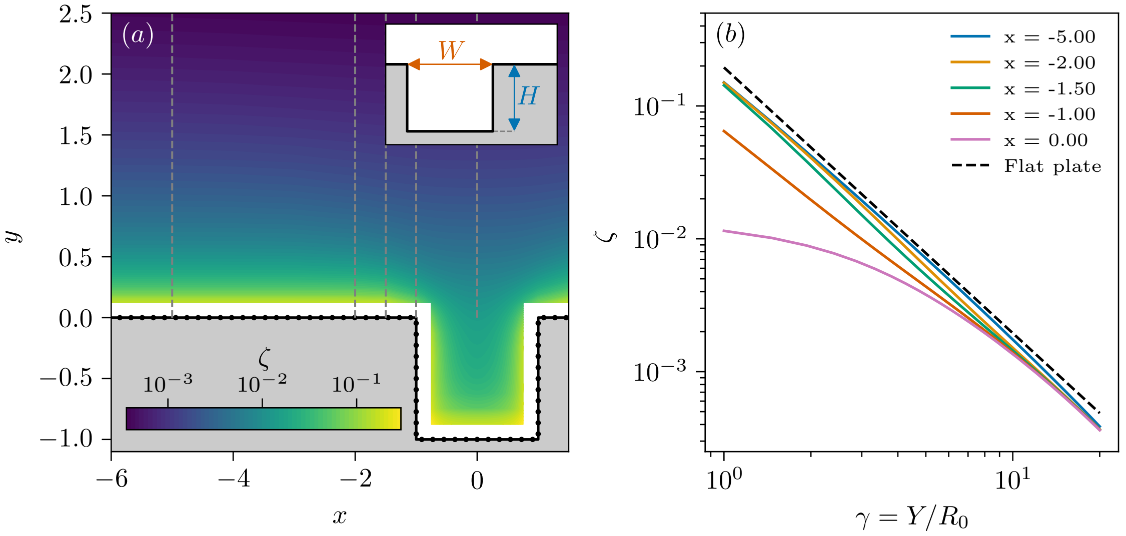

FIGURE 4.3: (*a*) A contour plot of anisotropy magnitude for bubbles positioned around a slot with $H/W = 1$, $W/R_0 = 8$ and $R_0 = 0.5$ mm. $x = 2X/W$ and $y = Y/W$ where X is the horizontal position of the bubble from the slot center, Y is the vertical position of the bubble from the upper surface, and W is the slot width as in chapter 3. The slot boundary is indicated in solid black with boundary sink positions displayed as black dots. Grey dashed lines correspond to the horizontal positions in (*b*). (*b*) Anisotropy magnitude against standoff distance from the upper surface of the slot for five horizontal positions. The dashed line is the analytic solution for a flat plate.

pressure mesh. The corner has an internal angle $\theta_c = \pi/3$ and thus used $M = 5$ mirror sinks. Here the anisotropy is at a maximum near the corners of each shape showing similar tendencies as the slot geometry. Towards the center of the shape, bubbles experience decreasing anisotropy as the bubble collapse is less impeded by the boundaries. At the exact center of the prisms, the anisotropy is expected to be zero due to symmetry.

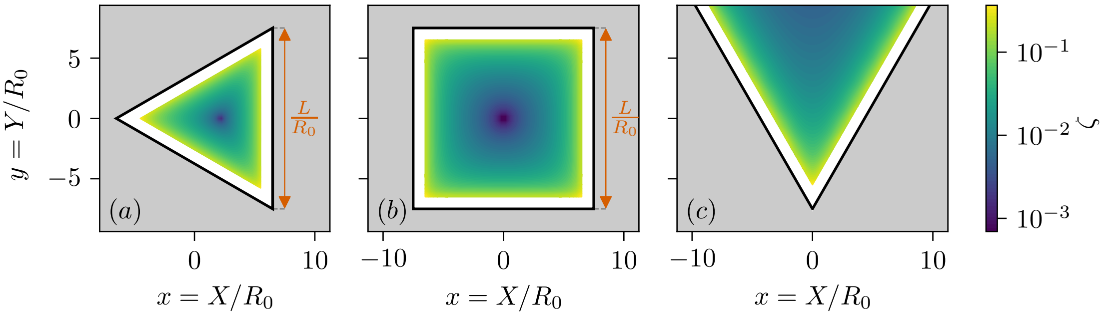

FIGURE 4.4: (*a*) A contour plot of anisotropy magnitude for bubbles positioned in an equilateral triangular prism. $L/R_0 = 15$ where L is the side length of the triangle. (*b*) A contour plot of anisotropy magnitude for bubbles positioned in a square prism. $L/R_0 = 15$ where L is the side length of the square. (*c*) A contour plot of anisotropy magnitude for bubbles positioned in a corner with angle $\theta_c = \pi/3$. These geometries are of the type investigated by Tagawa & Peters (2018) and Molefe & Peters (2019). The boundaries are indicated by solid black lines. The area outside of the fluid domain is shaded grey.

4.4.2 Experimental results

It has previously been shown that bubble displacement and rebound size depend on the anisotropy parameter (Supponen *et al.*, 2016, 2018). In this section we present experimental measurements of displacement and rebound size and compare them to anisotropy parameter predictions for each collapse event.

4.4.2.1 Data post-processing

The models presented in this work assume a spherical bubble. However, bubbles in experiments deviate from being perfectly spherical to varying degrees. When a bubble is initially nucleated a plasma is formed around the point at which the laser is focused. If the angle of convergence of the beam is too small (having a low equivalent numerical aperture), the energy density of the beam can remain high away from the laser focus. This leads to the plasma forming in an elongated shape, and sometimes even forming multiple separate spots of plasma (Tagawa *et al.*, 2016). This elongation leads to an oblate bubble at the maximum bubble size and increases the spread of data for measured displacement. Figure 4.5 demonstrates this occurrence. In the first frame, at $t = 0$ μs, the plasma is visible and is elongated to the point of having two almost-separated sections. In the second frame, at $t = 100$ μs where the bubble is at its maximum size, the bubble is slightly oblate. We quantify the deviation from a perfect sphere using the eccentricity of the bubble image, where eccentricity is defined as the eccentricity of an ellipse with second-moments equal to the bubble image region. At its maximum size, the bubble in figure 4.5 had a measured eccentricity of 0.36. By contrast, the bubble shown in figure 2.7 had an eccentricity of 0.25 at its maximum size. The third frame, at $t = 190$ μs, shows that the bubble collapses as expected. However, when it rebounds in the fourth frame at $t = 240$ μs, it retains the oblate deformation.

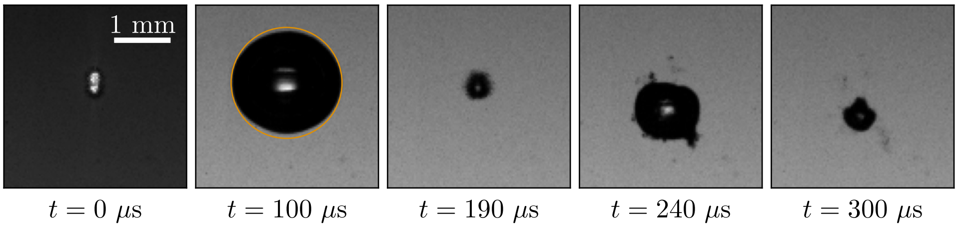

FIGURE 4.5: A series of frames showing a bubble collapsing near a slot. The laser enters from the top of frame. The frame at $t = 0$ μs shows the initial plasma generated by the laser. The orange line on the frame at $t = 100$ μs shows a perfect circle encompassing the bubble for comparison. The eccentricity of the bubble was 0.36 at $t = 100$ μs.

Bubbles that are deformed upon formation are expected to result in spread in experimental measurements. Figure 4.6 shows the spread of data as a function of bubble eccentricity at their maximum size. Here the spread is defined as the percentage difference between a data point and a power law curve that has been fitted across all data.

The curve fit used for this determination is shown in figure 4.7(*a*). Although the error bars are quite large in some areas of figure 4.6, it is clear that greater eccentricity leads to a greater spread in measured displacement. In order to compare consistent bubbles, and because we expect non-spherical bubbles to deviate most strongly from our model, we filter our experimental data by eccentricity. Thus, by filtering out highly eccentric bubbles, the spread of data can be reduced to more closely align with the idealised scenario of a spherical bubble. Filtered data are shown in figure 4.7 with unfiltered data shown in the inset plots. As expected, when the data are filtered, the spread of data reduces and many of the most significant outliers are removed. The eccentricity values used to filter these data are set separately for each geometry. Some geometries have many data points (the slots data set has 5094 points) whereas others have far fewer (the flat plate data set has only 82). Thus, much more stringent eccentricity filters are applied to larger data sets. Overall, with eccentricity limits varying between 0.2 (for slots) and 0.28 (for the flat plate), 2124 data points were retained after filtering across all data, comprising 31% of the available data.

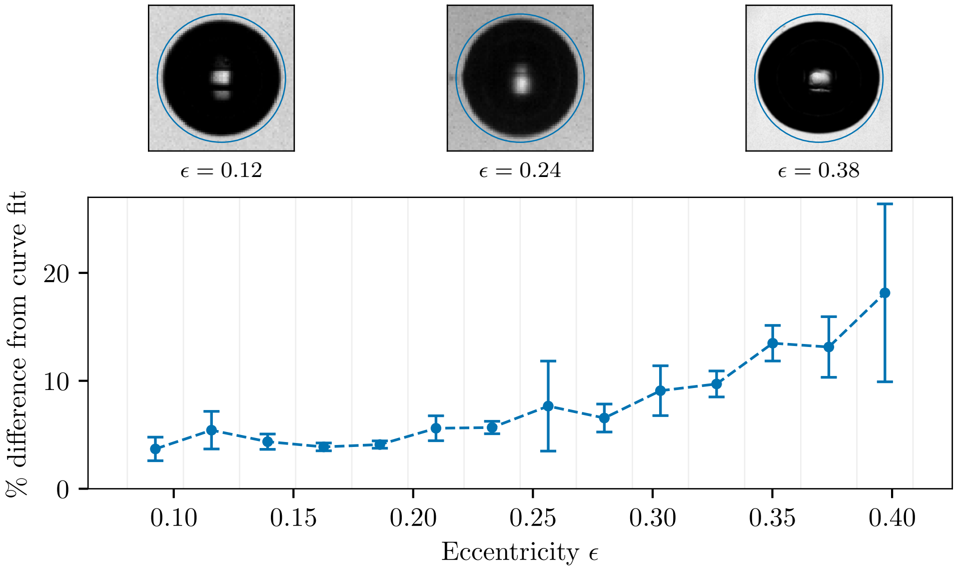

FIGURE 4.6: A plot showing how the spread of data varies with eccentricity. The spread is defined as the percentage difference between a data point and a curve fitted across all data. Data are placed in discrete bins and the mean of each bin is shown at the bin center with the 95% confidence interval shown by the error bars. Only bins with five or more data points are included. Frames showing examples of select eccentricities are displayed above the plot with perfect circles surrounding the bubbles for comparison.

4.4.2.2 Experimental data for all geometries

For any geometry, the displacement and radius ratio measurements can be plotted against predicted anisotropy magnitudes. All considered geometries are shown in figure 4.7. The corner, square prism and triangular prism data are plotted with semi-analytic anisotropy model predictions. The corner used $M = 3$ or $M = 5$, depending on corner angle, and $N \approx 50\,000$ elements in the pressure mesh. The triangular prism model used $M = 11\,163$ image sinks with $N \approx 30\,000$ elements in the pressure mesh. The square prism model used $M = 4225$ image sinks with $N \approx 50\,000$ elements in the pressure mesh. The flat plate and slot data are plotted using boundary element method anisotropy model predictions with $N = 19\,896$ and $19\,662 \leq N \leq 20\,142$, respectively. There is some variation in the number of elements used for the slot geometries due to varying slot sizes.

For the bubble displacement, shown in figure 4.7(*a*), all data collapses well onto a single line within the experimental variance of the data. The most significant deviation from this curve is at very low anisotropy magnitude values, where the bubbles move very little. Because of the small displacement, random noise is expected to contribute more to the deviation, although the data appears biased towards smaller displacement values. However, data in this region is sparse, so care should be taken to draw any conclusions from it. We further observe deviations at very high anisotropy magnitude values, where bubbles are very close to the walls and thus can become constrained. This constraint limits any meaningful measurement of the displacement and therefore also precludes any validation of the numerical model in this regime. The collapsed curve conforms to the power law $\Delta / R_0 = 4.54\zeta^{0.51}$.

Figure 4.7(*b*) shows the radius ratio R_1/R_0 as a function of the predicted anisotropy magnitude ζ. It is clear that there is much more spread in the data compared to the displacement data of figure 4.7(*a*). However, looking first at the flat plate and slot data, both data sets approximately collapse onto a single curve.

The data for the two corners has a slightly higher spread than the slots data, and tends to have a lower radius ratio at high anisotropies. Finally, the triangle and square data have the highest spread. The biggest grouping of square data falls close to the collapsed slot and flat plate data, however the triangle data is most significantly grouped below the other data sets. Due to experimental limitations, the triangle and square data is comprised of relatively small bubbles at a greater distance from the camera, producing small images in the frame with short collapse times. Smaller images cannot be measured as accurately as larger images which leads to greater measurement error in determining the radius ratio. In addition, shorter collapse times lead to fewer frames of data which can cause the radius to be measured at the wrong time. However, neither of these factors can fully account for such spread of data. It is noted that more confined geometries tend to have higher spreads of radius ratio which suggests that shockwave reflections might play a more important role in such geometries. Despite these variations, much of the data collapses reasonably well (in particular the slots and flat plate data), suggesting that it does strongly depend on the anisotropy parameter as has been previously reported (Supponen *et al.*, 2018).

Supponen *et al.* (2018) presented the ratio of energy between first and second size maxima as a function of the anisotropy parameter. The energy was calculated from the radius and thus the radius ratio function can be determined from the given rebound energy ratio function. This function is plotted alongside the data in figure 4.7(*b*) and significantly deviates from the experimental data. Although the cause of this deviation is not known, we speculate that minor variations in the experimental methodology could lead to different amounts of energy dissipation during the collapse, thus producing different radius ratio curves. The sensitivity to experimental conditions could also explain the large spread in the data in figure 4.7(*b*). One such parameter is the amount of non-condensable gas present in the bubble which is difficult to measure experimentally and has previously been shown to strongly affect the size of bubble rebounds (Tinguely *et al.*, 2012; Trummler *et al.*, 2021). Variation in the amount of non-condensable gas is therefore a good candidate as the cause of the variation between previous work and the data presented here. This variation of rebound radius presents a challenge in the use of the collapsed curves presented in the current work. Displacement measured from bubble inception to the end of the first collapse (Supponen *et al.*, 2016) is unaffected by rebound size and so the relation between displacement and the anisotropy parameter would be expected to remain constant across all experiments. However, displacement measured from the initial bubble size peak to the rebound size peak would vary as the rebound size varies. Thus, it is expected that the collapsed curves presented in figure 4.7 are not universal.

Despite the lack of universality, this data corroborates the assertion of Supponen *et al.* (2016) that many bubble collapse properties depend primarily on the anisotropy parameter. The collapse of the data also serves to validate the numerical models presented in this work. These models, in combination with established scaling functions (Supponen *et al.*, 2016), can therefore be used to predict bubble collapse properties, such as jet velocity and jet volume, for any rigid geometry.

4.5 Conclusion and outlook

In this work we have presented a numerical model for computing the anisotropy parameter defined by Supponen *et al.* (2016). We have applied this model to a series of complex geometries and demonstrated how the anisotropy parameter varies with bubble position. The anisotropy magnitude is found to be highest when the bubble is highly confined in one or more directions but with open fluid in another direction.

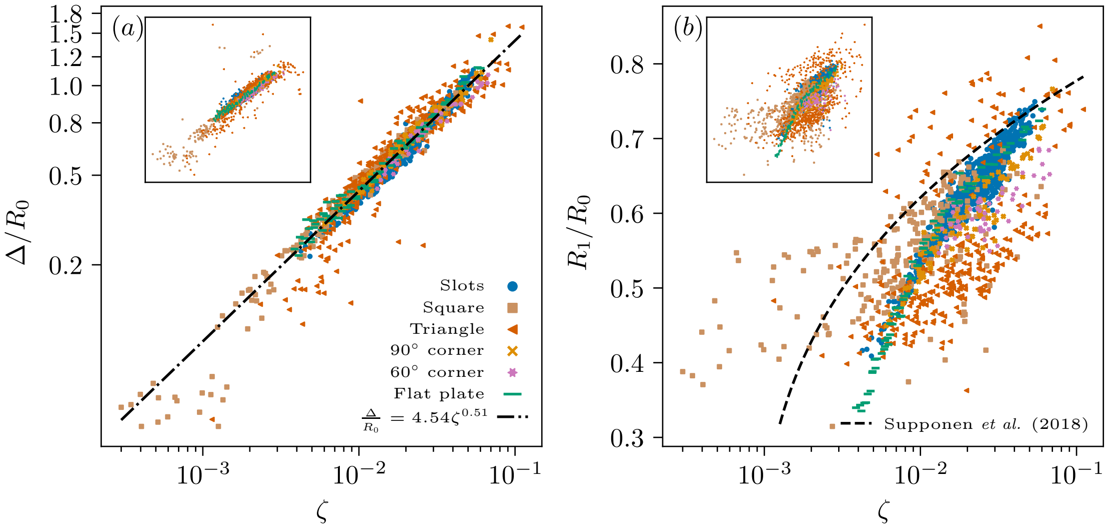

FIGURE 4.7: Experimental data for a flat plate, a series of slots, a triangular prism, a square prism, and two corners. Experimental data is plotted against anisotropy magnitude predictions using the numerical models in this work. (*a*) Normalised bubble displacement Δ/R_0 against anisotropy magnitude ζ. A power law curve fit for all the data combined is shown by the black dash-dotted line. (*b*) Ratio of second bubble size maximum to first bubble size maximum R_1/R_0 against anisotropy magnitude ζ. The black dashed line is derived from Supponen *et al.* (2018). Inset axes of both plots include all data unfiltered.

This configuration is mostly found near concave corners of geometries. The anisotropy magnitude is found to be at a minimum far from geometries and in highly symmetric areas.

We have experimentally measured two parameters of bubble collapse that can both be measured robustly: the bubble displacement and ratio of bubble radius between the first two size maxima. Using the anisotropy magnitude predicted by the numerical model, we have shown that the bubble displacement collapses onto a single curve which conforms to the power law $\Delta/R_0 = 4.54\zeta^{0.51}$ where Δ/R_0 is the dimensionless displacement and ζ is the anisotropy parameter magnitude. A large portion of the radius ratio data collapses approximately onto a single curve, however there is very high spread in some data sets and some significant overall deviation from the collapsed curve. In addition, it is clear that this data does not collapse onto the same curve as was presented by Supponen *et al.* (2018). We suggest that this variation could be significantly influenced by experimental differences such as the non-condensable gas content of the bubble. Such a variation should also lead to a variation in shockwave energy so the energy partition could be used to test this theory (Tinguely *et al.*, 2012). We recommend further investigation of this discrepancy, aiming to identify the key parameters that lead to such variation between experimental setups and how those parameters can be controlled.

Previous research has shown that the anisotropy parameter is a good predictor of various collapse properties in a range of simple geometries (Supponen *et al.*, 2016). The anisotropy parameter model presented here, in combination with experimental data, has shown that the anisotropy parameter remains a good predictor of collapse properties, even in complex geometries. Thus, this model can be combined with scaling laws, such as those presented by Supponen *et al.* (2016), to predict many bubble collapse properties, such as jet velocity, jet volume, and jet impact time. The anisotropy vector direction produced by this model is equivalent to the directions produced by models that have already been investigated in connection with the bubble displacement direction (Tagawa & Peters, 2018; Molefe & Peters, 2019; Andrews *et al.*, 2020). This model can therefore provide a complete prediction of the bubble displacement for any rigid geometry.

Chapter 5

Bubble collapse near porous plates

This chapter is based on a paper that has been submitted to Journal of Fluid Mechanics (Andrews et al., 2022).

5.1 Abstract

A gas or vapour bubble near a solid boundary collapses towards the boundary due to the asymmetry induced by the nearby boundary. High surface pressure and shear stress from this collapse can damage, or clean, the surface. A porous boundary, such as a filter, would act similarly to a solid boundary but with reduced asymmetry and thus reduced effect. Prior research has measured the cleaning effect of bubbles on filters using ultrasonic cleaning, but it is not known how the bubble dynamics are fundamentally affected by the porosity of the surface. We address this question experimentally by investigating how the standoff distance, porosity, pore size, and pore shape affect two collapse properties: bubble displacement and bubble rebound size. We show that these properties depend primarily on the standoff distance and porosity of the boundary and extend a previously developed numerical model that approximates this behaviour. Using the numerical model in combination with experimental data, we show that bubble displacement and bubble rebound size each collapse onto respective single curves.

5.2 Introduction

Collapsing bubbles can be found in numerous physical systems. Typically this involves bubbles collapsing in proximity to various boundaries. The high surface pressures and shear stresses generated by collapsing bubbles can damage, or clean, the boundary. This cleaning effect can be harnessed through processes such as ultrasonic cleaning (Reuter & Mettin, 2016) which can involve complex geometries (Verhaagen *et al.*, 2016).

Single bubbles collapsing near simple geometries, such as flat rigid boundaries, have been widely investigated. Much of this research has focused on understanding bubble morphology and jetting (Kröninger *et al.*, 2010; Zhang *et al.*, 2019), nearby surface shear stress (Koukouvinis *et al.*, 2018), surface pressure (Benjamin & Ellis, 1966; Li *et al.*, 2016), and surface damage (Sagar & el Moctar, 2020).

There has been a recent effort to characterise single bubble collapse in a range of complex geometries. For example, characterising jet direction in a selection of geometries including in concave corners (Tagawa & Peters, 2018), inside rectangular and triangular prisms (Molefe & Peters, 2019), above slots (chapter 3), and in the corner of a wall and a free surface (Kiyama *et al.*, 2021). Bubble morphology, flow properties, and jetting behaviours have also been investigated in combinations of concave corners and free surfaces (Zhang *et al.*, 2017; Brujan *et al.*, 2018), between two parallel rigid boundaries (Brujan *et al.*, 2019; Rodriguez *et al.*, 2022), inside a slot (Brujan *et al.*, 2022), on a convex corner (Zhang *et al.*, 2020), on a crevice (Trummler *et al.*, 2020), and on ridge-patterned structures (Kim & Kim, 2020; Kadivar *et al.*, 2022). Nevertheless, there remain fundamental complex geometries that have yet to be explored.

Porous materials are a large family of complex geometries with a wide range of applications. Broadly, they could be categorised as connected or unconnected. One example of an unconnected porous material is a bed of sand, such as those investigated by Sieber *et al.* (2022). The sand creates pores which are permeated by water, but the grains are able to separate which allows for significant deformation of the bed. The influence of the bubble on the boundary is shown to depend on the granular size of the sand, including behaviors such as granular jets and displacement of the boundary material. However, the boundary is modelled as a liquid-liquid interface and it is shown that the bubble rebound and displacement are principally driven by the density difference between the pliable granular suspension and the water.

Connected porous materials have a wide range of applications, of which one very practical application is filters. Filters are typically porous materials through which a fluid is passed in order to remove contamination. This contamination builds up on the filter, reducing performance. Ultrasonic cleaning can be applied to filters in order to remove the built-up contamination from the filter (Reuter *et al.*, 2017).

The simplest example of a porous material is a flat plate with a pattern of through-holes. Some research has investigated the problem of a plate with a through-hole bounding a free surface in relation to breaches of maritime hulls (He *et al.*, 2021; Cui *et al.*, 2021, 2022). Similarly, Sun *et al.* (2022*b*) investigated bubble collapse near a rigid surface with a gas-entrapping hole. This concept was also investigated by Gonzalez-Avila *et al.* (2020*b*) and Sun *et al.* (2022*a*), who considered surfaces with a pattern of gas-entrapping holes. In all these cases, bubbles were found to translate away from the boundary, acting analogously to a typical free surface.

Liu *et al.* (2017) investigated a bubble collapsing between a free surface and a submerged solid boundary with a through-hole. Bubbles collapsing close to a fully submerged rigid boundary with a single through-hole have also been investigated, both experimentally (Lew *et al.*, 2007; Karri *et al.*, 2011; Abboud & Oweis, 2013) and numerically (Khoo *et al.*, 2005). Similarly, Moloudi *et al.* (2019) numerically investigated bubble collapse dynamics close to a convex boundary with a through-hole. These investigations revealed similar tendencies of the bubbles during collapse, such as the bubble translating towards and through the holes, the bubble surface expanding into the holes, and stronger counter-jetting than solid plates.

In this research, we investigate a less-studied phenomenon: how a series of porous plates affect bubble collapse dynamics. We include some comments on bubble morphology and measurements of bubble displacement and bubble rebound radius.

5.3 Problem definition

We define a porous plate as a thin, rigid plate with a pattern of through-holes. The plate thickness is defined as H, with through-holes of characteristic length W and spacing S. Three shapes of hole are investigated: circles, squares, and triangles. Circles are the smoothest possible hole shape and triangles are the least-smooth regular polygon, with the tightest corner angle. Squares are somewhere between the two and are used to achieve high void fractions due to their efficient tessellation packing. Schematics of these arrangements are shown in figure 5.1(*a*-*c*). The void fraction ϕ is defined as the fraction of the total plate area that is occupied by holes. For circular holes the void fraction is

$$\phi = \frac{\pi\sqrt{3}}{6}\left(\frac{W}{S}\right)^2, \tag{5.1}$$

for square holes the void fraction is

$$\phi = \left(\frac{W}{S}\right)^2, \tag{5.2}$$

and for triangular holes the void fraction is

$$\phi = \frac{1}{3}\left(\frac{W}{S}\right)^2. \tag{5.3}$$

Bubbles are positioned vertically at a distance Y from the boundary with time-variant radius R and maximum radius R_0. These parameters are shown in figure 5.1(*d*). Horizontally, the bubble can be positioned in two dimensions with varying proximity to the holes. We identify the two extreme cases as a bubble directly over a hole and a bubble directly over the plate between holes. These two cases represent the minimum and maximum area of solid boundary near the bubble. The horizontal positions of bubbles above holes are shown by the orange circles in figure 5.1. The horizontal positions of bubbles above the plate between holes are shown by the green crosses in figure 5.1 and are usually referred to hereafter as 'between-holes'.

The vertical distance of the bubble is normalised by the maximum bubble radius to produce the dimensionless standoff distance $\gamma = Y/R_0$. The hole size is also normalised with the maximum bubble radius, W/R_0.

In this research we investigate fixed, rigid plates with a constant thickness $H = 1$ mm and compare only the effects of bubble position and hole geometry.

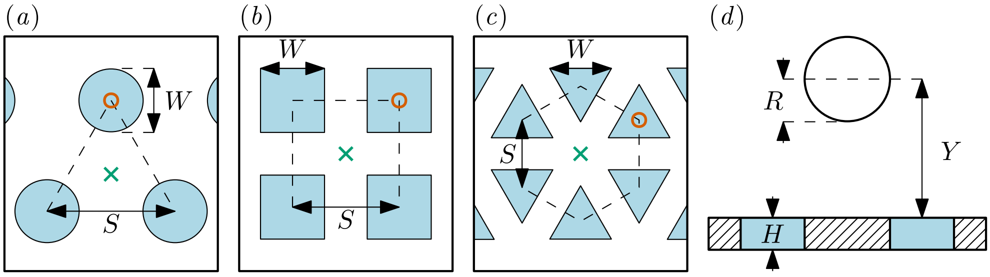

FIGURE 5.1: Top-down view schematic diagrams of porous plates with patterns of circular (*a*), square (*b*), or triangular (*c*) holes. Orange circles mark horizontal positions above a hole and green crosses mark horizontal positions between-holes. (*d*) Side-on cross-section view of a porous plate with a bubble positioned vertically above it.

5.4 Methods

5.4.1 Experimental method

Experiments were performed using laser-induced cavitation with an off-axis parabolic mirror as the focusing optic as described in section 2.1.2.

Porous plates were created by laser cutting 50 mm × 50 mm plates out of stainless steel with a thickness of 1 mm. Stainless steel was selected to ensure rigidity in the plates because other materials, such as 1 mm acrylic, flex significantly under the load of a bubble collapsing, which is known to reduce or reverse displacement (Gibson & Blake, 1982; Brujan *et al.*, 2001*b*). Holes had characteristic lengths between 0.40 mm and 4.79 mm, primarily limited at the low end by laser cut quality. Due to the position of the bubble in close proximity to the plate, the diverging laser impinges upon the plate. If the plate is sufficiently close to the focal point, or the focal angle is narrow, the plate can absorb a significant amount of laser energy which can then nucleate a second bubble at the surface of the material. This nucleation is shown in figure 5.2. In order to stop significant surface nucleation, the plates were polished to reduce laser energy

Hole shape	ϕ (%)	W (mm)	A (mm^2)	$\bar{R}_0$ (mm)
solid	-	-	-	1.50
circles	7.3	1.15	1.04	1.48
circles	11.5	0.40	0.12	1.49
triangles	13.4	1.10	0.52	1.33
circles	14.6	1.15	1.04	1.45
circles	21.6	1.14	1.02	1.50
circles	22.7	4.79	18.02	1.43
squares	22.9	1.96	3.84	1.34
triangles	23.1	2.35	2.40	1.31
circles	23.3	2.37	4.41	1.41
triangles	25.9	1.08	0.50	1.33
circles	29.3	1.15	1.04	1.57
circles	35.6	1.13	1.01	1.45
circles	40.7	1.11	0.96	1.51
triangles	44.1	1.60	1.11	1.33
squares	44.7	1.94	3.77	1.42
squares	52.7	1.94	3.78	1.32
squares	59.4	1.94	3.75	1.39

TABLE 5.1: All experimental geometries used in this research. Ordered by void fraction ϕ and showing hole shape; hole characteristic width W; hole area A; and mean bubble size $\bar{R}_0$.

absorption by increasing the reflectivity. All geometries used are listed in table 5.1 with measurements of the geometric parameters and range of bubble sizes.

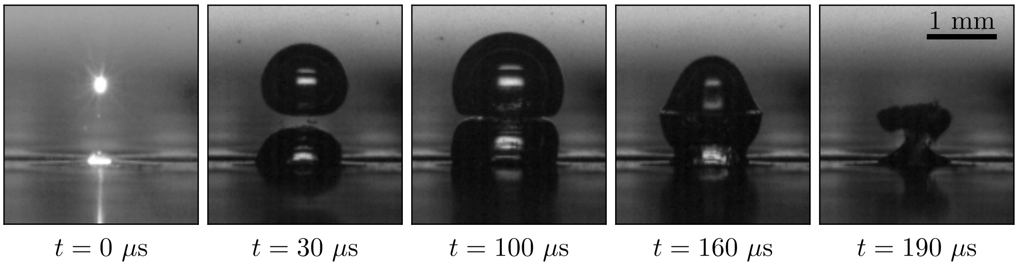

FIGURE 5.2: Frames showing the expansion and collapse of two bubbles, one nucleated at the laser focal point and one simultaneously nucleated where the laser impinges on a nearby steel plate. An approximate scale bar is given.

5.4.2 Numerical model

Bubbles collapsing in complex geometries experience varied degrees of asymmetry. This asymmetry can be quantified with the 'anisotropy parameter' ζ, a dimensionless equivalent of the Kelvin impulse, which can predict several bubble collapse properties (Supponen *et al.*, 2016, 2017, 2018).

In chapter 4, we presented a numerical model, based on the boundary element method, capable of predicting the anisotropy parameter for arbitrary rigid geometries. This model assumes that the bubble can be treated as a fixed three-dimensional point sink in potential flow with a strength depending on the bubble radius and radial velocity of the bubble surface which are calculated by numerically solving the Rayleigh-Plesset equation. Nearby boundaries are modelled by a distribution of point sink elements and the no-through-flow boundary condition is imposed at their centroids. Each element i has a constant sink strength density σ_i across its surface and area A_i such that the sink strength of the centroid point sink is $\sigma_i A_i$ and the velocity induced at a point j by the element i is

$$\nabla \phi|_j = \frac{\sigma_i A_i (\mathbf{x}_j - \mathbf{x}_i)}{4\pi |\mathbf{x}_j - \mathbf{x}_i|^3}, \tag{5.4}$$

where ϕ is the velocity potential, $\mathbf{x}_j$ is a point in the fluid, and $\mathbf{x}_i$ is the centroid position of the element i.

The bubble is assumed to be stationary and the integral of pressures on the boundary surface is calculated and integrated over time. This allows the Kelvin impulse to be estimated and then non-dimensionalised to the anisotropy parameter ζ.

Porous plates could be directly modelled this way, however a high number of elements would be required to adequately resolve the holes. Here we propose an adaptation of the previous model that does not require each hole to be resolved separately.

By assuming that the plate has zero thickness, the plate can be modelled with a single layer of boundary elements. Elements could then be constructed to surround the holes, however this would simply act to redistribute the element centroids and reduce the overall area. Instead, we assume that the plate is homogeneous, and simply scale the element areas using the void fraction so that the porous element area A_i is

$$A_i = (1 - \phi) A_{is} \tag{5.5}$$

where A_{is} is the area of the equivalent solid element. This method assumes that the shape of the holes doesn't matter, and that the holes are small enough that any difference in horizontal position is negligible.

After scaling the areas, the boundary element method solution can proceed as usual, using the reduced A_i for both the boundary conditions and pressure integration. The core boundary element method procedure is described in section 3.4.2.1 and the anisotropy computations are described in section 4.3.

5.5 Experimental results

5.5.1 Bubbles close to porous boundaries

Bubbles collapsing in close proximity to porous boundaries show a broad range of interesting dynamics. In this section, frames from high-speed recordings of five bubble collapses are presented, demonstrating some of these dynamics.

When bubbles collapse close to solid boundaries, they produce strong jets that often impinge on the boundaries. When the bubble is nucleated above a hole (positioned above the orange circles in figure 5.1), these jets can propagate through the hole, producing very long regions of entrained vapour. One such example is shown in figure 5.3. In this figure, an average jet velocity of 39 m s^{-1} is found between $t = 279$ μs and $t = 319$ μs. The frame at $t = 359$ μs shows that the vapour entrained by the jet extends beyond the bottom of the frame. This region of vapour then itself very rapidly collapses, as seen at $t = 369$ μs, followed by the rest of the bubble collapsing down towards the hole.

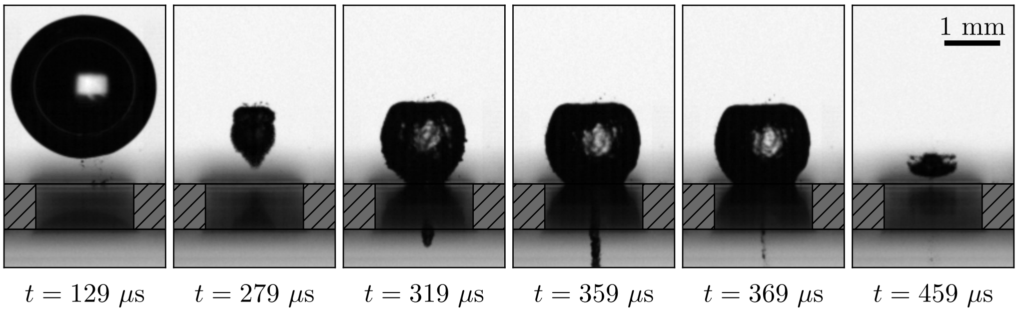

FIGURE 5.3: Frames from a high-speed recording of a bubble collapsing with a strong jet passing through a hole in a porous plate with void fraction $\phi = 44.7$ % and square holes of size $W = 1.94$ mm. A cross-section of the plate at the bubble position is superimposed with hatched areas indicating the solid part of the plate.

As well as allowing jets to pass through the holes, the holes reduce the impedance of the boundary. Bubbles collapse towards solid boundaries because the solid boundary impedes the flow out from the bubble during expansion and into the bubble during collapse. This results in the opposite side of the bubble expanding and collapsing much faster, leading to the overall motion towards the boundary (Blake, 1983). When the bubble is directly over a hole (positioned above the orange circles in figure 5.1), the hole does not impede the bubble expansion and collapse. Figure 5.4 shows one such configuration. Initially, the bubble expands mostly spherically. However, the bottom of the bubble, positioned directly over the hole, expands more than the rest of the lower side, resulting in a protrusion visible in the frame at $t = 80$ μs. The protrusion expands into the hole when the bubble is at its maximum size at $t = 160$ μs. Subsequently, during collapse, the protrusion entirely withdraws by $t = 240$ μs, with a clear gap visible between the now-flattened lower surface and the boundary. Due to the low impedance of the hole compared to the surrounding boundary, the center of the bottom side of the bubble continues collapsing much more rapidly than the surrounding areas. This leads to a full inversion of the bottom of the bubble, visible by the upward-facing triangular jet entering from the bottom side of the bubble at $t = 300$ μs. These qualitative observations agree well with those reported by Khoo *et al.* (2005). The bubble then fully collapses and re-expands by $t = 410$ μs. It is interesting to note in the frame at $t = 410$ μs that the bubble undergoes a rapid ejection event on the upper right surface, the cause of which is unknown. The bubble goes on to travel through the hole, breaking up as it goes.

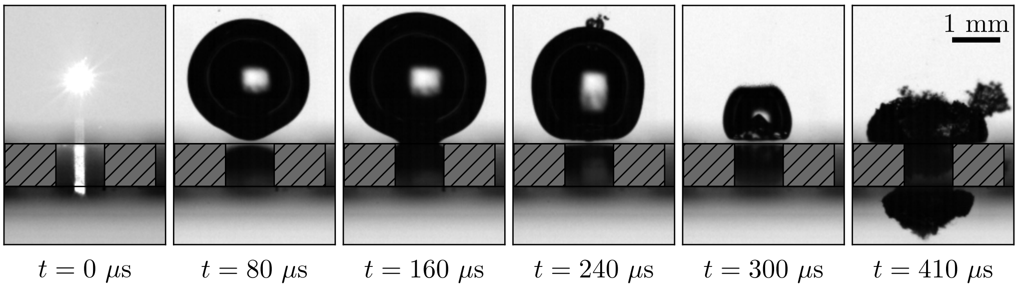

FIGURE 5.4: Frames from a high-speed recording of a bubble collapsing through a hole in a porous plate with void fraction $\phi = 21.6$ % and circular holes of size $W = 1.14$ mm. A cross-section of the plate at the bubble position is superimposed with hatched areas indicating the solid part of the plate.

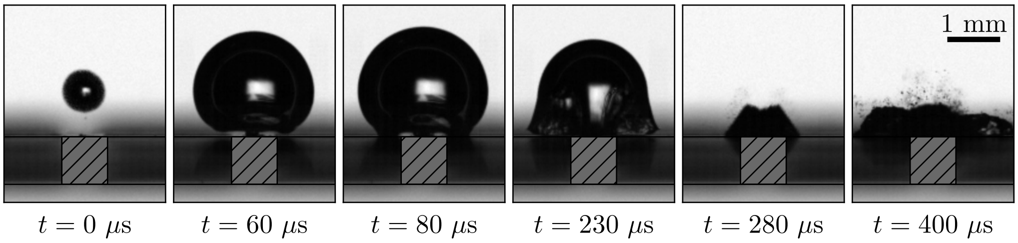

FIGURE 5.5: Frames from a high-speed recording of a bubble collapsing above the area between four holes in a porous plate with void fraction $\phi = 44.7$ % and square holes of size $W = 1.94$ mm. A cross-section of the plate through the row of holes in front of the bubble is superimposed with hatched areas indicating the solid part of the plate.

Bubbles positioned above the solid boundary between holes also expand preferentially towards nearby holes. Figure 5.5 shows a bubble positioned between four square holes (above the green cross in figure 5.1*b*). At the lower edge of the bubble, the areas closest to the holes expand more than the center. These appear as two sharper protrusions on either side of the bottom of the bubble in the frames at $t = 60$ μs and $t = 80$ μs. On the boundary, an extremely small bubble is nucleated by the laser impinging on the boundary. This bubble is visible in the first three frames as a shadow directly below the main bubble. The main bubble, however, does not contact the boundary at the center until the frame at $t = 230$ μs, showing how the solid parts of the boundary strongly limit the growth and collapse of the bubble when compared to the holes. As the bubble begins to collapse, surface instabilities become visible in the frame at $t =$

230 μs, growing initially from the holes and spreading across the bubble surface. The top surface of the bubble rapidly collapses, leaving an indentation on the top of the collapsing bubble at $t = 280$ μs. The bubble then re-expands along the solid parts of the boundary, splitting into multiple sections visible at $t = 400$ μs.

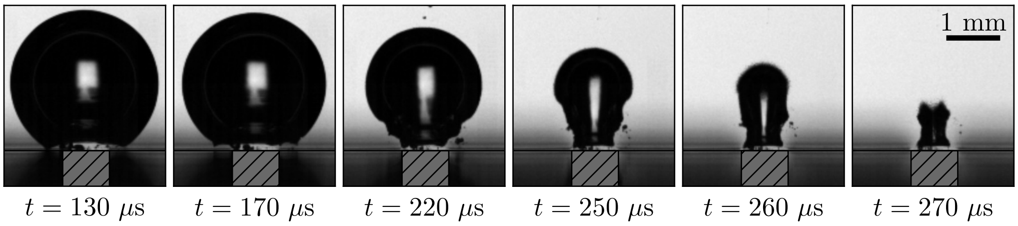

FIGURE 5.6: Frames from a high-speed recording of a bubble collapsing above the area between two holes in a porous plate with void fraction $\phi = 44.7$ % and square holes of size $W = 1.94$ mm. A cross-section of the plate at the bubble position is superimposed with hatched areas indicating the solid part of the plate.

These effects can be further explored by observing a bubble positioned between just two holes. This case is shown in figure 5.6. As in figure 5.5, the bubble in figure 5.6 expands preferentially towards the nearby holes. Again, protrusions are visible on either side of the lower surface of the bubble. However, as the bubble collapses, the motion of these protrusions is in the camera plane and so can be more clearly observed. The surface of the bubble directly adjacent to the solid part of the boundary remains significantly impeded throughout the collapse and so does not move significantly. At $t = 170$ μs the two expanded protrusions have begun to collapse towards bubble centroid. As the collapse advances the protrusions retain their additional curvature, forming ‘ears’ on either side of the bubble which are visible until $t = 270$ μs. The longevity of these ears is a surprising feature as the areas of a bubble with greatest curvature are expected to collapse most rapidly (Lauterborn, 1982).

We note here that the rapid jet, often seen around the time of the first re-expansion of the bubble, is not always aligned with the overall motion of the bubble. This suggests that small asymmetries in the initial plasma formation may affect the bubble dynamics beyond the initial formation and expansion, despite the bubble being very spherical at its maximum size. The mechanism for this behaviour could be some history of the initial plasma and expansion being retained due to insufficient mixing and homogenisation of the internal gases of the bubble. An example of an offset jet is shown in figure 5.7 where the bubble is collapsing near a solid plate. Despite the bubble appearing very spherical at its maximum size, and the plate being highly symmetric, the jet that appears at $t = 400$ μs is clearly offset from the vertical axis (shown by the grey dashed line). Although this jet is strong, it does not affect the overall motion of the bubble as the bubble proceeds to collapse in the expected vertical direction. This effect is visible in data sets we have previously used in chapter 4 and can be found in some other publications such as figure 5 in Požar *et al.* (2021) and figure 4(*a*) in Sieber *et al.* (2022).

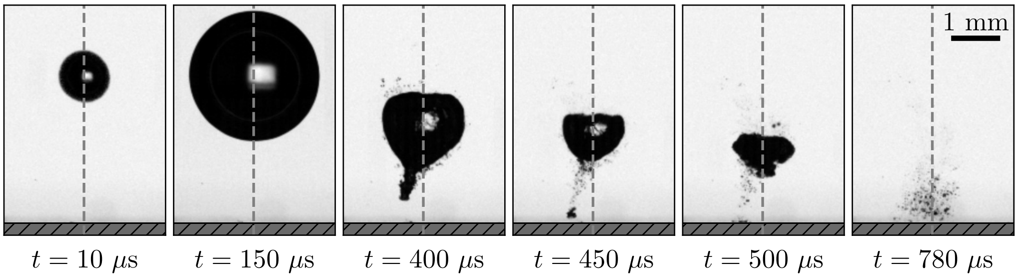

FIGURE 5.7: Frames from a high-speed recording of a bubble collapsing above a solid boundary. The horizontal position of the bubble at its maximum size is shown by the grey vertical line in each frame. The plate is indicated by the hatched grey area at the bottom of the frame.

5.5.2 Variation of displacement and rebound radius with standoff distance

Bubble displacement Δ/R_0 and rebound radius R_1/R_0 are known to depend strongly on the standoff distance $\gamma = Y/R_0$ (Supponen *et al.*, 2016, 2018). In figure 5.8, the blue data points are experimental data from bubbles collapsing near a solid plate. As the standoff distance increases, the displacement decreases, approximately following a power law. Similarly, the rebound radius decreases as the standoff distance increases, although this approximately follows a log law rather than a power law. A porous plate impedes flow, but to a lesser degree than a solid plate. Thus, it induces a lesser displacement and rebound radius than a solid plate as shown by the orange data in figure 5.8. For the porous plate, the displacement approximately follows a power law and the rebound radius approximately follows a log law, which are the same trends as for the solid plate.

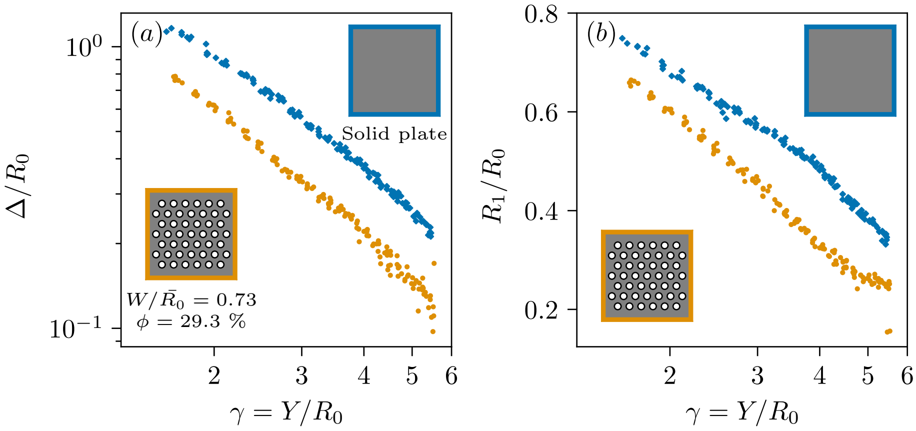

FIGURE 5.8: (*a*) Normalised displacement plotted against standoff distance. (*b*) Normalised rebound radius plotted against standoff distance. Blue diamonds are data from bubbles collapsing near a solid plate. Orange circles are data from bubbles collapsing near a porous plate.

5.5.3 Comparing horizontal position, hole size, and hole shape

Many parameters govern the porous plate and a vast number of plates could be considered with a range of hole shapes and sizes. In addition, the bubble can vary in position relative to the plate both horizontally and vertically. In order to reduce the parameter space, it is thus desirable to determine which parameters can be considered negligible.

As discussed in section 5.3, the horizontal position of the bubble has two extremes: above a hole (above the orange circles in figure 5.1), or directly above an area of plate between holes (above the green crosses in figure 5.1). Intuitively, it can be understood that a bubble above a hole will displace less than a bubble above solid boundary because the fluid does not impede the collapse of the bottom of the bubble. In the limiting case of an infinitely large hole, the bubble experiences no asymmetry, and thus no displacement. Conversely, with a fixed void fraction, infinitely large holes produce infinitely large spaces between holes. Thus, for bubbles nucleated between-holes, the bubble is no longer affected by the holes and so tends towards the solution for a simple solid plate. However, for sufficiently small holes, the difference between bubbles collapsing above a hole and bubbles collapsing between-holes is expected to become negligible.

Here we define a dimensionless area parameter A' to be the ratio between the area of one tessellation unit and the projected area of the bubble. The tessellation unit area is the total area that would be used to calculate the void fraction of one hole. These units are shown graphically in figure 5.9. Thus, the parameter A' is defined as

$$A' = \frac{A}{\phi \pi \bar{R_0}^2} \tag{5.6}$$

where A is the area of one hole and $\bar{R_0}$ is the mean maximum bubble radius of bubble collapse experiments near the plate.

Figure 5.10 shows data for four different plates. One plate has very large tessellation unit area compared to the average bubble size ($A' = 12.54$), while the other three have area ratios in the range $1.78 \leq A' \leq 3.28$. For each plate, bubbles are positioned above a hole and between-holes. The dashed lines follow bubbles above holes and the solid lines follow bubbles between-holes. It is immediately clear that there is a distinct separation of data, with bubbles above holes displacing significantly less, and rebounding to a smaller size, than bubbles between-holes. However, as the standoff distance increases, the dashed and solid lines converge. For the three plates with smaller holes, at sufficiently large standoff distances, the lines merge completely and the data become independent of horizontal position (within experimental variation). For these three data sets, the data become independent of horizontal position at approximately $\gamma = 3$. In general, as A' decreases, convergence occurs at lower standoff distances. Thus, the horizontal position of the bubble is unimportant for displacement and rebound size when the pattern of holes is on a scale smaller than the bubble size. This is confirmed by figure 5.8 where the porous plate data (with $A' = 0.13$) for above a hole and between-holes are plotted together and show no greater spread than the solid plate data in the same figure. In addition, for small holes (low W/R_0) at very low void fractions, the dimensionless area A' can be large but does not result in significant splitting of the data.

The data in figure 5.10 represent three different hole shapes: a square, a circle, and a triangle. The square and smaller circular holes have very similar area ratios and produce almost identical curves for both displacement and rebound size. The triangular holes are slightly smaller and show slightly less splitting of the data. Thus, using the dimensionless area A', the shape of holes can be considered unimportant. This can be explained by the short timescale on which these flows occur. In less rapid flows, the shape of a hole is important due to the viscous boundary layers that form around the edge of the hole. Shapes such as triangles have a greater perimeter per unit area when compared to circles. This increased surface leads to more boundary layers forming which further restrict the flow. However, for flow induced by a bubble collapsing near a hole, there is insufficient time for a significant viscous boundary layer to form and thus the shape of the hole becomes insignificant. This can be shown with the approximate relation $\delta \sim \sqrt{\nu_L t}$ where δ is the approximate scale of the boundary layer thickness, ν_L is the kinematic viscosity, and t is the time over which the boundary layer would develop. The kinematic viscosity of water at room temperature is approximately 1×10^{-6} m^2 s^{-1}. From our experiments, a typical growth and collapse cycle occurs in approximately 0.5 ms. Thus, the boundary layer formed in this time would be on the scale of 0.02 mm which is much smaller than the size of the holes and so can be considered insignificant.

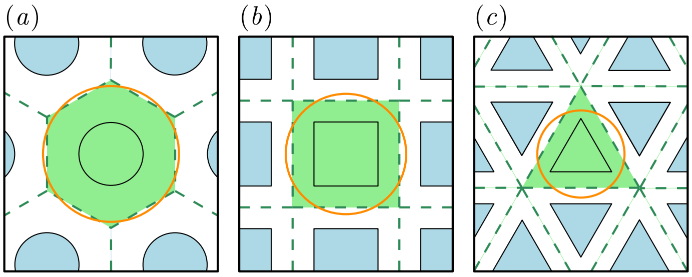

FIGURE 5.9: Top-down view diagrams of porous plates with circular holes (*a*), square holes (*b*), and triangular holes (*c*). The tessellation pattern is shown by the green dashed lines with a single tessellation area shaded in green. The orange circles indicate the size of a bubble with equal area to each tessellation area such that $A' = 1$.

5.5.4 Variation of displacement and rebound ratio with void fraction

From the observations above, we can neglect the influence of hole size, hole shape, and horizontal position for porous plates with dimensionless area $A' < 1.5$ or with small

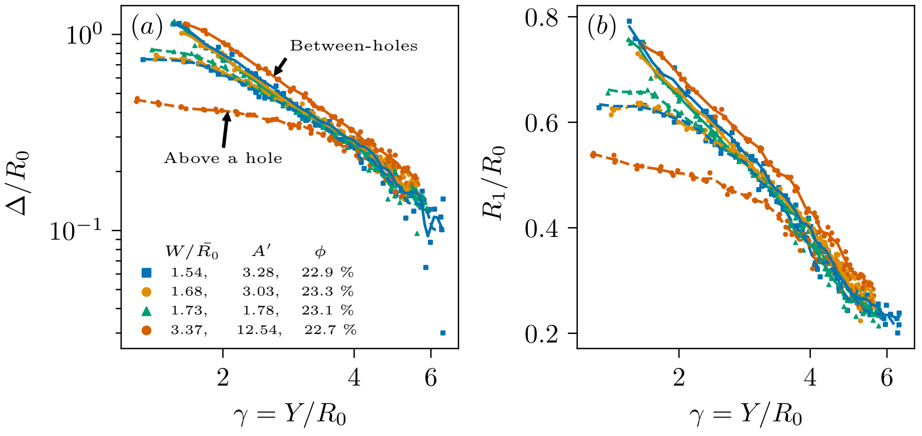

FIGURE 5.10: (*a*) Normalised displacement plotted against standoff distance. (*b*) Normalised rebound radius plotted against standoff distance. Data are plotted for four porous plates with tesselation unit areas $A' > 1.5$. Data for bubbles positioned between-holes are traced by solid lines and data for bubbles positioned above holes are traced by dashed lines. Data markers have shapes corresponding to the shape of holes in the plates (circles, squares, and triangles).

holes ($W/R_0 < 1$). All analysis hereafter relies only on data within this regime and we now further investigate the influence of the void fraction.

Starting from a solid plate, with zero void fraction, and then increasing the void fraction, figure 5.11(*a*) shows that displacement decreases as void fraction increases. Similarly, figure 5.11(*b*) shows that the rebound size ratio decreases as the void fraction increases. Both of these confirm that higher plate porosity results in less asymmetry in the bubble collapse. Despite the decrease in displacement and rebound ratio with increasing void fraction, the gradient remains remarkably similar for all void fractions.

To find out how the displacement and rebound size depend on void fraction, we take vertical slices at three stand-off distances. For each slice, the displacement and rebound size values at a given void fraction are calculated from straight-line fits to each data set shown in figures 5.11(*a*) and 5.11(*b*). Three such curve fits are shown on each of figures 5.11(*a*) and 5.11(*b*) as examples. Figures 5.11(*c*) and 5.11(*d*) show displacement and rebound size ratio as functions of void fraction for three values of standoff distance. The displacement and rebound radius both decrease as the void fraction increases. Both displacement and rebound radius show fairly uniform sensitivity to void fraction across different standoff distances, although the displacement is marginally more sensitive at low standoff distances.

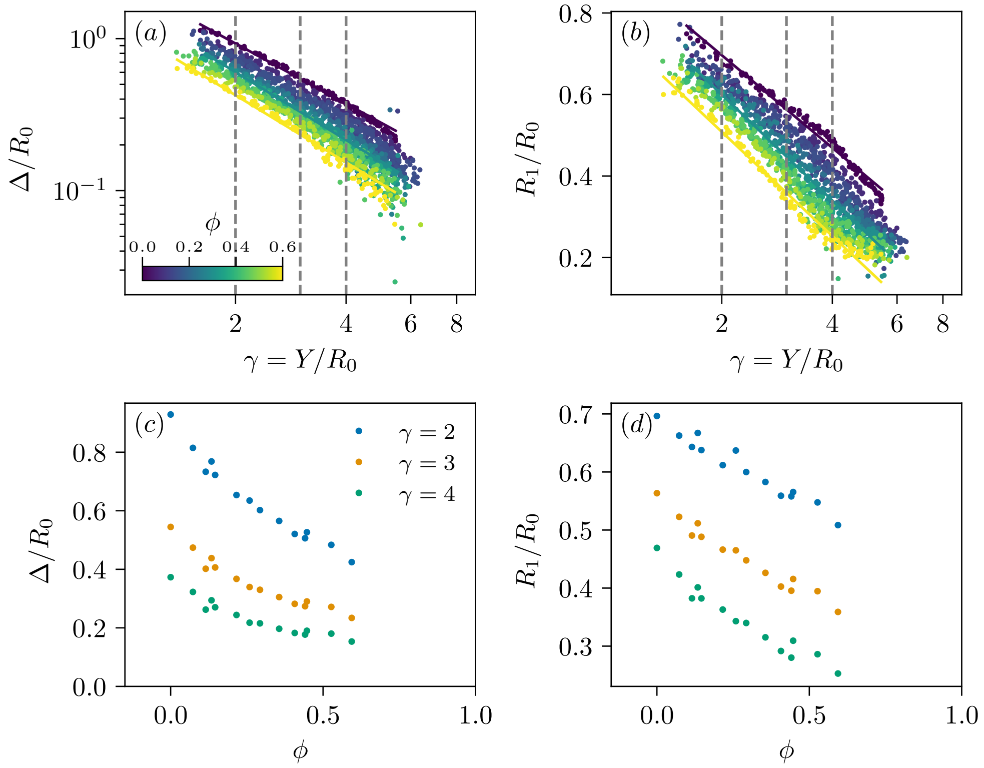

FIGURE 5.11: (*a*) Normalised displacement plotted against standoff distance for a range of void fractions ϕ. (*b*) Bubble rebound radius ratio plotted against standoff distance for a range of void fractions ϕ. Straight-line curve fits are shown for three representative cases in each of (*a*) and (*b*). (*c*) Normalised displacement plotted against void fraction ϕ for standoff distances corresponding to the grey dashed lines in (*a*). (*d*) Bubble rebound radius ratio plotted against void fraction for standoff distances corresponding to the grey dashed lines in (*b*). Only data for plates with $A' < 1.5$ or $W/\bar{R}_0 < 1$ are included in these plots.

5.6 Anisotropy parameter for porous plates

In the previous section, we have shown how displacement and radius ratio vary with both standoff distance and void fraction. In order to unify these parameters, and compare these results with other geometries, it is desirable to formulate the anisotropy parameter as a function of standoff distance and void fraction. We assume that the anisotropy of a porous plate is only a function of void fraction ϕ and standoff distance γ.

$$\zeta = f(\phi, \gamma) \tag{5.7}$$

In this section we present two methods of determining the function $f(\phi, \gamma)$.

5.6.1 Displacement and rebound ratio as a function of anisotropy

The first formulation of the anisotropy parameter is the implementation of the numerical method described in section 5.4.2. Using this method, experimental measurements of displacement and rebound ratio can be plotted as a function of the anisotropy predictions as shown in figure 5.12 (parts *a* and *b*). Although not perfect, it shows reasonable collapse of most data onto a single curve for each of the two measurements.

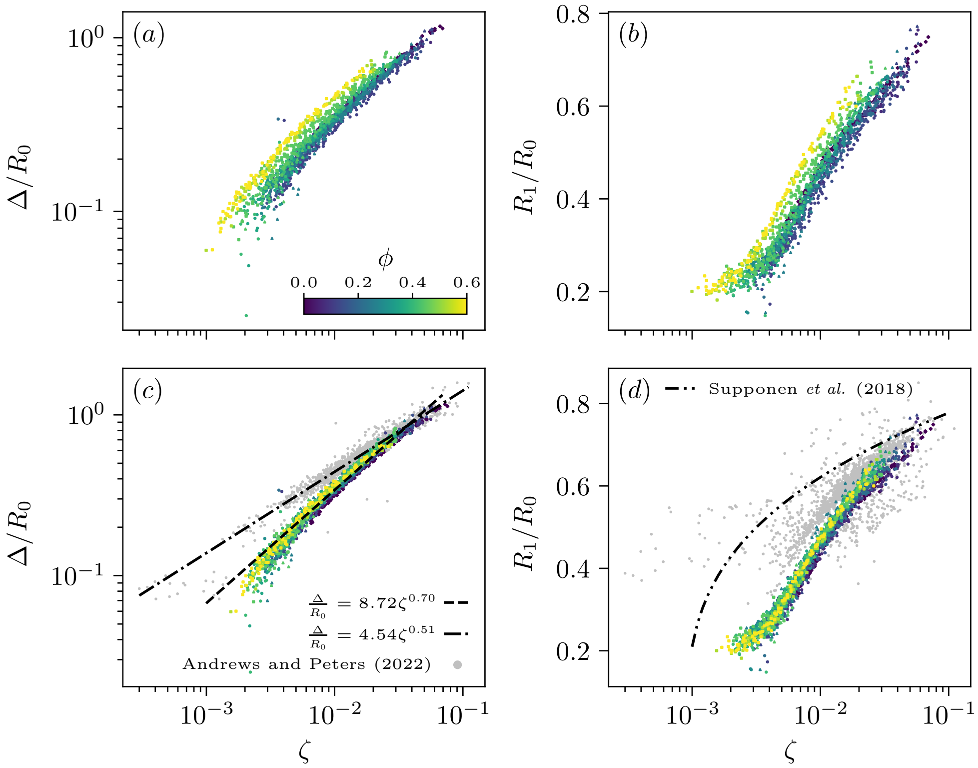

FIGURE 5.12: Normalised displacement (*a*) and rebound radius ratio (*b*) plotted against the anisotropy parameter magnitude ζ predicted by the numerical model. Normalised displacement (*c*) and rebound radius ratio (*d*) plotted against the anisotropy parameter magnitude ζ estimated by fitting displacement data to the solid plate data. Data are coloured by void fraction ϕ. The grey data points in (*c*) and (*d*) are from chapter 4. The black dashed line is a curve fit to the porous plates data. The black dash-dotted line is the curve fit from chapter 4. The black dash-dot-dotted line is derived from the curve fit of Supponen *et al.* (2018).

Using the numerical model, we find that the anisotropy parameter varies almost exactly with γ^{-2} across all porous plates. This is consistent with all the other anisotropy functions for flat geometries presented by Supponen *et al.* (2016). Thus, we simplify equation 5.7 to

$$\zeta = g(\phi)\gamma^{-2}, \tag{5.8}$$

leaving only the function $g(\phi)$ to be determined. Using the numerical model, the prefactor $g(\phi)$ is plotted as the orange line in figure 5.13. This was computed for a 50 mm × 50 mm plate using 19 756 elements, with element lengths ranging between 0.35 mm and 0.42 mm, where larger elements were used around the edge of the plate. As the void fraction increases, the prefactor $g(\phi)$ decreases. At a void fraction $\phi = 0$, identically a solid plate, the prefactor approaches the solution for a solid plate $g(0) = 0.195$. Notably, due to differences between the numerical model and analytic solution for a flat plate, the boundary element method solution does not reach 0.195. At the opposite limit, with void fraction $\phi = 1$, the plate does not exist, resulting in zero anisotropy, thus $g(1) = 0$. Between these limits the gradient of the prefactor is highest at low void fractions, indicating higher sensitivity to void fraction when the void fraction is low. This conclusion is also reflected in the shape of the curves in figure 5.11(*c*, *d*).

The second formulation for the anisotropy parameter assumes that displacement is solely a function of the anisotropy parameter ζ and maintains the assumption that the anisotropy can be written as equation 5.8. The analytic solution for a solid plate ($g(0) = 0.195$) can be applied to the solid plate data to give the measured displacement as a function of anisotropy. Then, for each porous plate data set, the prefactor $g(\phi)$ can be fitted such that the porous plate data follows the same curve for displacement against anisotropy. This curve fit is performed using the logarithmic least-squares difference between each data set and the curve fit on the solid plate data.

Using the fitted prefactors $g(\phi)$, the data collapses very well onto single curves for displacement and rebound radius as shown in figure 5.12 parts (*c*) and (*d*). It should be noted that only the displacement curve is fitted and the resulting values cause the rebound radius data to collapse as well, suggesting that these values are representative of the underlying physics and not simply overfitting to the data.

The fitted prefactors are shown alongside the numerically predicted curve in figure 5.13 with vertical error bars of one standard deviation of the least-squares fit. In this plot, different horizontal positions are treated as distinct data sets, resulting in two data points for each porous plate which are typically very closely aligned.

Figure 5.13 shows that the boundary element method agrees well with the experimentally determined prefactors. However, at low void fractions the experimental values tend to be below the numerical predictions, whereas at higher void fractions they tend to be above. This may suggest that there are some nuances to the behaviour that the numerical model cannot capture.

An empirical curve fit for the anisotropy parameter is desirable in order to further reduce the cost of modelling porous boundaries. It is noted that the two limits of $g(\phi)$ are $g(0) = 0.195$ and $g(1) = 0$. We assume that $g(\phi)$ is a non-linear, smooth function between these limits of the form

$$g(\phi) = 0.195(1 - \phi^k) \tag{5.9}$$

where k is the single parameter to be fitted. Using the experimental data shown in figure 5.13, the fitted parameter k is found to be 0.500 with a standard deviation of 0.027. This curve fit is plotted alongside the data in figure 5.13 which shows good agreement with experimental data. The anisotropy can therefore be written as

$$\zeta = 0.195(1 - \phi^k)\gamma^{-2} \tag{5.10}$$

for all $\phi \in [0, 1]$, effectively providing a single equation for displacement and rebound radius for any void fraction and standoff distance.

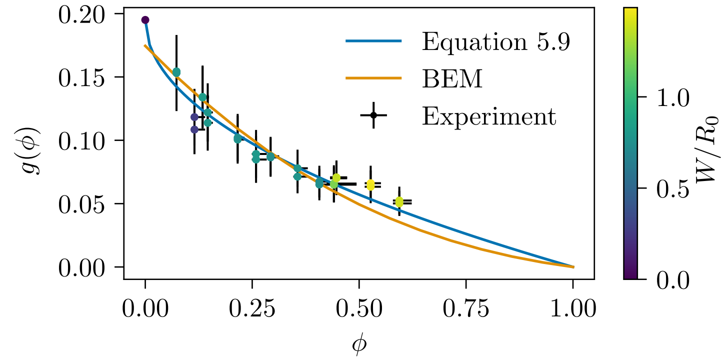

FIGURE 5.13: Prefactors $g(\phi)$ where $\zeta = g(\phi)\gamma^{-2}$ plotted against void fraction ϕ. Experiment data points are computed from fitting displacement data for porous plates with the solid plate data. Horizontal error bars represent the range of possible void fractions for each data point. Vertical error bars are the standard deviation from the least squares fit of $g(\phi)$. Points are coloured by the dimensionless width of the holes.

5.6.2 Disparity with other experimental methodologies

Computing the anisotropy for this data allows it to be compared to prior research, as shown in figure 5.12 (parts *c* and *d*). Figure 5.12(*d*) shows the curve presented by Supponen *et al.* (2017) as well as data points from chapter 4 which used a different experimental method than the present chapter. Although there is significant spread in the data from chapter 4, it does not follow the same curve as the present research. The curve presented by Supponen *et al.* (2017) is even further different. This reinforces our previous suggestion that there is likely another factor that varies between experimental methodologies that can significantly affect the bubble rebound size.

Figure 5.12(*c*) shows data points and the curve fit for displacement against anisotropy for a range of complex geometries presented in chapter 4. This collapsed curve is markedly different to the curve presented in the present research. The principle difference between the two works is that the previous research used a microscope objective to create bubbles whereas the current research uses an off-axis parabolic mirror. This difference in displacement is likely partly due to smaller rebounds, but may also be affected by bubble morphology due to the difference in plasma shapes created by different focusing optical elements.

5.7 Conclusion

In this chapter, we have investigated how a pattern of through-holes in a rigid boundary affect the dynamics of a collapsing bubble. We have demonstrated how bubbles expand preferentially towards the holes and less towards the solid parts of the boundaries. We have shown that the displacement and rebound radius do not depend significantly on the shape of the holes, and the size of the holes only becomes important when comparable to the bubble size (dimensionless tessellation unit area $A' > 1.5$).

The bubble displacement and rebound radius depend strongly on both the standoff distance and void fraction of the porous plate. These parameters can be unified in terms of the anisotropy parameter with equation 5.10. Using this unified parameter, all data for porous plates collapse onto single curves for displacement and rebound radius. However, the collapsed curves vary from those found in chapter 4 which used a different experimental method.

This work provides a solid first step towards characterising bubble behaviour near porous plates and connects this geometry to the wider framework of investigations using the anisotropy parameter.

Chapter 6

Conclusion

In this work we have experimentally and numerically investigated how complex geometries affect the dynamics of bubble collapse.

We first showed that the jet produced by a bubble collapsing near a slot angles away from the slot. The angle reaches a maximum near the edge of the slot and becomes independent of the depth of the slot for sufficiently deep slots. We captured this behaviour using experiments and the boundary element model that we developed. Using the boundary element model, we showed that the jet angle collapses onto a single curve for all slot geometries when appropriate normalisations are applied. Many geometries could be considered analogous to a slot, such as a hole or recess in a flat plate, and similar conclusions would be expected.

We have then extended the boundary element method to not only capture the angle of the bubble collapse, but also the asymmetry of the collapse. This was quantified using the anisotropy parameter and our model agreed well with previous analytic results. We then applied this model, and a simplified, semi-analytic version of this model, to predict anisotropy values for a range of complex geometries. We showed, as expected, that bubbles that are confined in one direction and exposed to open fluid in the opposite direction experience greater anisotropy. We then used our model to predict anisotropy values for experimental measurements of bubble displacement and bubble rebound size. The bubble displacement collapsed very well onto a single curve using the anisotropy values. However, the rebound size data sets showed a lot of scatter, possibly due to shockwave rebounds in confined geometries. Nevertheless, the least-scattered data sets did collapse down onto one curve. We also showed that this mostly-collapsed curve did not agree with previous research, suggesting that there may be other parameters affecting the bubble rebound size such as the amount of non-condensable gas in the bubble.

Finally, we investigated bubble collapse near porous plates. We showed that the bubble displacement and rebound size do not depend strongly on the hole size and shape for holes smaller than the bubbles. Thus, bubble displacement and rebound size depend primarily on the void fraction of the plate and the standoff distance. Using our numerical model and an empirical curve fit, we showed that the curves once again collapse. However, these collapsed curves were different to the previous displacement and rebound size curves, which we expect is due to the different experimental methodology being used. This reinforces our suggestion that there is another parameter significantly affecting the rebound size. This investigation of porous plates lays the groundwork for future investigations of more generalised porous materials.

The numerical model presented in this work allows any complex geometry to be investigated within the anisotropy parameter framework to leverage existing and future results. However, further work is required to connect this framework of single-bubble collapse to applications such as ultrasonic cleaning. For example, understanding the geometric distribution of bubble collapse events induced by an ultrasound field, the combined effect of multiple bubbles, and the relation between surface shear stress and the anisotropy parameter.

References

ABBOUD, JACK E. & OWEIS, GHANEM F. 2013 The microjetting behavior from single laser-induced bubbles generated above a solid boundary with a through hole. *Experiments in Fluids* **54** (1), 1438.

AKHATOV, I., LINDAU, O., TOPOLNIKOV, A., METTIN, R., VAKHITOVA, N. & LAUTERBORN, W. 2001 Collapse and rebound of a laser-induced cavitation bubble. *Physics of Fluids* **13** (10), 2805–2819.

ANDREWS, ELIJAH D., FERNÁNDEZ RIVAS, DAVID & PETERS, IVO R. 2020 Cavity collapse near slot geometries. *Journal of Fluid Mechanics* **901**, A29.

ANDREWS, ELIJAH D., FERNÁNDEZ RIVAS, DAVID & PETERS, IVO R. 2022 Bubble collapse near porous plates, arXiv: 2210.03614.

ANDREWS, ELIJAH D. & PETERS, IVO R. 2022 Modeling bubble collapse anisotropy in complex geometries. *Physical Review Fluids* **7** (12), 123601.

BENJAMIN, T B & ELLIS, A T 1966 The Collapse of Cavitation Bubbles and the Pressures thereby Produced against Solid Boundaries. *Philosophical Transactions of the Royal Society of London. Series A, Mathematical and Physical Sciences* **260** (1110), 221–240.

BIRKIN, PETER R., OFFIN, DOUGLAS G. & LEIGHTON, TIMOTHY G. 2016 An activated fluid stream - New techniques for cold water cleaning. *Ultrasonics Sonochemistry* **29**, 612–618.

BLAKE, J. R. 1983 Kelvin Impulse: Applications to bubble dynamics. In *Eighth Australasian Fluid Mechanics Conference* (ed. R.A. Antonia), vol. 2, pp. 10B.1–10B.4. Newcastle, N.S.W.: University of Newcastle.

BLAKE, J. R. 1988 The Kelvin impulse: application to cavitation bubble dynamics. *The Journal of the Australian Mathematical Society. Series B. Applied Mathematics* **30** (2), 127–146.

BLAKE, J. R. & CERONE, P. 1982 A note on the impulse due to a vapour bubble near a boundary. *The Journal of the Australian Mathematical Society. Series B. Applied Mathematics* **23** (4), 383–393.

BLAKE, J. R. & GIBSON, D. C. 1981 Growth and Collapse of A Vapour Cavity Near A Free Surface. *Journal of Fluid Mechanics* **111**, 123–140.

BLAKE, J R & GIBSON, D C 1987 Cavitation Bubbles Near Boundaries. *Annual Review of Fluid Mechanics* **19** (1), 99–123.

BLAKE, JOHN R., LEPPINEN, DAVID M. & WANG, QIANXI 2015 Cavitation and bubble dynamics: The Kelvin impulse and its applications. *Interface Focus* **5** (5), 1–15.

BLAKE, J. R., TAIB, B. B. & DOHERTY, G. 1986 Transient cavities near boundaries. Part 1. Rigid boundary. *Journal of Fluid Mechanics* **170**, 479–497.

BLAKE, J. R., TAIB, B. B. & DOHERTY, G. 1987 Transient cavities near boundaries Part 2. Free surface. *Journal of Fluid Mechanics* **181** (-1), 197.

BREBBIA, C. A. & DOMINGUEZ, J. (JOSE) 2001 *Boundary elements : an introductory course*. WIT Press.

BRENNEN, CHRISTOPHER E. 1995 *Cavitation and Bubble Dynamics*. Oxford University Press.

BRENNEN, CHRISTOPHER E. 2003 Cavitation in Biological and Bioengineering Contexts. *Fifth International Symposium on Cavitation*.

BREWER, RICHARD G. & RIECKHOFF, KLAUS E. 1964 Stimulated Brillouin scattering in liquids. *Physical Review Letters* **13** (11), 334–336.

BRUJAN, EMIL ALEXANDRU, NAHEN, KESTER, SCHMIDT, PETER & VOGEL, ALFRED 2001*a* Dynamics of laser-induced cavitation bubbles near an elastic boundary. *Journal of Fluid Mechanics* **433**, 251–281.

BRUJAN, EMIL ALEXANDRU, NAHEN, KESTER, SCHMIDT, PETER & VOGEL, ALFRED 2001*b* Dynamics of laser-induced cavitation bubbles near elastic boundaries: Influence of the elastic modulus. *Journal of Fluid Mechanics* **433**, 283–314.

BRUJAN, EMIL ALEXANDRU, NODA, TATSUYA, ISHIGAMI, ATSUSHI, OGASAWARA, TOSHIYUKI & TAKAHIRA, HIROYUKI 2018 Dynamics of laser-induced cavitation bubbles near two perpendicular rigid walls. *Journal of Fluid Mechanics* **841**, 28–49.

BRUJAN, EMIL ALEXANDRU, TAKAHIRA, HIROYUKI & OGASAWARA, TOSHIYUKI 2019 Planar jets in collapsing cavitation bubbles. *Experimental Thermal and Fluid Science* **101**, 48–61.

BRUJAN, EMIL-ALEXANDRU, ZHANG, A.-M., LIU, YUN-LONG, OGASAWARA, TOSHIYUKI & TAKAHIRA, HIROYUKI 2022 Jetting and migration of a laser-induced cavitation bubble in a rectangular channel. *Journal of Fluid Mechanics* **948**, A6.

Canchi, Saranya, Kelly, Karen, Hong, Yu, King, Michael A., Subhash, Ghatu & Sarntinoranont, Malisa 2017 Controlled single bubble cavitation collapse results in jet-induced injury in brain tissue. *Journal of the Mechanical Behavior of Biomedical Materials* **74**, 261–273.

Chahine, Georges L., Kapahi, Anil, Choi, Jin Keun & Hsiao, Chao Tsung 2016 Modeling of surface cleaning by cavitation bubble dynamics and collapse. *Ultrasonics Sonochemistry* **29**, 528–549.

Chin, Chien Ting, Lancée, Charles, Borsboom, Jerome, Mastik, Frits, Frijlink, Martijn E., De Jong, Nico, Versluis, Michel & Lohse, Detlef 2003 Brandaris 128: A digital 25 million frames per second camera with 128 highly sensitive frames. *Review of Scientific Instruments* **74** (12), 5026.

Cui, Jie, yuan Li, Ming, Sun, Shi Yan, Xu, Wei, Zhou, Tao Ran & Zhang, Xiao 2022 Experimental studies of bubble dynamics under a broken horizontal plate. *Ocean Engineering* **245**, 110459.

Cui, Jie, Zhou, Tao Ran, Huang, Xiao & Li, Zi Chao 2021 Experimental study of bubble dynamics in the neighbourhood of a vertical incomplete boundary. *Ultrasonics Sonochemistry* **75**, 105587.

Cui, Pu, Zhang, A. Man, Wang, Shiping & Khoo, Boo Cheong 2018 Ice breaking by a collapsing bubble. *Journal of Fluid Mechanics* **841**, 287–309.

De La Torre, Ralph 1992 Intravascular laser induced cavitation : a study of the mechanics with possible detrimental and beneficial effects. PhD thesis, Massachusetts Institute of Technology.

Dijkink, Rory, Le Gac, Séverine, Nijhuis, Erwin, van den Berg, Albert, Vermes, István, Poot, André & Ohl, Claus Dieter 2008 Controlled cavitation-cell interaction: Trans-membrane transport and viability studies. *Physics in Medicine and Biology* **53** (2), 375–390.

Dijkink, Rory & Ohl, Claus Dieter 2008 Measurement of cavitation induced wall shear stress. *Applied Physics Letters* **93** (25), 254107.

Dular, Matevž, Požar, Tomaž, Zevnik, Jure & Petkovšek, Rok 2019 High speed observation of damage created by a collapse of a single cavitation bubble. *Wear* **418-419**, 13–23.

Fernandez Rivas, David, Betjes, Joris, Verhaagen, Bram, Bouwhuis, Wilco, Bor, Ton C., Lohse, Detlef & Gardeniers, Han J.G.E. 2013 Erosion evolution in mono-crystalline silicon surfaces caused by acoustic cavitation bubbles. *Journal of Applied Physics* **113** (6), 064902.

GIBSON, D. C. & BLAKE, J. R. 1982 The growth and collapse of bubbles near deformable surfaces. *Applied Scientific Research* **38** (1), 215–224.

GONZALEZ-AVILA, SILVESTRE ROBERTO, VAN BLOKLAND, ANNE CHARLOTTE, ZENG, QINGYUN & OHL, CLAUS-DIETER 2020*a* Jetting and shear stress enhancement from cavitation bubbles collapsing in a narrow gap. *Journal of Fluid Mechanics* **884**, A23.

GONZALEZ-AVILA, SILVESTRE ROBERTO, NGUYEN, DANG MINH, ARUNACHALAM, SANKARA, DOMINGUES, EDDY M., MISHRA, HIMANSHU & OHL, CLAUS DIETER 2020*b* Mitigating cavitation erosion using biomimetic gas-entrapping microtextured surfaces (GEMS). *Science Advances* **6** (13), 6192–6219.

HAN, BING, ZHU, RIHONG, GUO, ZHENYAN, LIU, LIU & NI, XIAO WU 2018 Control of the liquid jet formation through the symmetric and asymmetric collapse of a single bubble generated between two parallel solid plates. *European Journal of Mechanics, B/Fluids* **72**, 114–122.

HARRIS, P. J. 1992 A numerical model for determining the motion of a bubble close to a fixed rigid structure in a fluid. *International Journal for Numerical Methods in Engineering* **33** (9), 1813–1822.

HARRIS, P. J. 1996 The numerical determination of the Kelvin impulse of a bubble close to a submerged rigid structure. *Computer Methods in Applied Mechanics and Engineering* **130** (3-4), 195–202.

HE, MING, WANG, SHI PING, REN, SHAO FEI & ZHANG, SHUAI 2021 Numerical study of effects of stand-off distance and gravity on large scale bubbles near a breach. *Applied Ocean Research* **117**, 102946.

KADIVAR, EBRAHIM, EL MOCTAR, OULD & SAGAR, HEMANT J. 2022 Experimental study of the influence of mesoscale surface structuring on single bubble dynamics. *Ocean Engineering* **260**, 111892.

KARRI, BADARINATH, GONZALEZ-AVILA, SILVESTRE ROBERTO, LOKE, YEE CHONG, O'SHEA, SEAN J., KLASEBOER, EVERT, KHOO, BOO CHEONG & OHL, CLAUS DIETER 2012 High-speed jetting and spray formation from bubble collapse. *Physical Review E - Statistical, Nonlinear, and Soft Matter Physics* **85** (1), 015303.

KARRI, BADARINATH, PILLAI, KIRAN S., KLASEBOER, EVERT, OHL, SIEW WAN & KHOO, BOO CHEONG 2011 Collapsing bubble induced pumping in a viscous fluid. *Sensors and Actuators A: Physical* **169** (1), 151–163.

KELLER, JOSEPH B. & MIKSIS, MICHAEL 1980 Bubble oscillations of large amplitude. *Journal of the Acoustical Society of America* **68** (2), 628–633.

KHOO, B.C., KLASEBOER, E. & HUNG, K.C. 2005 A collapsing bubble-induced micropump using the jetting effect. *Sensors and Actuators A: Physical* **118** (1), 152–161.

KIM, DONGHYUN & KIM, DAEGYOUM 2020 Underwater bubble collapse on a ridge-patterned structure. *Physics of Fluids* **32** (5), 053312.

KIYAMA, AKIHITO, SHIMAZAKI, TAKAAKI, GORDILLO, JOSÉ MANUEL & TAGAWA, YOSHIYUKI 2021 The direction of the microjet produced by the collapse of a cavitation bubble located in between a wall and a free surface. *Physical Review Fluids* **6** (8), 083601.

KOUKOUVINIS, P., GAVAISES, M., SUPPONEN, O. & FARHAT, M. 2016 Simulation of bubble expansion and collapse in the vicinity of a free surface. *Physics of Fluids* **28** (5), 052103.

KOUKOUVINIS, PHOEVOS, STROTOS, GEORGE, ZENG, QINGYUN, GONZALEZ-AVILA, SILVESTRE ROBERTO, THEODORAKAKOS, ANDREAS, GAVAISES, MANOLIS & OHL, CLAUS DIETER 2018 Parametric Investigations of the Induced Shear Stress by a Laser-Generated Bubble. *Langmuir* **34** (22), 6428–6442.

KRÖNINGER, DENNIS, KÖHLER, KARSTEN, KURZ, THOMAS & LAUTERBORN, WERNER 2010 Particle tracking velocimetry of the flow field around a collapsing cavitation bubble. *Experiments in Fluids* **48** (3), 395–408.

KUCERA, A. & BLAKE, J. R. 1990 Approximate methods for modelling cavitation bubbles near boundaries. *Bulletin of the Australian Mathematical Society* **41** (1), 1–44.

KUMAR, PARDEEP & SAINI, R.P. 2010 Study of cavitation in hydro turbines - A review. *Renewable and Sustainable Energy Reviews* **14** (1), 374–383.

LAUTERBORN, W. 1972 High-speed photography of laser-induced breakdown in liquids. *Applied Physics Letters* **21** (1), 27–29.

LAUTERBORN, W. 1982 Cavitation bubble dynamics — new tools for an intricate problem. In *Mechanics and Physics of Bubbles in Liquids*, pp. 165–178. Springer, Dordrecht.

LECHNER, CHRISTIANE, LAUTERBORN, WERNER, KOCH, MAX & METTIN, ROBERT 2019 Fast, thin jets from bubbles expanding and collapsing in extreme vicinity to a solid boundary: A numerical study. *Physical Review Fluids* **4** (2), 021601.

LEW, KELLY SIEW FONG, KLASEBOER, EVERT & KHOO, BOO CHEONG 2007 A collapsing bubble-induced micropump: An experimental study. *Sensors and Actuators A: Physical* **133** (1), 161–172.

LI, S., HAN, R., ZHANG, A. M. & WANG, Q. X. 2016 Analysis of pressure field generated by a collapsing bubble. *Ocean Engineering* **117**, 22–38.

Li, Shuai, Khoo, Boo Cheong, Zhang, A. Man & Wang, Shiping 2018 Bubble-sphere interaction beneath a free surface. *Ocean Engineering* **169**, 469–483.

Li, Shuai, bo Li, Yun & man Zhang, A. 2015 Numerical analysis of the bubble jet impact on a rigid wall. *Applied Ocean Research* **50**, 227–236.

Liu, N. N., Wu, W. B., Zhang, A. M. & Liu, Y. L. 2017 Experimental and numerical investigation on bubble dynamics near a free surface and a circular opening of plate. *Physics of Fluids* **29** (10).

Lu, Jiaxing, Yuan, Shouqi, Luo, Yin, Yuan, Jianping, Zhou, Banglun & Sun, Hui 2016 Numerical and experimental investigation on the development of cavitation in a centrifugal pump. *Proceedings of the Institution of Mechanical Engineers, Part E: Journal of Process Mechanical Engineering* **230** (3), 171–182.

Luo, Xian Wu, Ji, Bin & Tsujimoto, Yoshinobu 2016 A review of cavitation in hydraulic machinery. *Journal of Hydrodynamics* **28** (3), 335–358.

Molefe, Lebo & Peters, Ivo R. 2019 Jet direction in bubble collapse within rectangular and triangular channels. *Physical Review E* **100** (6), 063105.

Moloudi, Gohar, Dadvand, Abdolrahman, Dawoodian, Mazyar & Saleki-Haselghoubi, Noureyeh 2019 Oscillation of a transient bubble near an aperture made in a convex rigid plate. *Engineering Analysis with Boundary Elements* **103**, 51–65.

Noack, Joachim & Vogel, Alfred 1999 Laser-induced plasma formation in water at nanosecond to femtosecond time scales: calculation of thresholds, absorption coefficients, and energy density. *IEEE Journal of Quantum Electronics* **35** (8), 1156–1167.

Obreschkow, D., Bruderer, M. & Farhat, M. 2012 Analytical approximations for the collapse of an empty spherical bubble. *Physical Review E - Statistical, Nonlinear, and Soft Matter Physics* **85** (6), 066303.

Obreschkow, Danail, Tinguely, Marc, Dorsaz, Nicolas, Kobel, Philippe, De Bosset, Aurele & Farhat, Mohamed 2013 The quest for the most spherical bubble: Experimental setup and data overview. *Experiments in Fluids* **54** (4), 1–18.

Obreschkow, D., Tinguely, M., Dorsaz, N., Kobel, P., De Bosset, A. & Farhat, M. 2011 Universal scaling law for jets of collapsing bubbles. *Physical Review Letters* **107** (20), 204501.

Ohl, Claus Dieter, Arora, Manish, Dijkink, Rory, Janve, Vaibhav & Lohse, Detlef 2006 Surface cleaning from laser-induced cavitation bubbles. *Applied Physics Letters* **89** (7).

Oyarte Gálvez, Loreto, Fraters, Arjan, Offerhaus, Herman L., Versluis, Michel, Hunter, Ian W. & Fernández Rivas, David 2020 Microfluidics control the ballistic energy of thermocavitation liquid jets for needle-free injections. *Journal of Applied Physics* **127** (10), 104901.

PALANKER, DANIEL, VANKOV, ALEXANDER & MILLER, JASON 2002 Effect of the probe geometry on dynamics of cavitation. *Proceedings of SPIE - The International Society for Optical Engineering* **4617**, 112–117.

PAN, ZHAO, KIYAMA, AKIHITO, TAGAWA, YOSHIYUKI, DAILY, DAVID J., THOMSON, SCOTT L., HURD, RANDY & TRUSCOTT, TADD T. 2017 Cavitation onset caused by acceleration. *Proceedings of the National Academy of Sciences of the United States of America* **114** (32), 8470–8474.

PETERS, IVO & MOLEFE, LEBO 2019 Dataset for Jet direction in bubble collapse within rectangular and triangular channels, University of Southampton, doi: 10.5258/SOTON/D1151.

PETERS, IVO & TAGAWA, YOSHIYUKI 2018 Dataset for Bubble Collapse and Jet Formation in Corner Geometries, University of Southampton, doi: 10.5258/SOTON/D0595.

PLESSET, MILTON 1949 The dynamics of cavitation bubbles. *Journal of Applied Mechanics* **16** (3), 277–282.

PLESSET, MILTON S. & CHAPMAN, RICHARD B. 1971 Collapse of an initially spherical vapour cavity in the neighbourhood of a solid boundary. *Journal of Fluid Mechanics* **47** (2), 283–290.

PODBEVŠEK, DARJAN, LOKAR, ŽIGA, PODOBNIKAR, JURE, PETKOVŠEK, ROK & DULAR, MATEVŽ 2021 Experimental evaluation of methodologies for single transient cavitation bubble generation in liquids. *Experiments in Fluids* **62** (8), 1–28.

POŽAR, TOMAŽ, AGREŽ, VID & PETKOVŠEK, ROK 2021 Laser-induced cavitation bubbles and shock waves in water near a concave surface. *Ultrasonics Sonochemistry* **73**, 105456.

QUAH, EDMUND WENJIE, KARRI, BADARINATH, OHL, SIEW-WAN, KLASEBOER, EVERT & KHOO, BOO CHEONG 2018 Expansion and collapse of an initially off-centered bubble within a narrow gap and the effect of a free surface. *International Journal of Multiphase Flow* **99**, 62–72.

RAYLEIGH, LORD 1917 VIII. On the pressure developed in a liquid during the collapse of a spherical cavity. *The London, Edinburgh, and Dublin Philosophical Magazine and Journal of Science* **34** (200), 94–98.

REUTER, FABIAN, LAUTERBORN, SONJA, METTIN, ROBERT & LAUTERBORN, WERNER 2017 Membrane cleaning with ultrasonically driven bubbles. *Ultrasonics Sonochemistry* **37**, 542–560.

REUTER, FABIAN & METTIN, ROBERT 2016 Mechanisms of single bubble cleaning. *Ultrasonics Sonochemistry* **29**, 550–562.

RODRIGUEZ, MAURO, BEIG, SHAHABODDIN A., BARBIER, CHARLOTTE N. & JOHNSEN, ERIC 2022 Dynamics of an inertially collapsing gas bubble between two parallel, rigid walls. *Journal of Fluid Mechanics* **946**, A43.

SAGAR, HEMANT J. & EL MOCTAR, OULD 2020 Dynamics of a cavitation bubble near a solid surface and the induced damage. *Journal of Fluids and Structures* **92**, 102799.

SHIMU, Q. I.N., YANG, YULIANG, JUNQI, Q. I.N. & CHANGCHUN, D. I. 2019 Research on the Cavitation in the Snapping Shrimp: A Review. *IOP Conference Series: Earth and Environmental Science* **310** (5), 052057.

SIEBER, A.B., PRESO, D.B. & FARHAT, M. 2022 Dynamics of cavitation bubbles near granular boundaries. *Journal of Fluid Mechanics* **947**, A39.

SIJL, JEROEN, DOLLET, BENJAMIN, OVERVELDE, MARLIES, GARBIN, VALERIA, ROZENDAL, TIMO, DE JONG, NICO, LOHSE, DETLEF & VERSLUIS, MICHEL 2010 Subharmonic behavior of phospholipid-coated ultrasound contrast agent microbubbles. *The Journal of the Acoustical Society of America* **128** (5), 3239.

SINIBALDI, G., OCCHICONE, A., ALVES PEREIRA, F., CAPRINI, D., MARINO, L., MICHELOTTI, F. & CASCIOLA, C. M. 2019 Laser induced cavitation: Plasma generation and breakdown shockwave. *Physics of Fluids* **31** (10), 103302.

SONDE, EMMANUEL, CHAISE, THIBAUT, BOISSON, NICOLAS & NELIAS, DANIEL 2018 Modeling of cavitation peening: Jet, bubble growth and collapse, micro-jet and residual stresses. *Journal of Materials Processing Technology* **262**, 479–491.

SREEDHAR, B. K., ALBERT, S. K. & PANDIT, A. B. 2017 Cavitation damage: Theory and measurements - A review. *Wear* **372-373**, 177–196.

STRICKER, LAURA, DOLLET, BENJAMIN, FERNÁNDEZ RIVAS, DAVID & LOHSE, DETLEF 2013 Interacting bubble clouds and their sonochemical production. *The Journal of the Acoustical Society of America* **134** (3), 1854–1862.

SUN, YURONG, DU, YUXIN, YAO, ZHIFENG, ZHONG, QIANG, GENG, SIYUAN & WANG, FUJUN 2022*a* The Effect of Surface Geometry of Solid Wall on the Collapse of a Cavitation Bubble. *Journal of Fluids Engineering* **144** (7).

SUN, YURONG, YAO, ZHIFENG, WEN, HAIGANG, ZHONG, QIANG & WANG, FUJUN 2022*b* Cavitation bubble collapse in a vicinity of a rigid wall with a gas entrapping hole. *Physics of Fluids* **34** (7), 073314.

SUPPONEN, OUTI, OBRESCHKOW, DANAIL & FARHAT, MOHAMED 2018 Rebounds of deformed cavitation bubbles. *Physical Review Fluids* **3** (10), 103604.

SUPPONEN, OUTI, OBRESCHKOW, DANAIL & FARHAT, MOHAMED 2019 High-speed imaging of high pressures produced by cavitation bubbles. In *32nd International Congress on High-Speed Imaging and Photonics* (ed. Michel Versluis & Eleanor Stride), , vol. 11051, p. 4. SPIE.

SUPPONEN, OUTI, OBRESCHKOW, DANAIL, KOBEL, PHILIPPE & FARHAT, MOHAMED 2015 Detailed Jet Dynamics in a Collapsing Bubble. *Journal of Physics: Conference Series* **656**, 12038.

SUPPONEN, OUTI, OBRESCHKOW, DANAIL, KOBEL, PHILIPPE, TINGUELY, MARC, DORSAZ, NICOLAS & FARHAT, MOHAMED 2017 Shock waves from nonspherical cavitation bubbles. *Physical Review Fluids* **2** (9), 093601.

SUPPONEN, OUTI, OBRESCHKOW, DANAIL, TINGUELY, MARC, KOBEL, PHILIPPE, DORSAZ, NICOLAS & FARHAT, MOHAMED 2016 Scaling laws for jets of single cavitation bubbles. *Journal of Fluid Mechanics* **802**, 263–293.

TAGAWA, YOSHIYUKI & PETERS, IVO R 2018 Bubble collapse and jet formation in corner geometries. *Physical Review Fluids* **3** (8), 081601(R).

TAGAWA, YOSHIYUKI, YAMAMOTO, SHOTA, HAYASAKA, KEISUKE & KAMEDA, MASAHARU 2016 On pressure impulse of a laser-induced underwater shock wave. *Journal of Fluid Mechanics* **808**, 5–18.

VAN TERWISGA, TOM, VAN WIJNGAARDEN, ERIK, BOSSCHERS, JOHAN & KUIPER, GERT 2007 Achievements and challenges in cavitation research on ship propellers. *International Shipbuilding Progress* **54**, 165–187.

TINGUELY, M., OBRESCHKOW, D., KOBEL, P., DORSAZ, N., DE BOSSET, A. & FARHAT, M. 2012 Energy partition at the collapse of spherical cavitation bubbles. *Physical Review E - Statistical, Nonlinear, and Soft Matter Physics* **86** (4), 046315.

TOMITA, Y., ROBINSON, P. B., TONG, R. P. & BLAKE, J. R. 2002 Growth and collapse of cavitation bubbles near a curved rigid boundary. *Journal of Fluid Mechanics* **466**, 259–283.

TRUMMLER, THERESA, BRYNGELSON, SPENCER H., SCHMIDMAYER, KEVIN, SCHMIDT, STEFFEN J., COLONIUS, TIM & ADAMS, NIKOLAUS A. 2020 Near-surface dynamics of a gas bubble collapsing above a crevice. *Journal of Fluid Mechanics* **899**, 16–16.

TRUMMLER, T., SCHMIDT, S. J. & ADAMS, N. A. 2021 Numerical investigation of non-condensable gas effect on vapor bubble collapse. *Physics of Fluids* **33** (9), 096107.

VERHAAGEN, BRAM & FERNÁNDEZ RIVAS, DAVID 2016 Measuring cavitation and its cleaning effect. *Ultrasonics Sonochemistry* **29**, 619–628.

VERHAAGEN, BRAM, ZANDERINK, THIJS & FERNANDEZ RIVAS, DAVID 2016 Ultrasonic cleaning of 3D printed objects and Cleaning Challenge Devices. *Applied Acoustics* **103**, 172–181.

VERSLUIS, M., SCHMITZ, B., VON DER HEYDT, A. & LOHSE, D. 2000 How snapping shrimp snap: Through cavitating bubbles. *Science* **289** (5487), 2114–2117.

WANG, QIANXI, MAHMUD, MEHDI, CUI, JIE, SMITH, WARREN R & WALMSLEY, A D 2020 Numerical investigation of bubble dynamics at a corner. *Physics of Fluids* **32** (5), 53306.

VAN WIJNGAARDEN, LEEN 2016 Mechanics of collapsing cavitation bubbles. *Ultrasonics Sonochemistry* **29**, 524–527.

ZENG, QINGYUN, AN, HONGJIE & OHL, CLAUS DIETER 2022 Wall shear stress from jetting cavitation bubbles: influence of the stand-off distance and liquid viscosity. *Journal of Fluid Mechanics* **932**, 14.

ZENG, QINGYUN, GONZALEZ-AVILA, SILVESTRE ROBERTO, DIJKINK, RORY, KOUKOUVINIS, PHOEVOS, GAVAISES, MANOLIS & OHL, CLAUS-DIETER 2018 Wall shear stress from jetting cavitation bubbles. *Journal of Fluid Mechanics* **846**, 341–355.

ZHANG, A. M. & LIU, Y. L. 2015 Improved three-dimensional bubble dynamics model based on boundary element method. *Journal of Computational Physics* **294**, 208–223.

ZHANG, M., CHANG, QING, MA, XIAOJIAN, WANG, G. & HUANG, BIAO 2019 Physical investigation of the counterjet dynamics during the bubble rebound. *Ultrasonics Sonochemistry* **58**, 104706.

ZHANG, S., ZHANG, A. M., WANG, S. P. & CUI, J. 2017 Dynamic characteristics of large scale spark bubbles close to different boundaries. *Physics of Fluids* **29** (9), 092107.

ZHANG, YUNING, QIU, XU, ZHANG, XIANGQING & TANG, NINGNING 2020 Collapsing dynamics of a laser-induced cavitation bubble near the edge of a rigid wall. *Ultrasonics Sonochemistry* **67**, 105157.

ZHAO, RUI, LIANG, ZHONG CHENG, XU, RONG QING, LU, JIAN & NI, XIAO WU 2008 Dynamics of laser-induced cavitation bubble near solid boundary. *Japanese Journal of Applied Physics* **47** (7 PART 1), 5482–5485.

ZWAAN, ED, LE GAC, SÉVERINE, TSUJI, KINKO & OHL, CLAUS DIETER 2007 Controlled cavitation in microfluidic systems. *Physical Review Letters* **98** (25), 254501.